Interference experiments with the fluorescence light of Ba^+ ions

Dissertation

zur Erlangung des Doktorgrades an der
naturwissenschaftlichen Fakultät
der Leopold-Franzens-Universität Innsbruck

vorgelegt von

Christoph Raab

durchgeführt am Institut für Experimentalphysik
unter der Leitung von
o. Univ. Prof. Dr. R. Blatt

Innsbruck
Jänner 2001

It's completely dark.

His holiness, the 17th Dalai Lama

Abstract

This thesis reports about measurements of fluorescence light of a single Barium ion using various interference techniques. For that purpose a Barium ion is trapped in a spherical Paul trap and cooled with laser light. The fluorescence light of this ion is emitted on its $P_{1/2} \rightarrow S_{1/2}$ transition at 493 nm and detected with a single photon counting setup.

The objectives of the experiments are to investigate the spectrum of the fluorescence light, especially the effects of the ion's motion in the trap on the spectrum, and to study the interaction between the ion and a part of its fluorescence light which is reflected and focused back onto the ion.

The trapped ion is excited with two lasers on its $S_{1/2} \leftrightarrow P_{1/2}$ and $D_{3/2} \leftrightarrow P_{1/2}$ transitions in order to continually observe fluorescence. By comparing a measured excitation spectrum of the trapped ion with a calculation based on optical Bloch equations, the parameters of the laser excitation, such as detunings, intensities, and linewidths, are characterized. In these spectra, narrow spectral features, so-called dark resonances, are observed which indicate Raman transitions between the $S_{1/2}$ and $D_{3/2}$ states. Furthermore, the collection efficiency of the detection channel that is used can be also determined.

In the first part of the thesis the spectrum of the resonance fluorescence is measured utilizing a heterodyne detector. The coherently scattered part of the fluorescence light is detected with a linewidth of 61 mHz (Fourier limited) relative to the exciting laser. Sidebands due to the micro-motion and the macro-motion of the ion are also detected. The cooling rate of the ion is determined from the width of the macro-motion sidebands.

The second main part of this thesis is the interference experiment of an atom with its mirror image. The fluorescence is collected within a solid angle of 4% and collimated with a lens. This light beam is reflected back onto the ion with a mirror. This mirror is adjusted such that the ion and its mirror image are superimposed. The light intensity in the opposite direction is measured with a photo-multiplier as a function of the distance between ion and mirror. While scanning this distance, interference fringes are recorded. Furthermore, by observing the fluorescence at 650 nm from $P_{1/2} \rightarrow D_{3/2}$ transition, the influence of the back reflected light on the internal state of the atom is demonstrated. This experiment is also carried out with two ions, where both ions interact via their fluorescence light which is transferred by the mirror. The fundamental processes that appear when an atom is placed in a structured dielectric environment or in the close vicinity of another atom, such as inhibited or enhanced spontaneous emission and sub- and super-radiance, are all observed in this experiment.

Zusammenfassung

Diese Arbeit berichtet über die Analyse des Fluoreszenzlichts einzelner Ionen mit Hilfe interferometrischer Messtechniken. Dazu wird ein Barium-Ion in einer Paulfalle gespeichert und mit Laserlicht gekühlt. Das Fluoreszenzlicht, welches das Ion wird auf dem $P_{1/2} \rightarrow S_{1/2}$ Übergang bei 493 nm emittiert, wird mit Hilfe eines Photonenzählaufbaus detektiert.

Ziele dieses Experiments sind die Untersuchung des Spektrums des Fluoreszenzlichts, insbesondere die Auswirkungen der Bewegung des Teilchens in der Falle auf das Spektrum, und das Studium der Wechselwirkung eines Ions mit einem Teil seines Fluoreszenzlichts, welches von einem Spiegel zurückreflektiert wird.

Um kontinuierlich Fluoreszenz zu beobachten wird das Ion mit zwei Lasern auf seinen $S_{1/2} \leftrightarrow P_{1/2}$ und $D_{3/2} \leftrightarrow P_{1/2}$ Übergängen angeregt. Trägt man die Fluoreszenzintensität gegen die Laserverstimmung auf (Anregungsspektrum), beobachtet man in diesen Spektra sogenannte Dunkelresonanzen, welche ein Zeichen für Ramanübergänge zwischen dem $S_{1/2}$ und dem $D_{3/2}$ Niveau sind. Die Anpassung der optischen Blochgleichungen an die gemessenen Spektra erlaubt die Bestimmung der Intensitäten, Verstimmungen und Linienbreiten der verwendeten Laser. Außerdem kann die Sammeleffizienz der Detektionskanäle bestimmt werden.

Das Spektrum der Resonanzfluoreszenz wird mit Hilfe eines Heterodyndetektors gemes–sen. Der kohärent gestreute Anteil des Fluoreszenzlichts wird mit einer Linienbreite von 61 mHz (fourierlimitiert) relativ zum anregenden Laser nachgewiesen. Darüber hinaus werden die Seitenbänder der Mikrobewegung und der Makrobewegung im Spektrum beobachtet. Aus der Breite der Seitenbänder der Makrobewegung wird die Kühlrate des Ions bestimmt.

Die Untersuchung der Interferenz eines Ions mit seinem Spiegelbild wird im zweiten Teil der Arbeit behandelt. Das Fluoreszenzlicht wird mit einem Objektiv in einem Raumwinkel von 4% aufgesammelt und kollimiert. Dieser Lichtstrahl wird mit einem Spiegel auf das Ion zurückreflektiert. Die Lichtintensität in die dem Spiegel entgegengesetzter Richtung wird mit einem Photomultiplier als Funktion des Abstandes zwischen Ion und Spiegel gemessen. Wird dieser Abstand verändert, werden Interferenzstreifen beobachtet. Der Spiegel verändert das Vakuumfeld am Ort des Ions, wodurch die spontane Emissionsrate modifiziert wird. Um diese Wechselwirkung nachzuweisen wird gleichzeitig die Fluoreszenz bei 650 nm auf dem $P_{1/2} \rightarrow D_{3/2}$ Übergang als Funktion des Spiegelabstandes nachgewiesen. Somit kann die Besetzung des $P_{1/2}$ Zustandes in Abhängigkeit der Spigelposition direkt gemessen werden. Dieses Experiment wird auch mit zwei Ionen durchgeführt. Dabei wechselwirken beide Ionen über das Fluoreszenzlicht. In Diesem Experiment können alle Prozesse die auftreten, wenn ein Atom sich in einer strukturierten dielektrischen Umgebung oder in der Nähe eines anderen Atoms befindet, beobachtet werden.

Contents

1 Introduction

A single fluorescing atom is the most fundamental light source that can be imagined, and it is theoretically well understood. With the invention of Paul traps [1] and laser cooling [2, 3], it became possible to realize experimentally a single atom well isolated from perturbations through the environment [4, 5], and to investigate its resonantly scattered light.

Analysis of the properties of fluorescence light leads to new insights into the interaction between atoms and light, and to a better understanding of the underlying quantum mechanics. Some of these unique properties can be observed in the non-classical intensity correlation function [6, 7] and quadrature-squeezing [8]. The intensity correlation function $g^{(2)}(\tau)$, i.e. the probability of detecting a photon at the time $t + \tau$ after one other photon was detected at time t, is never smaller than one for classical light sources [9, 10]. The first measurement of a $g^{(2)}(\tau)$ intensity correlation function of a thermal light source was performed by H. Brown and R.Q. Twiss [11] with light from a mercury lamp. It showed higher probability for finding two photons with a very short time delay than for longer temporal separation, i.e. $g^{(2)}(\tau) > 1$ for small τ (bunching). Calculations of the intensity correlation function of fluorescence light for a single atom, however, showed that it can be smaller than one and for $\tau = 0$ it is $g^{(2)}(0) = 0$ [12–14] (anti-bunching). Indeed, experiments with dilute atomic beams, where on average only one atom is in the detection zone [15–17], showed anti-bunching for short times τ. However, for these experiments it was necessary to average over a large number of atoms, because the time that one atom stayed in the detection zone was not sufficiently long to record the intensity correlation function with high signal to noise ratio.
Measurements with the fluorescence light of a single trapped atom stored in a Paul trap have been performed by Diedrich *et al.* [6] and Schubert *et al.* [7]. These experiments confirmed the absolute minimum of the $g^{(2)}(\tau) = 0$ intensity correlation function at the time $\tau = 0$.

While the $g^{(2)}(\tau)$ intensity correlation function is the second order correlation function of the fluorescence light field, other aspects of the light-matter interaction can be learned by investigating the first order correlation function $g^{(1)}(\tau)$ and its Fourier transform, the spectrum of the fluorescence light. First calculations of the fluorescence spectrum were reported by Weisskopf [18] and revealed that for low driving intensities the spectrum consists of a very narrow feature, much narrower than the natural

linewidth. The complete spectrum of resonance fluorescence for a two-level system was calculated by Mollow [19] for all values of the laser intensity. In the low intensity limit these calculations confirmed the narrow spectrum, known as Rayleigh scattering, while for intensities near saturation the spectrum consists of the Rayleigh scattering and one broader line whose width equals the natural linewidth. For high driving intensities, the Rayleigh scattering vanishes and the spectrum is split into three broad peaks, the Mollow triplet. Similar calculations have been made for multi-level atoms and showed that the spectrum reveals similar properties as in the two-level case. For low light intensities, Rayleigh scattering dominates and in the strong field limit, the spectrum consists of several broad peaks.
Spectrally resolved measurements of fluorescence light were performed with atomic Sodium beams by Schuda *et al.* in 1974 and later by Wu and Hartig *et al.* [20–22]. These measurements showed reasonable agreement with the predicted spectrum. Due to the limited interaction time of the atoms with the laser and due to the Doppler shift, the width of the Mollow triplet was broadened. These measurements also showed that the width of the Rayleigh peak is substantially smaller than the natural linewidth. Measurements with single trapped Barium ions were performed by Schubert *et al.* [23] and Stalgies *et al.* [24] and showed good agreement with the calculated spectra. The observed width of the Rayleigh scattering was limited in these measurements by the resolution of the spectrum analyzer, which was a Fabry-Perot interferometer with a linewidth of several MHz.
High resolution measurements of the scattered light can be performed using a heterodyne setup, where the fluorescence light is superimposed with a local oscillator beam at a slightly different frequency. With this setup, the spectral distribution of light frequencies is converted into the radio frequency regime and can be detected with an rf spectrum analyzer which can have a resolution well below 1 Hz. The fluorescence spectrum of Sodium atoms trapped in optical molasses was investigated in this way by Westbrook *et al.* [25] showing a Rayleigh peak with a linewidth of 70 kHz. Later Höffges *et al.* [26] observed a 6 Hz peak in the fluorescence spectrum of a single trapped Magnesium ion.
This high resolution allows investigation of another aspect of the light-atom interaction inside the trap, that is the cooling of the atom through laser light. The oscillation of the trapped ion manifests itself in sidebands of the fluorescence spectrum. These can be very well resolved in the coherent Rayleigh scattering. The relative strength of the sidebands to the carrier is a measure for the amplitude of the oscillation, i.e. the temperature of the atom can be derived. The cooling rate, i.e. the damping rate through laser cooling, can be determined directly from the width of the sidebands [27, 28]. Jessen *et al.* first investigated the influence of the motion of Rubidium atoms stored in optical molasses onto the spectrum of resonance fluorescence [29].

The light-matter interaction can also be studied by placing an optical resonator or a micro-wave resonator around the atom [30–32]. If the coupling between the light field

in the resonator and atom become comparable to or exceed the atomic and cavity decay strengths, the properties of the atom and resonator are significantly changed. For example, the cavity resonance is split into two peaks which are separated by the coupling constant between the atom and the resonator. Also, an excited atom emits its fluorescence photons mainly into the cavity. These cavity QED experiments now use cold atoms falling through a small resonator with a very high finesse [33]. It has been reported [34] that the optical dipole forces act on the trajectories of the falling atom, and, recently, that atoms can be trapped inside the cavity by these optical dipole forces for a short time [35]. However, it has not been possible yet to store an atom inside a cavity for an extended period and within an volume much smaller than the wavelength of the light (Lamb-Dicke regime).

In this thesis, not a cavity but a slightly different approach is used to examine the interaction of the atom with its fluorescence light. The fluorescence light of a single trapped Barium ion is collected in a large solid angle and then reflected back onto the ion with a mirror. This is very similar to a cavity with a low finesse, but the interaction between the ion and the standing light field generated by the mirror is still appreciable because the focus generated by the collimating lens is very tight, i.e. about 1 μm. The advantage of this setup is that the position of the ion is well known with a spread much smaller than the wavelength of the light, and that the ion can be placed into a node or an anti-node of the standing wave created by the mirror at will. The second objective of this work was to measure the rate of laser cooling by observing the sidebands of motion in the fluorescence spectrum. Therefore, the collimated fluorescence light is superimposed with a local oscillator beam and the spectrum is measured in a heterodyne setup.

This thesis is structured as follows: Chapters 2 and 3 are dedicated to the basic theoretical basis necessary for the experiments. In chapter 2, the electrodynamic Paul trap is introduced and basic laser cooling schemes are described. A theoretical description of the laser-ion interaction is given in chapter 3. Emphasis is given to the Bloch equation formalism, which allows one to calculate the steady-state solution of the atom-field Hamiltonian as well as the dynamics of this interaction. The experimental setup is described in chapter 4. Both diode laser systems used in the experiment are described and the trap apparatus with collimation optics is shown. Chapter 5 gives an overview of the basic techniques required for trapping and detecting single Ba^+ ions. The measurements of excitation spectra and intensity correlation functions are also reported. The main experimental results of this thesis are presented in chapters 6 and 7. In chapter 6, first the setup used to record the spectrum of the resonance fluorescence is described. Then the experimental results using different collimating optics are given. These include the measurement of the Rayleigh peak and its sidebands, and the direct measurement of the cooling rate of the ion. Chapter 7 deals with experiments studying the interaction of the ion with a standing wave of its fluorescence light.

2 Paul traps and laser cooling

Precision spectroscopy of atoms requires cold and slow atoms well isolated from their environment, i.e. a small Doppler-shift, long interaction times with the lasers and unperturbed evolution of the atomic state. These requirements can be met with trapped, laser-cooled atoms. W. Paul realized in 1953 [36] that ions can be mass-selected by a linear, quadrupole RF-field. This idea was modified in 1958 [1] into a three-dimensional quadrupole field which allows the trapping of charged particles.

This chapter describes the basics of the Paul trap and the cooling of trapped atoms with lasers.

2.1 Paul traps

In a Paul trap, an electric quadrupole potential

$$\Phi(\vec{r}) = \Phi_0 \sum_{i=x,y,z} \alpha_i (r_i/\tilde{r}_i)^2 \tag{2.1}$$

is used to store ions. Such a potential can be generated with a ring electrode and two end-cap electrodes, which are shaped as the equipotential surfaces of the electric field as shown in Fig. 2.1a. This configuration has the disadvantage that the optical access to the ions through the electrodes is very limited. Therefore, the Paul traps used for single or few ions have a more open electrode structure, as shown in Fig. 2.1b. The field generated by this configuration has higher order terms which, however, become negligible near the trap center. In order to fulfill the Laplace equation $\Delta\Phi = 0$, the sum of the coefficients α_i in (2.1) has to be zero. Therefore, this potential with $\Phi_0 = const.$ has a saddle-point at $\vec{r} = 0$ and does not trap an ion in three dimensions.

It is possible to use an additional magnetic field to confine the ions in the directions not stable due to the electric field. Such a trap is called a Penning trap.

The other possibility to trap ions in three dimensions is to use a time-varying potential $\Phi_0(t) = V_0 + U_0 \cos \Omega_f t$. The quadrupole potential has no mixed terms in α_i, as e.g. $\alpha_1\alpha_2$, therefore the motion in the three dimensions is decoupled. The equation of motion for the charged particle in one dimension is

$$\ddot{r}_i - \frac{\alpha_i q}{m\tilde{r}^2}(V_0 + U_0 \cos \Omega_f t) r_i = 0 \tag{2.2}$$

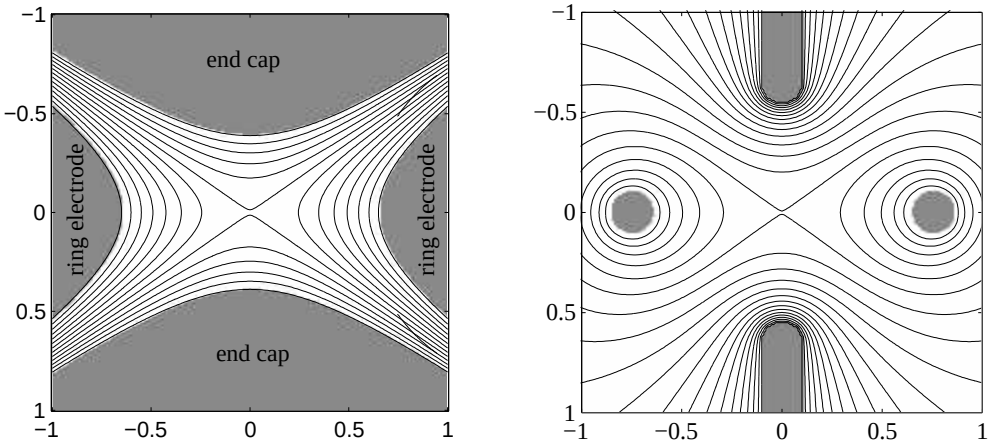

(a) 'original' (b) miniature

Figure 2.1: Electrodes of a Paul trap. The equipotential surfaces are indicated. (a) This potential is used to trap large clouds of ions. (b) This potential is used to trap single ions or small crystals of ions. It provides better optical access, but the field far from the trap center has significant higher order terms. However, near the trap center the potential is harmonic to a good approximation.

where q is the charge of the ion, m is its mass and $\tilde{r}$ is the radius of the ring. With

$$a_i = \alpha_i \frac{4qV_0}{m\tilde{r}^2\Omega_f^2} \tag{2.3}$$

$$q_i = \alpha_i \frac{2qU_0}{m\tilde{r}^2\Omega_f^2} \tag{2.4}$$

$$\tau = \frac{\Omega_f}{2}t \tag{2.5}$$

this can be written as

$$\ddot{r}_i + (a_i - 2q_i \cos 2\tau) r_i = 0. \tag{2.6}$$

This equation is called the Mathieu equation. If the quadrupole potential is rotationally invariant about the z-axis, i.e. $\alpha_x = \alpha_y = -2\alpha_z$, the parameters a and q are given

by

$$a_z = -2a_{x,y} = -\frac{8q_eV_0}{m\tilde{r}^2\Omega_f^2} \tag{2.7}$$

$$q_z = -2q_{x,y} = -\frac{4q_eU_0}{m\tilde{r}^2\Omega_f^2}. \tag{2.8}$$

For certain values of q_i and a_i the solutions of this so-called Mathieu equation are stable, i.e. the value of $r_i(\tau)$ is limited to r_{max} for all times τ, i.e. the particle is trapped in a limited volume. Fig. 2.2, which is reffered to as a stability diagram, shows the areas of stable solutions for various q and a parameters [37]. The general

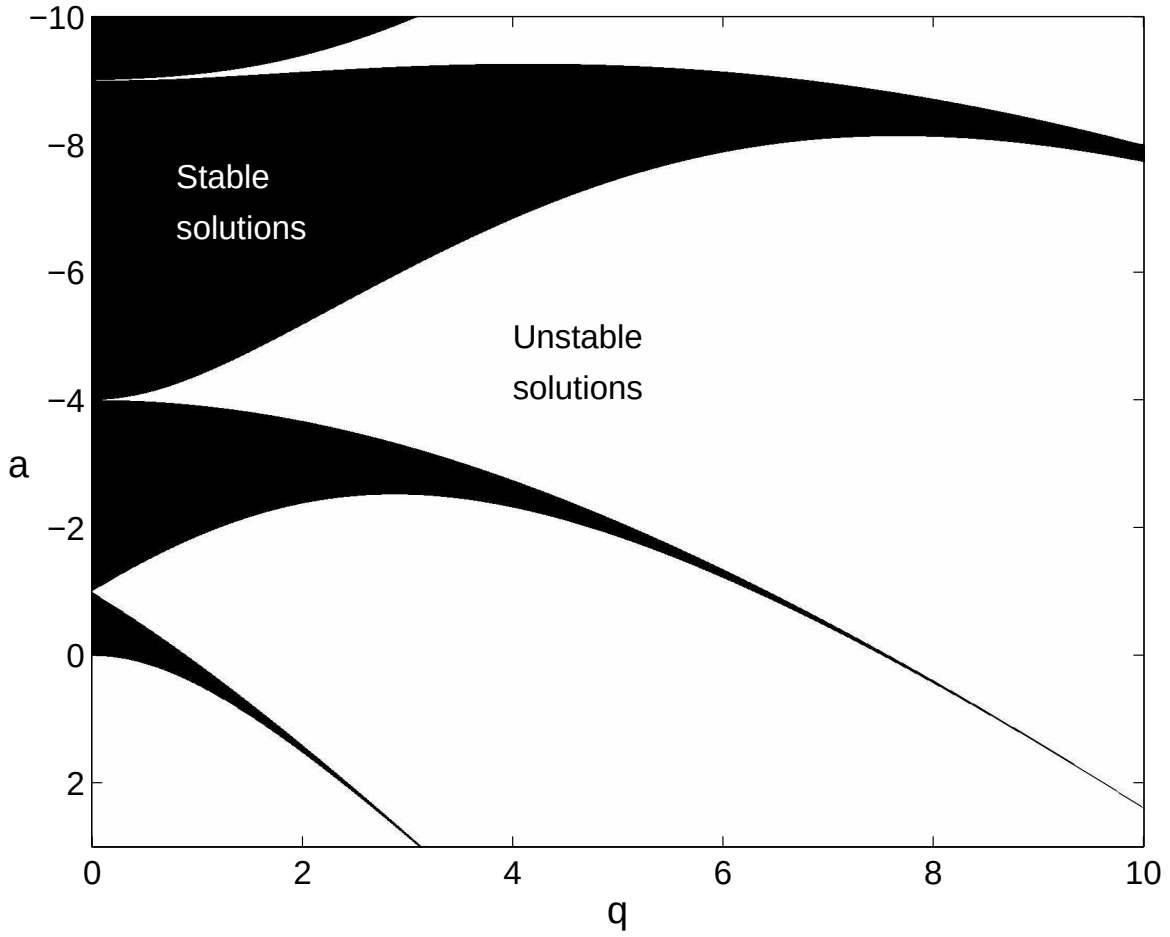

Figure 2.2: Stability diagram of the Mathieu equation in one direction

solution for r_i is then [37]

$$r_i(\tau) = A \sum_{n=-\infty}^{\infty} C_{2n} \cos{(2n+\beta_i)\tau} + B \sum_{n=-\infty}^{\infty} C_{2n} \sin{(2n+\beta_i)\tau}. \tag{2.9}$$

The coefficients C_{2n} and β_i do not depend on the initial conditions. These enter only into A and B.

In the case of trapped ions, only the first area of stability, which is shown in Fig. 2.3, is used because the voltages necessary for areas with higher a or q are techniqually difficult to reach. In the case of small parameters $a_i, q_i < 1$, approximate solutions are

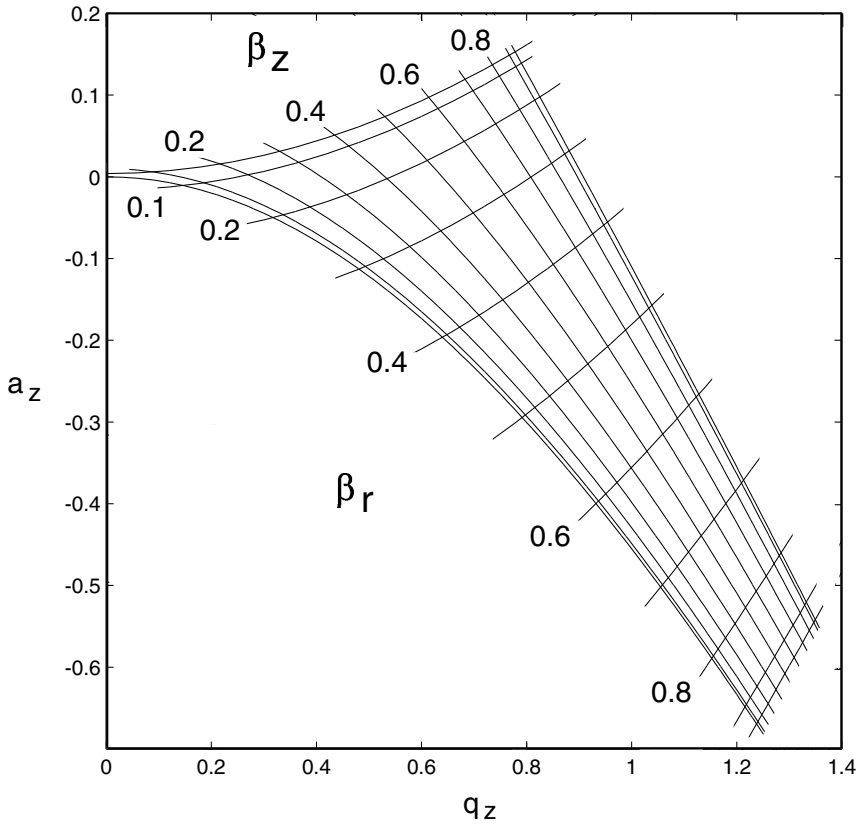

Figure 2.3: First area of stability

$$r_i(\tau) = r_i^0 \cos{(\omega_i \tau + \phi_i)} \left(1 + \frac{q_i}{2} \cos{(\Omega_f t)}\right). \tag{2.10}$$

The motion with frequency ω_i is called macro- or secular motion, the motion with Ω_f micro-motion. The frequency of the macro-motion ω_i is given by

$$\omega_i = \beta_i \frac{\Omega_f}{2} \text{ and } \beta_i^2 \approx a_i + \frac{q_i^2}{2}. \tag{2.11}$$

This approximation means that the ion moves in a harmonic pseudo-potential $\Psi = \frac{|\nabla\phi|^2}{4m\Omega_f^2}$, which is generated by the electric trap potential $\Phi(t, \vec{r})$.

The kinetic energy corresponding to the macro-motion of an ion can be reduced by means of laser cooling to a level which is comparable to $\hbar\omega_i$. Then the motion of the ion has to be quantized. By defining the usual creation and annihilation operators

$$\hat{a}_i^\dagger = \sqrt{\frac{m\omega_i}{2\hbar}}\hat{r}_i + \frac{i}{\sqrt{2m\hbar\omega_i}}\hat{p}_i \tag{2.12}$$

$$\hat{a}_i = \sqrt{\frac{m\omega_i}{2\hbar}}\hat{r}_i - \frac{i}{\sqrt{2m\hbar\omega_i}}\hat{p}_i \ , \tag{2.13}$$

where $\hat{r}_i$ and $\hat{p}_i$ are now position and momentum operators, the Hamiltonian

$$H = \sum_i \frac{\hat{p}_i^2}{2m} + \frac{1}{2}m{\omega_i}^2\hat{r}_i^2$$

can be cast into the standard form

$$H = \sum_i \hbar\omega_i \left(\hat{a}_i^\dagger\hat{a}_i + \frac{1}{2}\right) \ .$$

The eigenstates of the Hamilton operator, which are the so-called phonon number states $|n\rangle = |0\rangle, |1\rangle, |2\rangle, ...$, have an energy $E_n = \hbar\omega_i(n + 1/2)$.

The width of the zero-point wave function is then given by $\langle 0|{r_i}^2|0\rangle^{1/2} = \sqrt{\hbar/2m\omega_i}$. For example, a $^{138}Ba^+$ ion cooled to the ground state of a trap with $\omega = (2\pi)$ 750 kHz is localized to within 7 nm.

2.2 Excess micro-motion

These considerations assume that the zero of the DC part and the AC part of the potential are at the same position. In practice, this is often not the case due to stray electric fields caused by charged dielectrics or patch charges on the electrodes. The equation of motion (2.2) can be modified to account for this additional force.

$$\ddot{r}_i - \frac{\alpha_i q}{m\tilde{r}^2}(V_0 + U_0\cos\Omega_f t)r_i = \frac{qE_i}{m} \tag{2.14}$$

Solutions in the pseudo-potential approximation are then

$$r_i(\tau) = \left(r_i^M + r_i^0\cos(\omega_i\tau + \phi_i)\right)\left(1 + \frac{q_i}{2}\cos(\Omega_f t)\right). \tag{2.15}$$

The term $r_i^M\frac{q_i}{2}\cos(\Omega_f t)$ describes unwanted excess micro-motion. The static stray electric fields can be compensated and hence this excess micro-motion can be eliminated by applying a suitable combination of voltages to a set of compensation electrodes, see chapter 4.

2.3 Laser cooling of trapped ions

The macro-motion amplitude of a trapped ion can be reduced with different cooling techniques. These are, for example, buffer gas cooling, electrical coupling of the ion to a cold resonant circuit, which is used in Penning traps, and laser cooling. In Paul traps, laser cooling allows one to reduce the kinetic energy of the ions to the quantum regime.

The kinetic energy of an atom is reduced by laser excitation if the photons absorbed by the atom have lower energy than the photons reemitted by the atom. The energy difference is taken from the motion of the atom, therefore it is cooled. Many different laser cooling schemes exist. Simple methods are Doppler cooling [2, 3] and sideband cooling [5,38], more sophisticated methods, which rely on a multi-level structure of the atom, are, for example, polarization-gradient cooling [39–41], Raman cooling [42, 43] and EIT-cooling [44].

Two-level atoms can be cooled with a red-detuned laser, i.e. the laser frequency is set slightly below the atomic transition frequency. For simplicity, only cooling of one vibrational mode is described here. In a trap, three different regimes can be separated. These regimes depend on the ratios between the trap frequency ω_{tr}, the photon recoil frequency ϵ, and the natural linewidth Γ of the cooling transition. The photon recoil energy is given by

$$\hbar\epsilon = \frac{\hbar^2 k^2}{2m}, \tag{2.16}$$

with $k = \omega_0/c$ and the atomic mass m, is the average kinetic energy transferred to an atom by absorption or emission of a photon with frequency ω_0.

The ratio between ϵ and the trap frequency ω_{tr} is used to define the Lamb-Dicke parameter $\eta = \sqrt{\epsilon/\omega_{tr}}$. The Lamb-Dicke parameter can also be defined as the ratio between the width of the ion ground state in the trap $\langle 0|{r_i}^2|0\rangle^{1/2} = \sqrt{\hbar/2m\omega_i}$ and the wavelength of the resonant light $\lambda_0/2\pi = c/\omega_0$

$$\eta = \frac{\sqrt{\hbar/2m\omega_i}}{\lambda_0/2\pi}. \tag{2.17}$$

When the ion is not in the ground state, it is also useful to define a modified Lamb-Dicke parameter

$$\eta_{mod} = \sqrt{2n+1}\,\eta \tag{2.18}$$

1. **Quasi free particles**
   When the Lamb-Dicke parameter η_{mod} is greater than one, the atom can be treated like a free particle. The atom is cooled by momentum transfer from the photons of the light field as in Doppler cooling of free atoms [2].

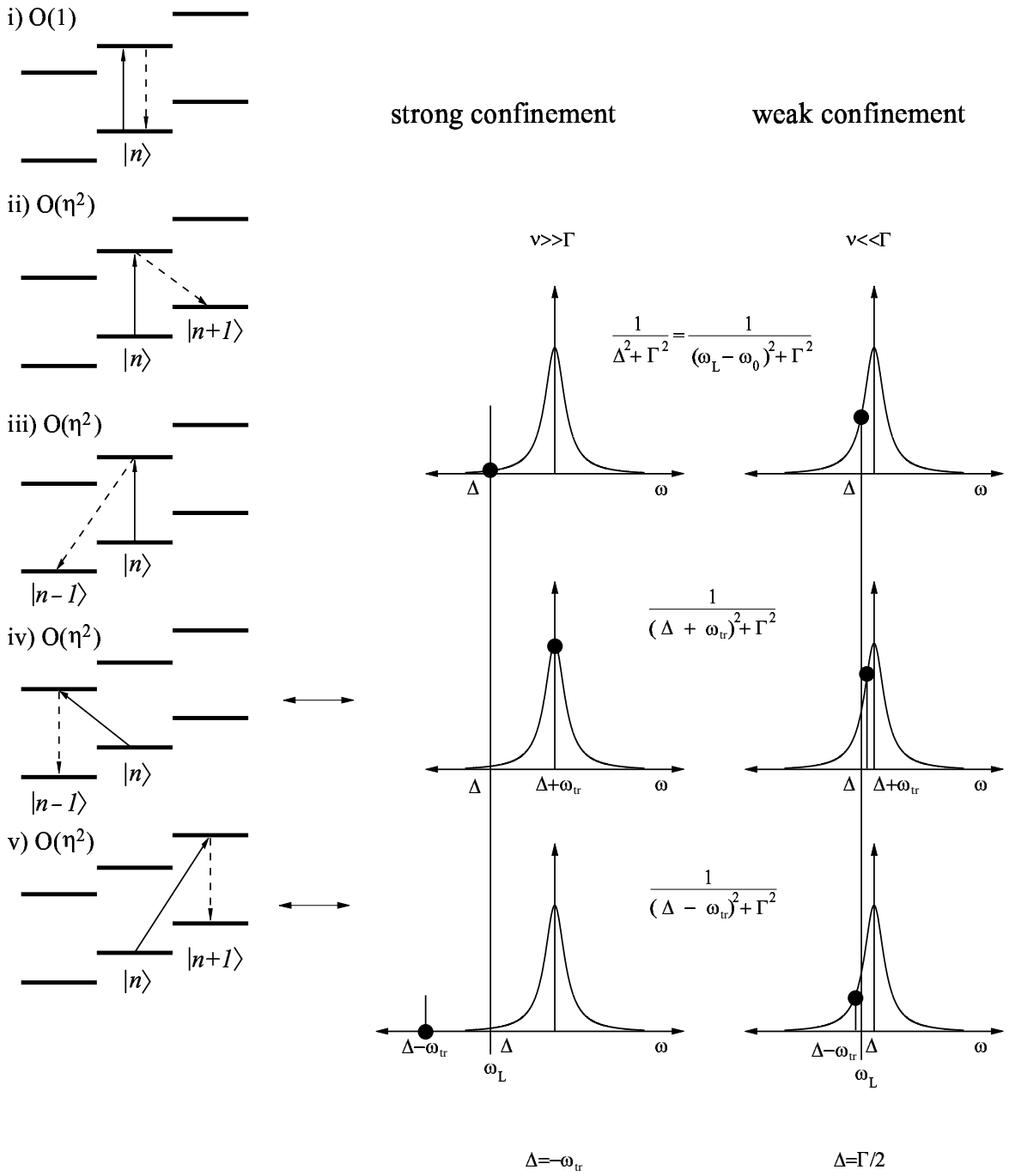

Figure 2.4: Left side: possible optical absorption-emission cycles in the Lamb-Dicke regime. Right side: Lorentzian line shape of the cooling transition with a natural linewidth Γ and the trap frequency ω_{tr}.

2. **Lamb-Dicke regime**
The regime $\eta_{mod} < 1$ is called the Lamb-Dicke regime. Absorption and emission processes are best viewed in the rest frame of the atom. Then, the laser light seen by the atom is frequency-modulated with the trap frequency. In the Lamb-Dicke regime the spectrum of the laser light seen by the atom consists only of the carrier at frequency ω_l and the first-order sidebands at $\omega_l \pm \omega_{tr}$.

Five processes, as shown in Fig. 2.4, can happen during absorption and spontaneous emission of a photon. The detuning Δ_l of the laser from the atomic resonance enters into their relative probabilities.

i. Absorption and emission without change of the phonon number. This process is the most likely one with a relative probability of $p_i \approx 1/(\Delta_l^2+(\Gamma/2)^2)$.

ii. Absorption with $\Delta n = 0$ and emission with $\Delta n = +1$ with probability $p_{ii} = (n+1)\eta^2/(\Delta_l^2 + (\Gamma/2)^2)$.

iii. Absorption with $\Delta n = 0$ and emission with $\Delta n = -1$ with probability $p_{iii} = n\eta^2/(\Delta_l^2 + (\Gamma/2)^2)$.

iv. Absorption with $\Delta n = -1$ and emission with $\Delta n = 0$ with probability $p_{iv} = n\eta^2/[(\Delta_l + \omega_{tr})^2 + (\Gamma/2)^2]$.

v. Absorption with $\Delta n = +1$ and emission with $\Delta n = 0$ with probability $p_v = (n+1)\eta^2/[(\Delta_l - \omega_{tr})^2 + (\Gamma/2)^2]$.

The process i) does not change the motional state of the trapped atom, i.e. it does not contribute to cooling or heating. The transitions ii) and v) increase the phonon number by 1, while the processes iii) and iv) cool the atom by $\Delta n = 1$. The heating emission ii) is more likely than the cooling emission iii) by a factor $(n+1)/n$. This is also true for the absorptions, but these are additionally weighted with the Lorentzian line shape of the transition. When the laser is red detuned, i.e. $\Delta_l < 0$, the weight of the cooling process iv) can be made larger than that of the heating transition v).

Now two cases have to be examined. When the trap frequency ω_{tr} is larger than the natural linewidth Γ of the atom, that is the so called strong confinement regime, the sidebands are resolved because the atom undergoes many oscillations during one lifetime of the excited level. In the weak confinement case, i.e. $\omega_{tr} < \Gamma$, the sidebands are not resolved. This corresponds to the case that the lifetime of the excited level is smaller than the oscillation period.

a) **Sideband cooling**
In the limit of strong confinement, the atom sees the motional sidebands resolved. Then the laser can be tuned such that the atom in its rest frame is only resonant with the upper sideband, i.e. the carrier is below the atomic resonance frequency. In this limit, only process iv.) is resonant,

processes iii.) and v.) are off-resonant. In this case the absorption of one photon lowers the atomic kinetic energy by one phonon $\hbar\omega_{tr}$. In the Lamb-Dicke regime, the probabilities of changing the phonon number during the spontaneous emission by ± 1 are $(n+1)\eta_{mod}^2$ and $n\eta_{mod}^2$, respectively, i.e. in most cases n is not changed. Thus, in an absorption-emission cycle the atom is cooled by one phonon. The cooling limit for sideband cooling is given by the equilibrium of resonant cooling transitions and off-resonant heating. Its value is

$$\langle n \rangle_{SB} = \frac{\Gamma^2}{4\omega_{tr}^2} \left\{ \frac{\alpha}{\cos^2\theta} + \frac{1}{4} \right\} \tag{2.19}$$

with the angle θ between the axis of the vibrational mode and the direction of the laser beam $\vec{k}$, and with the geometrical factor α which depends on the spatial distribution of the spontaneous emission. In the case of an isotropic distribution, $\alpha = 1/3$ [45].

b) **Weak confinement**
The atom does not resolve the sidebands of the laser beam. Optimal cooling is achieved for $\Delta_l = -\Gamma/2$ [45]. The cooling limit is then

$$\langle n \rangle = \frac{1}{2} \left[\left(\frac{\alpha + \cos^2\theta}{\cos^2\theta} \right) \frac{\Gamma/2}{\omega_{tr}} \right]. \tag{2.20}$$

The cooling limit is the same as for Doppler cooling of free particles. Therefore this process is referred to as Doppler cooling, although the mechanisms in the two cases are different and have to be distinguished.

For the considered two-level system, the cooling rate, i.e. the damping rate of the oscillation, can be calculated analytically [45]. The cooling rate W_{max} at $\Delta_l = -\Gamma/2$ is on the order of $\eta\omega_{tr}$.

The cooling principle, as described above, also holds for multi-level atoms, but the final temperatures and the cooling rates differ due to the larger number of possible transitions. For the Ba^+ ion, which is an 8-level system, it is not possible to find analytical expressions for the temperature and the cooling rate. A detailed numerical analysis of this system can be found in [46]. However, in the limit of weak confinement the cooling rate can be estimated assuming a radiation pressure force on the atom, given by

$$F = \hbar k \sum_i \Gamma_i \rho_{ee}(\Delta_i - k_i v) \tag{2.21}$$

where v is the velocity of the oscillating atom and the excited state probability $\rho_{ee}(\Delta_i - k_i v)$ for the different lasers k_i with detunings Δ_i can be calculated from the optical

Bloch equations [45]. If the velocity is small, the radiation pressure force can be linearised around $v = 0$:

$$F = F_0 + \left.\frac{\mathrm{d}F}{\mathrm{d}v}\right|_{v=0} v = F_0 - \alpha v M \tag{2.22}$$

yielding a constant force plus a friction term with the cooling rate α. For negative detunings Δ_i the cooling rate α is given by:

$$\alpha = 2 \sum_i \frac{\hbar k_i^2}{2M} \Gamma_i \left.\frac{\partial \rho_{ee}}{\partial \Delta_i}\right|_{\Delta_i} . \tag{2.23}$$

The cooling rate and the cooling limit depend on $\frac{\partial \rho_{ee}}{\partial \Delta_i}$, yielding the same results for cooling of a 2-level atom.

3 Light-matter interaction

The experiments described in this thesis are carried out with single positively charged Barium ions (Ba^+). With the help of a Paul trap and laser cooling, as described in chapter 2, these ions are confined to a volume whose size is smaller than the wavelength of the fluorescence light in all 3 dimensions. The ion is continuously excited with lasers, and the properties of its fluorescence light are investigated with various interferometric techniques. This chapter describes the level structure of the Ba^+ ion, the theoretical modeling of the light-matter interaction for the example of Ba^+, and some of the expected properties of the fluorescence light.

3.1 The Ba^+ ion

For the experiments only the isotope ^{138}Ba, which has no nuclear spin, is used. Its natural abundance is 71.7% (Table 3.1).

Isotope		^{130}Ba	^{132}Ba	^{134}Ba	^{135}Ba	^{136}Ba	^{137}Ba	^{138}Ba
nuclear spin I	$\hbar$	0	0	0	3/2	0	3/2	0
abundance	%	0.1	0.1	2.4	6.6	7.8	11.3	71.7

Table 3.1: Natural isotope distribution [47] of Barium.

The electron configuration of Ba^+ is equivalent to the noble gas Xenon with an additional valence electron ($[Xe]6^2S_{1/2}$). The energy levels relevant for the experiments are $S_{1/2}$, $P_{1/2}$ and $D_{3/2}$. These levels form a lambda (Λ) system with dipole-allowed transitions from $S_{1/2}$ to $P_{1/2}$ and from $D_{3/2}$ to $P_{1/2}$. The transition from $S_{1/2}$ to $D_{3/2}$ is dipole-forbidden but quadrupole-allowed with the natural lifetime of the $D_{3/2}$ level being 79.8±4.6 s [48]. The level scheme is shown in Fig. 3.1 and the relevant transitions are listed in table 3.2. The levels have a Zeeman substructure which all together forms an 8-level system. The Zeeman substructure is shown in Fig. 3.2 together with the possible laser-induced transitions for a light polarization perpendicular to the magnetic field, as it is the situation in the experiments.

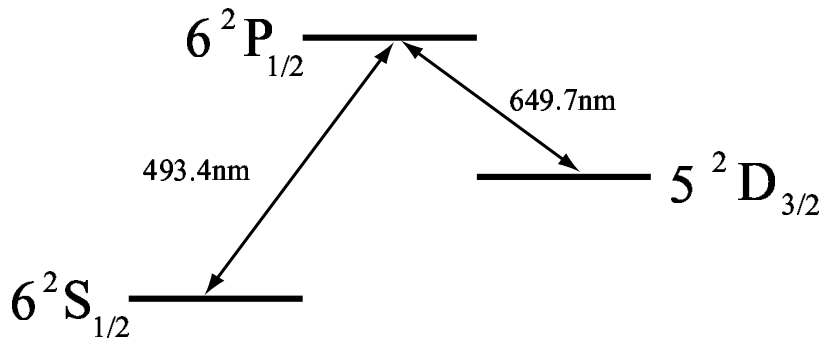

Figure 3.1: Levels of the Ba^+ ion used in the experiment and transition wavelengths

Transition	λ_{air} (nm)	Γ_{nat} (MHz)	A_{exp} (s^{-1})
$6^2S_{1/2} \rightleftharpoons 6^2P_{1/2}$	493.4	15.1	$95 \pm 7 \cdot 10^6$
$6^2P_{1/2} \rightleftharpoons 5^2D_{3/2}$	649.7	5.3	$33 \pm 4 \cdot 10^6$
$5^2D_{3/2} \rightleftharpoons 6^2S_{1/2}$	2051	$0.4 \cdot 10^{-8}$	$12.5 \pm 0.7 \cdot 10^{-3}$

Table 3.2: Transitions between the relevant energy levels with the respective wavelengths, natural linewidths and Einstein A-coefficients [48, 49].

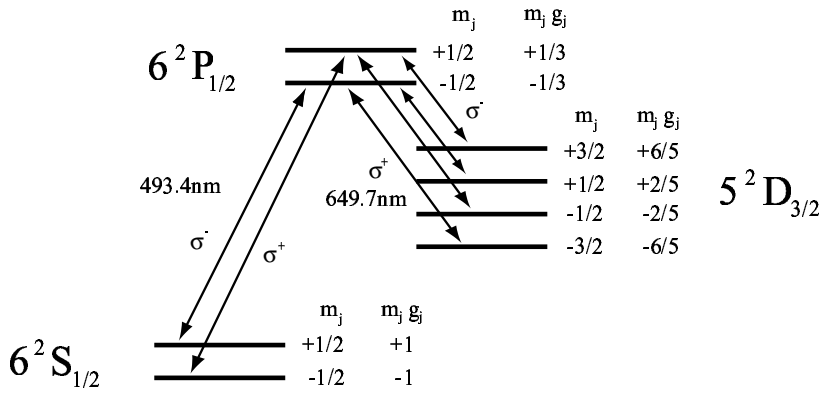

Figure 3.2: Zeeman substructure of the relevant Ba^+ levels. The laser transitions indicated by arrows can be excited when the light polarization is linear and orthogonal to the magnetic field.

3.2 Bloch equations

A theoretical model for describing the atom-laser interaction is presented in this section.

For simplicity, only the model for a three-level Λ-system interacting with two coherent light fields is discussed. This model can be easily extended to an 8-level system such as the Ba^+ ion [50].

3.2.1 Interaction of a Λ-system with coherent light fields

The system described in this paragraph is shown in Fig. 3.3. Because coherent laser

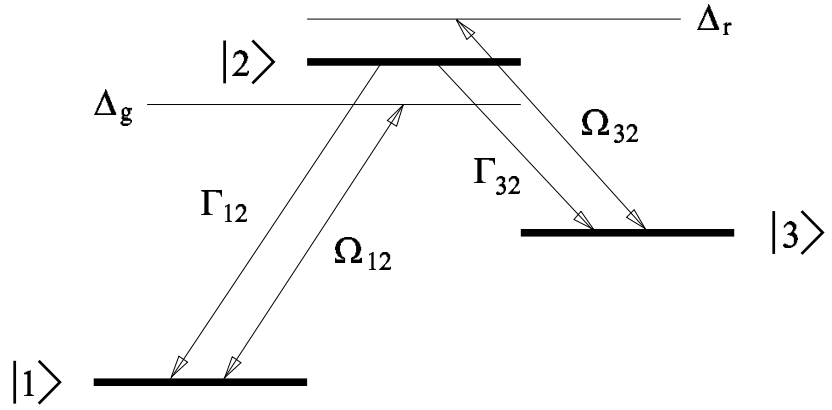

Figure 3.3: Three level system with the atomic eigenstates $|1\rangle, |2\rangle, |3\rangle$ and the coherent light fields $\hat{\vec{E}}_g$ and $\hat{\vec{E}}_r$ with Rabi frequencies $\Omega_{12,32}$ and detunings $\Delta_{12,32}$.

light fields with high photon numbers are considered, only the atom is described quantum mechanically while the two lasers are treated as classical electromagnetic waves $\vec{E}_g \sin(\omega_g t)$ and $\vec{E}_r \sin(\omega_r t)$ with a laser linewidth Γ_g and Γ_r, respectively. The spontaneous emission of photons is treated as a decay from $|2\rangle$ to $|1\rangle$ and $|3\rangle$ with the rates Γ_{12} and Γ_{32}.

The Hamiltonian of the atom, using the states $|1\rangle$, $|2\rangle$ and $|3\rangle$ as the basis, is defined by

$$\hat{\mathcal{H}}_{atom}|a\rangle = \hbar\omega_a|a\rangle \text{ with } a = 1, 2, 3 \tag{3.1}$$

with ω_a being the atomic Bohr frequencies. It is assumed that the atom-laser interaction is restricted to the dipole interaction. Then the interaction Hamiltonian can be written as:

$$\begin{aligned}\hat{\mathcal{H}}_{int} = -\{&\vec{D}_{12} \cdot \vec{E}_g i[|2\rangle\langle 1|e^{-i\omega_g t} - |1\rangle\langle 2|e^{i\omega_g t}] + \\ &\vec{D}_{32} \cdot \vec{E}_r i[|2\rangle\langle 3|e^{-i\omega_r t} - |3\rangle\langle 2|e^{i\omega_r t}]\}\end{aligned} \tag{3.2}$$

where $\vec{D}_{12}$ and $\vec{D}_{32}$ are the dipole matrix elements for the transition from $|1\rangle$ to $|2\rangle$ and $|3\rangle$ to $|2\rangle$, respectively. Here the terms which rotate at twice the optical

frequency and the non-resonant terms, e.g. $\vec{D}_{12} \cdot \vec{E}_r$, are neglected (rotating wave approximation) [50–52].

The Hamiltonian can also be written in a matrix representation with

$$\begin{pmatrix} c_1 \\ c_2 \\ c_3 \end{pmatrix} \equiv c_1|1\rangle + c_2|2\rangle + c_3|3\rangle \tag{3.3}$$

$$\mathcal{H}_{atom} = \hbar \begin{pmatrix} \omega_{12} & 0 & 0 \\ 0 & 0 & 0 \\ 0 & 0 & \omega_{32} \end{pmatrix} \tag{3.4}$$

with $\omega_{12} = \omega_1 - \omega_2$ and $\omega_{32} = \omega_3 - \omega_2$. The energy zero has been set to $|2\rangle$. The interaction Hamilton is then given by

$$\mathcal{H}_{int} = \hbar \begin{pmatrix} 0 & \frac{\Omega_{12}}{2} e^{+i\omega_g t} & 0 \\ \frac{\Omega_{12}}{2} e^{-i\omega_g t} & 0 & \frac{\Omega_{32}}{2} e^{-i\omega_r t} \\ 0 & \frac{\Omega_{32}}{2} e^{+i\omega_r t} & 0 \end{pmatrix} \tag{3.5}$$

where

$$\hbar\Omega_{12} := \vec{D}_{12} \cdot \vec{E}_g \tag{3.6}$$

$$\hbar\Omega_{32} := \vec{D}_{32} \cdot \vec{E}_r \tag{3.7}$$

The quantities Ω_{12} and Ω_{32} are called Rabi frequencies and denote the strength of the coupling between the atom and the electric field.

The complete Hamiltonian is finally

$$\mathcal{H} = \hbar \begin{pmatrix} \omega_{12} & \frac{\Omega_{12}}{2} e^{+i\omega_g t} & 0 \\ \frac{\Omega_{12}}{2} e^{-i\omega_g t} & 0 & \frac{\Omega_{32}}{2} e^{-i\omega_r t} \\ 0 & \frac{\Omega_{32}}{2} e^{+i\omega_r t} & \omega_{32} \end{pmatrix}. \tag{3.8}$$

The Hamiltonian does not describe the spontaneous decay of the upper level into the lower levels. The spontaneous decay can be represented as an interaction of the atom with the vacuum field. For this approach it would be necessary to introduce the electro-magnetic field fully quantum-mechanically [51, 52]. However, to understand the experiments of this thesis it is not necessary to use a full quantum-mechanical treatment of the decay. It is sufficient to treat the spontaneous decay as a rate Γ_{21} (Γ_{23}) with which the state $|2\rangle$ decays into $|1\rangle$ ($|3\rangle$). The resulting state of the atom is no longer a pure state and one can use the density matrix formalism.

3.2.2 Density matrix formalism

The density operator $\hat{\rho}$, written in the basis of atomic eigenstates $|a\rangle$, is

$$\hat{\rho} = \sum_{a,b=1,2,3} \rho_{ab}|a\rangle\langle b|. \tag{3.9}$$

The trace $\mathrm{Tr}(\hat{\rho})$, i.e. the probability to find the atom in any one of the states $|1\rangle, |2\rangle, |3\rangle$, is one.

The time evolution of the density operator is governed by the Liouville equation

$$\frac{d\hat{\rho}}{dt} = -\frac{i}{\hbar}[\mathcal{H}, \hat{\rho}] + \mathcal{L}_{damp}(\hat{\rho}) \tag{3.10}$$

where now the first part corresponds to the Schrödinger equation and $\mathcal{L}_{damp}$ describes the spontaneous decay of the upper state. The operator $\mathcal{L}_{damp}$ has the following general form [53]

$$\mathcal{L}_{damp}(\hat{\rho}) = -\frac{1}{2}\sum_m [\hat{C}_m^\dagger \hat{C}_m \hat{\rho} + \hat{\rho}\hat{C}_m^\dagger \hat{C}_m - 2\hat{C}_m \hat{\rho} \hat{C}_m^\dagger]. \tag{3.11}$$

The operators $\hat{C}_m$ describe the different dissipative processes. The first two terms $\hat{C}_m^\dagger \hat{C}_m \hat{\rho}$ and $\hat{\rho}\hat{C}_m^\dagger \hat{C}_m$ describe the decay of the excited levels, where the term $2\hat{C}_m \hat{\rho} \hat{C}_m^\dagger$, which is called feeding term, describes the decay *into* the lower states. In our case this is the decay $|2\rangle \rightarrow |1\rangle$ and $|2\rangle \rightarrow |3\rangle$. Also, the decoherence through the finite bandwidth Γ_g and Γ_r of the driving laser fields can be included in $\mathcal{L}_{damp}$ [14]

$$\hat{C}_{21} = \sqrt{\Gamma_{21}}|1\rangle\langle 2| \tag{3.12}$$
$$\hat{C}_{23} = \sqrt{\Gamma_{23}}|3\rangle\langle 2| \tag{3.13}$$
$$\hat{C}_g = \sqrt{2\Gamma_g}|1\rangle\langle 1| \tag{3.14}$$
$$\hat{C}_r = \sqrt{2\Gamma_r}|3\rangle\langle 3|. \tag{3.15}$$

By writing

$$\frac{d\hat{\rho}}{dt} = \mathcal{L}\hat{\rho(t)} \tag{3.16}$$

with

$$\mathcal{L}\hat{\rho} = -\frac{i}{\hbar}[\mathcal{H}, \hat{\rho}] + \mathcal{L}_{damp}(\hat{\rho}) \tag{3.17}$$

the density operator ρ at the time t can now be expressed in terms of $\hat{\rho(0)}$ by

$$\hat{\rho(t)} = \mathrm{e}^{\mathcal{L}t}\hat{\rho(0)}. \tag{3.18}$$

Finally, we transform the system into the rotating frame of the laser light fields with

$$U = \begin{pmatrix} e^{-i\omega_g t} & 0 & 0 \\ 0 & 1 & 0 \\ 0 & 0 & e^{-i\omega_r t} \end{pmatrix} \tag{3.19}$$

and get the transformed density and Hamilton operators

$$\hat{\rho}' = U\hat{\rho}U^\dagger \tag{3.20}$$

$$\mathcal{H}' = U\mathcal{H}U^\dagger - i\hbar U\frac{dU^\dagger}{dt}. \tag{3.21}$$

The resulting Hamiltonian $\mathcal{H}'$ is

$$\mathcal{H}' = \hbar \begin{pmatrix} \Delta_g & \Omega_{12}/2 & 0 \\ \Omega_{12}/2 & 0 & \Omega_{32}/2 \\ 0 & \Omega_{32}/2 & \Delta_r \end{pmatrix} \tag{3.22}$$

with the detunings

$$\Delta_g = \omega_g - \omega_{12} \tag{3.23}$$

$$\Delta_r = \omega_r - \omega_{32}. \tag{3.24}$$

The damping terms remain unchanged.

3.2.3 Optical Bloch equations

The Liouville equation (3.16) can be transformed into a system of linear equations by setting

$$\vec{\rho} := (\rho_{11}, \rho_{12}, ..., \rho_{23}, \rho_{33}) \tag{3.25}$$

$$\frac{d\vec{\rho}_i}{dt} = \sum_j \mathrm{M}_{ij}\vec{\rho}_j \tag{3.26}$$

where $\rho_{ab} = \langle a|\hat{\rho}|b\rangle$. These equations are called the optical Bloch equations. The matrix M is uniquely determined by $\mathcal{L}$ in Eq. (3.16), i.e. it contains all information relevant for the evolution of the system, i.e. the laser intensities, detunings, and decay constants.

According to (3.16), the time evolution $\vec{\rho}(t)$ with a given $\vec{\rho}(0)$ is

$$\vec{\rho}(t) = \exp(\mathrm{M}t)\vec{\rho}(0). \tag{3.27}$$

The trace of the density matrix must be one at all times (normalization condition):

$$\sum_i \rho_{ii}(t) = 1. \tag{3.28}$$

The steady-state solution ($\vec{\rho}(\infty) = \text{const.} \Leftrightarrow \dot{\vec{\rho}} = 0$) is given by

$$0 = \sum_j \mathrm{M}_{ij}\vec{\rho}_j. \tag{3.29}$$

To solve Eq. (3.29) with the correct normalization, one of the equations in (3.29) must be replaced by the normalization condition (3.28). The time evolution of $\vec{\rho}(t)$ and the steady-state solution $\vec{\rho}(\infty)$ can now be calculated numerically with a computer program.

3.3 Excitation spectra

An excitation spectrum is a record of the fluorescence intensity versus the detuning of one of the lasers. The average rate of photons emitted by a single Λ-system atom is given by

$$N = N_g + N_r \tag{3.30}$$
$$N_g = \Gamma_{21}\ \rho_{22} \tag{3.31}$$
$$N_r = \Gamma_{23}\ \rho_{22}. \tag{3.32}$$

The fluorescence light is spectrally integrated and measured with a photon counting detector. In this experiment only the fluorescence at 493 nm, N_g, is detected, the fluorescence at 650 nm is blocked with a filter. With the optics and the detectors used to collect the light, about 1% of the green fluorescence can be recorded.

If the time over which data are accumulated at a fixed set of parameters (typically on the order of 100 ms) is much longer than the time scale for the internal dynamics of the atom (on the order of 1 μs), the population of ρ_{22} for any set of parameters can be calculated from the steady-state solutions of the optical Bloch equations. Figure 3.4 shows a calculated spectrum where the red laser frequency is scanned while all other parameters are held fixed. The spectrum shows the expected Lorenzian line shape with an extra feature around $\Delta_r = \Delta_g$. There, the ion is pumped into a superposition state of $|1\rangle$ and $|3\rangle$ while state $|2\rangle$ is not populated. The steady-state solution of the Bloch equations at $\Delta_r = \Delta_g$ is:

$$\rho = \begin{pmatrix} \frac{\Omega_{12}^2}{\Omega_{12}^2+\Omega_{32}^2} & 0 & -\frac{\Omega_{12}\Omega_{32}}{\Omega_{12}^2+\Omega_{32}^2} \\ 0 & 0 & 0 \\ -\frac{\Omega_{12}\Omega_{32}}{\Omega_{12}^2+\Omega_{32}^2} & 0 & \frac{\Omega_{32}^2}{\Omega_{12}^2+\Omega_{32}^2} \end{pmatrix}. \tag{3.33}$$

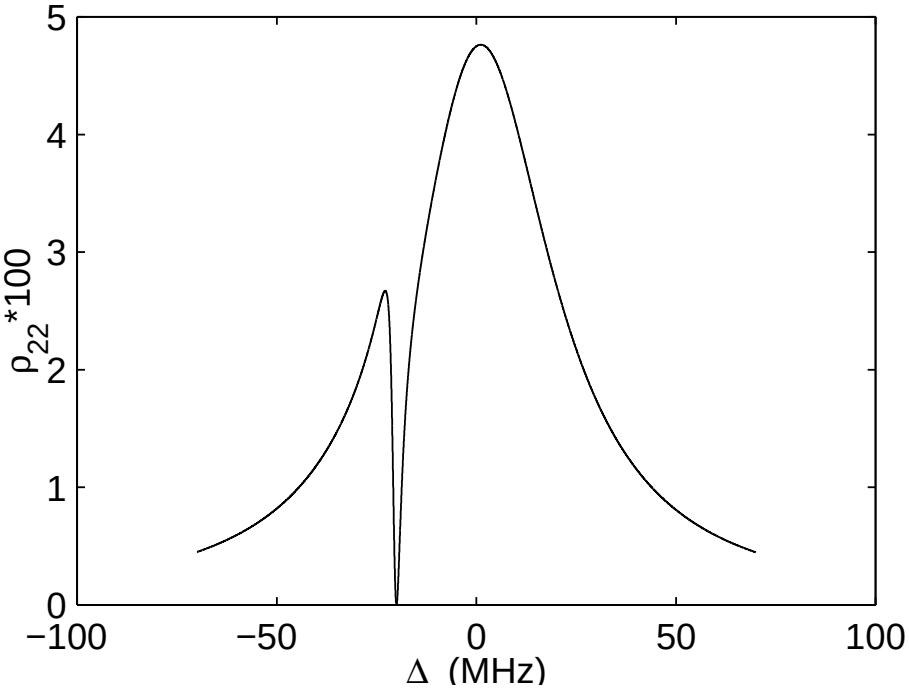

Figure 3.4: Excitation spectrum of a three level system. Parameters are $\Delta_g/2\pi$ = -20 MHz, $\Omega_{12}/2\pi = 10$ MHz, $\Omega_{23}/2\pi = 5$ MHz, $\Gamma_g = \Gamma_r = 0$.

This phenomenon is often called 'dark resonance' because the fluorescence vanishes. The perfect superposition of the states $|1\rangle$ and $|3\rangle$, i.e. $\rho_{22} = 0$, is perturbed by phase fluctuations of the lasers which in the model are represented by the laser linewidth parameters Γ_g and Γ_r. Figure 3.5 shows the dependence of the depth of the dark resonance on the laser linewidths. Thus, the depth of an experimentally measured dark resonance contains information about the linewidths of the two lasers. They can, however, not be determined individually, only the common linewidth $\Gamma_g + \Gamma_r$ (assuming that the phase fluctuations are not correlated) can be found in this way.

3.4 Correlation functions

An excitation spectrum only reveals information about the steady-state solution of the Bloch equations and the corresponding measurements for long integration times. Information about the internal dynamics can be gained from the correlation functions $g^{(1)}(\tau)$ and $g^{(2)}(\tau)$ of the fluorescence field. Here, only the correlation functions of the green fluorescence are discussed.

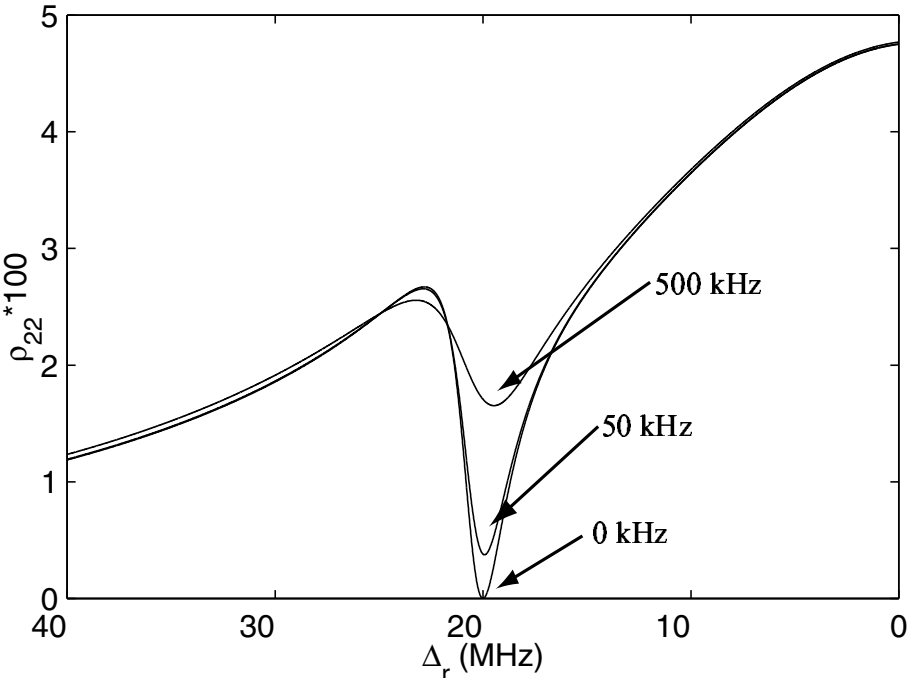

Figure 3.5: Depth of the dark resonance for increasing laser linewidth $\Gamma_r = 0,\ 50$ kHz, 500 kHz.

The first order correlation function [51]

$$g^{(1)}(\tau) = \frac{< \vec{E}_g^-(t)\vec{E}_g^+(t+\tau) >}{< \vec{E}_g^-(t)\vec{E}_g^+(t) >} \tag{3.34}$$

describes the coherence of the fluorescence light, and its Fourier transform is the spectrally resolved intensity distribution of the fluorescence light [51]. The brackets $< \ ... \ >$ denote the expectation value of the operators. The time t is assumed to be sufficiently long for the atom and the field to have arrived at a steady state. The degree of coherence is then independent of t.

The probability of detecting a photon at a time $t+\tau$ after a photon has been detected at time t, is described by the second order coherence function

$$g^{(2)}(\tau) = \frac{< \vec{E}_g^-(t)\vec{E}_g^-(t+\tau)\vec{E}_g^+(t+\tau)\vec{E}_g^+(t) >}{< \vec{E}_g^-(t)\vec{E}_g^+(t) >^2}. \tag{3.35}$$

The electric field $\vec{E}_g$ of the green fluorescence light at the position $\vec{r}$ is given by:

$$\vec{E}_g^+(t,\vec{r}) = -\frac{e\omega_0^2 D_{12}\sin\alpha}{4\pi_{12}\epsilon_0 c^2|\vec{r}|}\hat{\pi}\left(t - \frac{|\vec{r}|}{c}\right) \tag{3.36}$$

with the angle α being that between the atomic dipole and the direction of observation. The atomic flip operator is $\hat{\pi}(t) = |1\rangle\langle 2|(t)$.

The correlation functions $g^{(1)}$ and $g^{(2)}$ are now

$$g^{(1)}(\tau) = \frac{<\hat{\pi}^\dagger(t)\hat{\pi}(t+\tau)>}{<\hat{\pi}^\dagger(t)\hat{\pi}(t)>} \tag{3.37}$$

$$g^{(2)}(\tau) = \frac{<\hat{\pi}^\dagger(t)\hat{\pi}^\dagger(t+\tau)\hat{\pi}(t+\tau)\hat{\pi}(t)>}{<\hat{\pi}^\dagger(t)\hat{\pi}(t)>^2}. \tag{3.38}$$

The values of the correlation functions can be calculated from the Bloch equations using the quantum regression theorem [54, 55] as follows:

Let an arbitrary operator $\hat{A}_{ij}$ be defined as $\hat{A}_{ij} = |i\rangle\langle j|$. Its single-time expectation value $< \hat{A}(t) >$ is

$$< \hat{A}_{ij}(t) >= \mathrm{Tr}[\hat{A}_{ij}(0)\rho(t)]. \tag{3.39}$$

The two-time expectation value $G_{ij}(t,\tau)$ is defined as $G_{ij}(t,\tau) =< \hat{B}(t)\hat{A}_{ji}(t+\tau)\hat{C}(t) >$ with $\hat{B}$ and $\hat{C}$ arbitrary operators $\hat{A}_{nm}$ (or 1). In the stationary state $G(t,\tau)$ does not depend on t. Then $G(\tau)$ can be calculated with the quantum regression theorem

$$G(\tau) = \mathrm{e}^{\mathcal{L}\tau}G(0), \tag{3.40}$$

where the initial conditions are given by the the single-time expectation value

$$G_{ij}(0) =< \hat{B}(t)\hat{A}_{ji}(t)\hat{C}(t) > . \tag{3.41}$$

One gets the first-order correlation function $g^{(1)}(\tau)$ by setting $\hat{B} = \hat{\pi}^\dagger = |2\rangle\langle 1|$, $\hat{A} = \hat{\pi} = |1\rangle\langle 2|$ and $\hat{C} = 1$, such that

$$g^{(1)}(\tau) = \frac{G_{21}(\tau)}{G_{21}(0)}. \tag{3.42}$$

For the second-order correlation function $g^{(2)}(\tau)$, one sets $\hat{B} = \hat{\pi}^\dagger = |2\rangle\langle 1|$, $\hat{A} = \hat{\pi}^\dagger\hat{\pi} = |2\rangle\langle 2|$ and $\hat{C} = \hat{\pi} = |1\rangle\langle 2|$ such that a similar relation is found:

$$g^{(2)}(\tau) = \frac{G_{22}(\tau)}{G_{22}(0)}. \tag{3.43}$$

The value of $g^{(1)}(\tau)$ and $g^{(2)}(\tau)$ can now be calculated numerically. Fig. 3.6 shows $g^{(1)}$ calculated for two different sets of laser parameters. The second order coherence function $g^{(2)}$ for the same set of parameters is shown in Fig. 3.7.

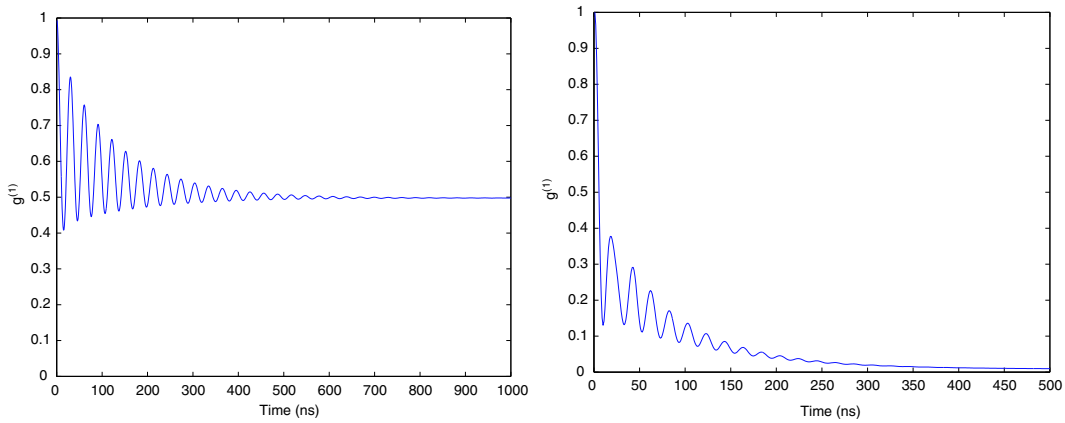

(a) (b)

Figure 3.6: Correlation function $\mathrm{Re}(g^{(1)})$ with $\Omega_{32}/\Gamma_{32} = 1$, $\Delta_{12}/2\pi = -5$ MHz, $\Delta_{32}/2\pi = 0$ MHz, (a) $\Omega_{12}/\Gamma_{12} = 1$, and (b) $\Omega_{12}/\Gamma_{12} = 4$. The laser line width has been set to zero.

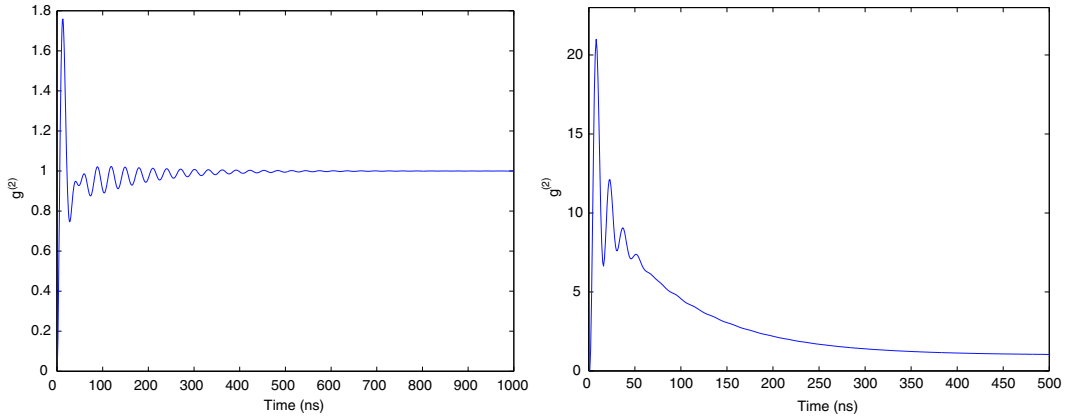

(a) (b)

Figure 3.7: Correlation function $\mathrm{Re}(g^{(2)})$ with $\Omega_{32}/\Gamma_{32} = 1$, $\Delta_{12}/2\pi = -5$ MHz, $\Delta_{32}/2\pi = 0$ MHz, (a) $\Omega_{12}/\Gamma_{12} = 1$, and (b) $\Omega_{12}/\Gamma_{12} = 4$. The laser linewidth has been set to zero.

3.5 Spectrum of resonance fluorescence and effects of motion

In this section, first the spectrum of resonance fluorescence of an atom at rest is discussed. Then the effects of motion in a Paul trap are included.

3.5.1 Spectrum of an atom at rest

The spectral intensity distribution of the fluorescence light of an atom at rest is given by the Fourier transform of the first-order coherence function $g^{(1)}(\tau)$ [52]

$$S(\omega) = \frac{1}{\pi}\mathrm{Re}\int_0^\infty g^{(1)}(\tau)e^{-i\omega\tau}d\tau. \tag{3.44}$$

In a two-level system, this can be solved analytically in the limit of very small laser intensity, i.e. $\Omega \ll \Gamma/4$, and high Rabi frequency, i.e. $\Omega \gg \Gamma/4$.
In the low field limit, i.e. $\Omega \ll \Gamma/4$, the electrons are weakly driven by the electric field of the light to oscillate at its frequency. The oscillating electrons emit an electric field like that of a classical dipole oscillator. The spectrum consists of a single δ peak at the driving laser frequency (Rayleigh scattering)

$$S(\omega) \propto \left(\frac{\Omega}{\Gamma}\right)^2 \delta(\omega - \omega_l). \tag{3.45}$$

The photon scattering rate is proportional to the laser intensity.
In the strong field limit, i.e. $\Omega \gg \Gamma/4$, the atomic levels are dressed by the light field as shown in Fig. 3.8. There exist four possible decay paths for the atom. Two of these

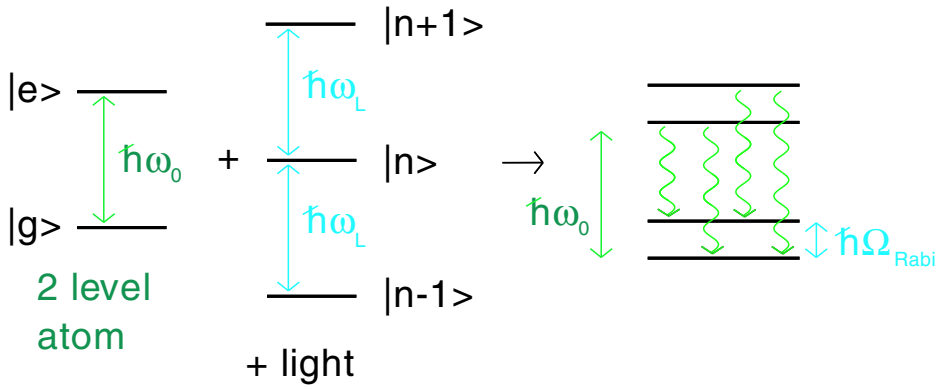

Figure 3.8: Dressed states of two level atom.

paths are degenerate. The spectrum consists of three peaks (Mollow triplet).

$$S(\omega) \propto \left[\frac{3\Gamma/4}{(-\omega-\omega_l-\Omega)^2+(3\Gamma/4)^2} + \right. \tag{3.46}$$

$$\frac{\Gamma}{(\omega-\omega_l)^2+(\Gamma/2)^2} + \tag{3.47}$$

$$\left.\frac{3\Gamma/4}{(-\omega-\omega_l+\Omega)^2+(3\Gamma/4)^2}\right]. \tag{3.48}$$

The strength of the central peak, i.e. the area under the peak, is twice the stength of the sidebands.

The results obtained in the case of a two level system still hold qualitatively in a multi-level system. In a Λ-system one can expect two δ-peaks at the frequencies of the two driving lasers in the low field limit. In the strong field limit, one has two add up all the possible decay paths, leading to a multi-peak spectrum. Calculated spectra for the Λ-system are shown in Fig. 3.9. The laser parameters are set to the same values as in Fig. 3.6.

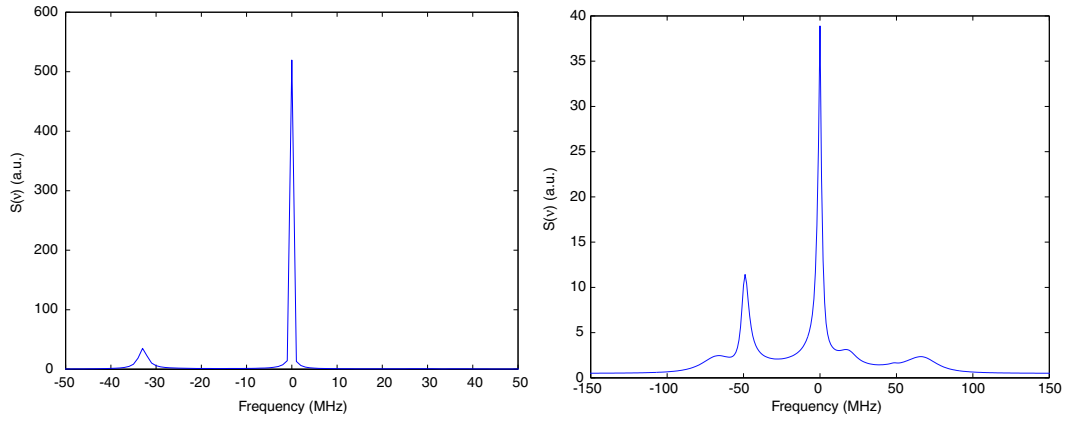

(a) (b)

Figure 3.9: Spectrum of the resonance fluorescence with $\Omega_{32}/\Gamma_{32} = 1$, $\Delta_{12}/2\pi = -5$ MHz, $\Delta_{32}/2\pi = 0$ MHz, (a) $\Omega_{12}/\Gamma_{12} = 1$, and (b) $\Omega_{12}/\Gamma_{12} = 4$. The laser linewidth has been set to zero. Note the different scales. The width of the Rayleigh peak is limited by the resolution of the Fourier transform.

3.5.2 Spectrum of a trapped ion in the low field limit

The fluorescence spectrum of a trapped atom is modified due to the motion in the trap. A trapped ion in a Paul trap oscillates with the micro-motion frequency Ω_f and the macro-motion frequencies ω_i. This leads to sidebands in the fluorescence spectrum. In the strong field limit, these sidebands are partially concealed due to the spectral width of the peaks which is on the order of the natural linewidth Γ. In the low field limit, the sidebands are well resolved due to the δ-peak nature of the Rayleigh scattering.

The important information gained from measuring the sidebands is their strengths and widths. The sideband width is a direct measure for the damping, i.e. the cooling,

of the oscillation inside the trap.
A detailed analysis of the spectrum of a trapped atom can be found in [27, 28]. The main results can be summarized as follows: The sideband strength depends on the temperature of the ion and on the position of the detector relative to the exciting laser beam [28]. In the following, only a one dimensional oscillation, with frequency ν, of a two-level atom in the Lamb-Dicke regime is considered. Then the spectrum consists of the coherent peak at the laser frequency ω_L and two motional sidebands at $\omega_L \pm \nu$. Fig. 3.10 shows the two-level system combined with the motional states $|n\rangle$. The various cooling and heating transitions, which lead to sideband emission of

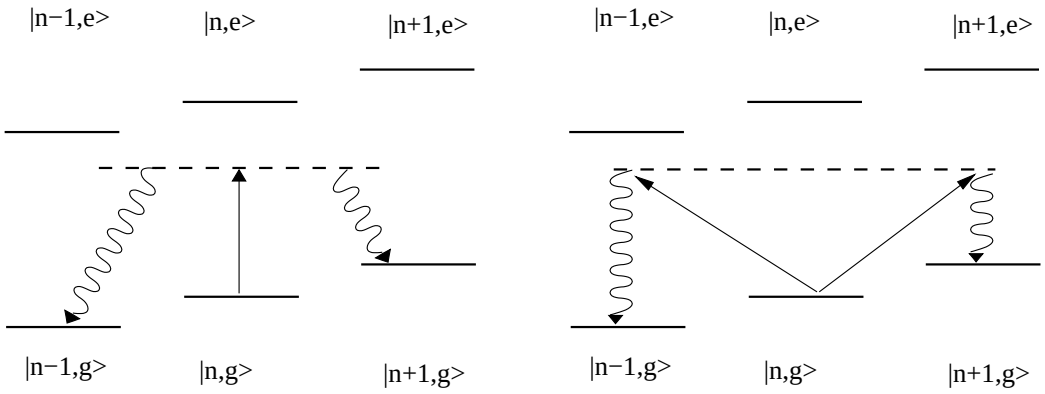

Figure 3.10: Level scheme for a two-level ion trapped in a harmonic potential and interacting with a laser field.

fluorescence, are indicated for low laser intensity. In the Lamb-Dicke regime $\eta << 1$, the cooling or heating transitions with $\Delta n = \pm 1$ are suppressed by a factor $\eta\sqrt{n}$ with respect to the transition with $\Delta n = 0$. The upper sideband is generated by the Raman processes $|n, g\rangle \rightarrow |n-1, g\rangle$, which lowers the motional state n by one. This Raman transition has contributions from two interfering quantum paths $|n, g\rangle \rightarrow |n, e\rangle \rightarrow |n-1, g\rangle$ and $|n, g\rangle \rightarrow |n-1, e\rangle \rightarrow |n-1, g\rangle$. This leads to spatial interference, resulting in the dependence of the sideband strength on the angle $\psi = \angle \vec{k}_{det}\vec{k}_L$ between the detector and the wave vector of the laser beam. The sidebands strength is given by

$$S^U \propto < n > \left| \frac{\cos(\psi)}{\Delta - i\Gamma/2} + \frac{1}{(\Delta + \nu) - i\Gamma/2} \right|^2 . \tag{3.49}$$

The two amplitudes have different energy denominators corresponding to the detuning from the $|n, e\rangle$ and $|n-1, e\rangle$ states. The lower sideband is generated by the transition $|n, g\rangle \rightarrow |n+1, g\rangle$ with a similar strength

$$S^L \propto (< n > +1) \left| \frac{\cos(\psi)}{\Delta - i\Gamma/2} + \frac{1}{(\Delta - \nu) - i\Gamma/2} \right|^2 . \tag{3.50}$$

4 Experimental setup

In this chapter the experimental setup is described. It consists of three building blocks. These are the laser sources, the trap apparatus and the detection setup. Fig.4.1 provides a general overview. The light fields at 493 nm and 650 nm are provided by two diode laser systems. These are optimized to produce narrow linewidth light which is stable in frequency and intensity over several hours. The miniature Paul trap is housed in a vacuum chamber which allows one to excite the ion from three independent directions and to observe it through two channels. The detection system uses these two channels to monitor the ion and analyze its fluorescence. The front channel is used to count the ions fluorescence or to observe the ion with the eye. The back channel uses a lens, which is mounted inside the vacuum chamber, to collect the fluorescence light with a very high beam quality. This light beam is then used for various experiments. A computer with a Labview program[1] controls the frequencies of the lasers and collects the data from the experiment.

4.1 Laser setup

The laser sources have to fulfill certain conditions: In order to use them routinely for spectroscopy, they have to be easy to handle and reliable. Also, their emission wavelength must be tunable to any desired value and remain stable within a few MHz for many hours. Finally, their emission linewidth has to be below 100 kHz to resolve the spectral structures in the Λ-system. In this experiment a diode laser at 986 nm [2], which is frequency doubled to 493 nm, and a diode laser at 650 nm [3] are used to drive the $S_{1/2} - P_{1/2}$ and the $D_{3/2} - P_{1/2}$ transitions, respectively. The laser systems are described in detail in [50, 56–60]. The principle setup of both laser systems is the same. In the following paragraphs first the principles of grating stabilized diode lasers and electronic stabilization are shown, then both lasers are described in detail.

[1] National Instruments
[2] Uniphase L980P180, $P_{max} = 180$ mW
[3] SDL 7511-G1, $P_{max} = 30$ mW

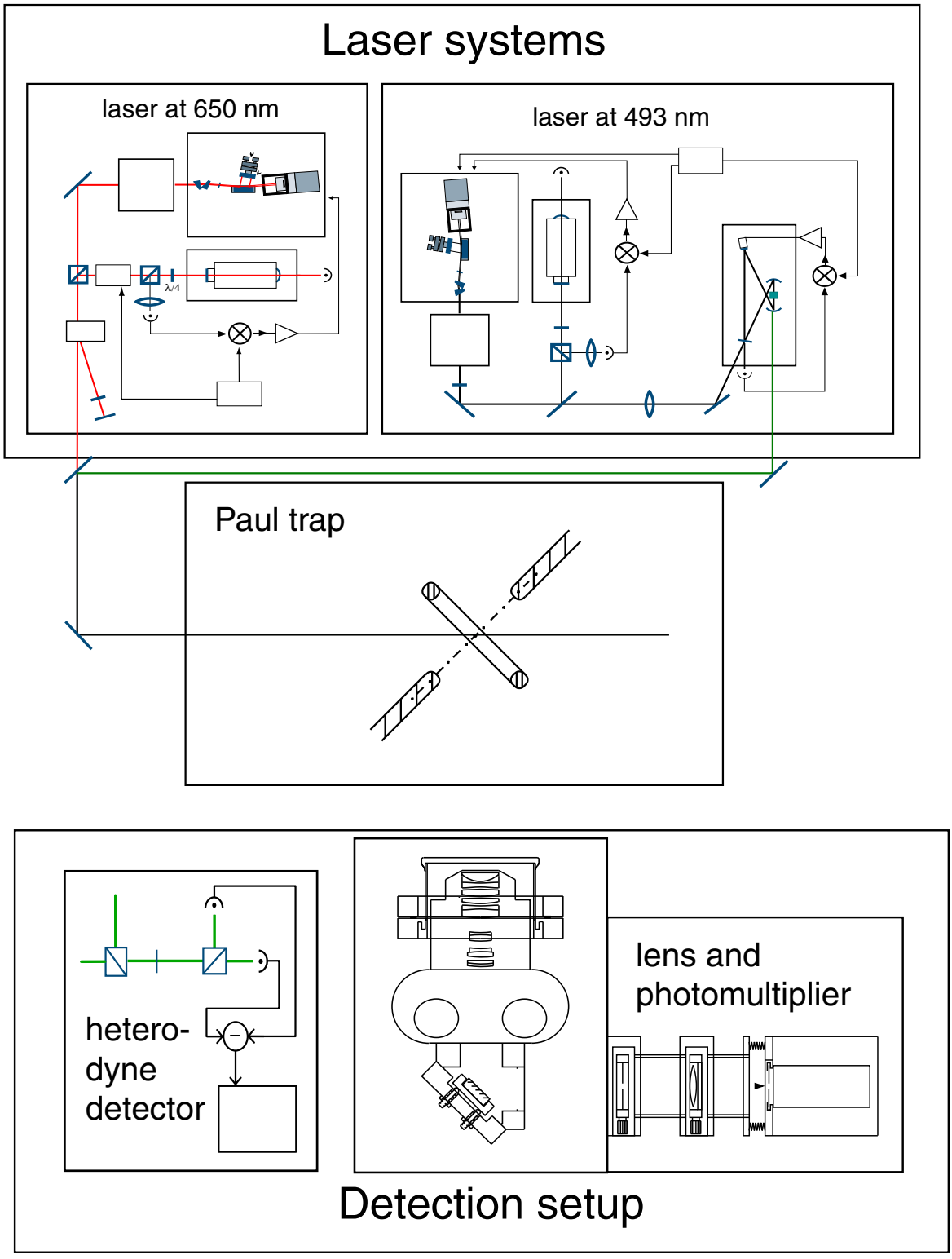

Figure 4.1: Schematic overview of the experimental setup

4.1.1 Littman laser

The inherent large linewidth of laser diodes is on the order of several 10's MHz. Therefore it is necessary for use in precision spectroscopy to reduce the emission bandwidth by a factor of 100 to 1000. This can be achieved with optical feedback from a grating and an additional electronic stabilization to a stable reference resonator. In this experiment a Littman-Metcalf configuration [61] is used, which is shown schematically in Fig. 4.2. The laser diode is mounted in a copper block whose temperature

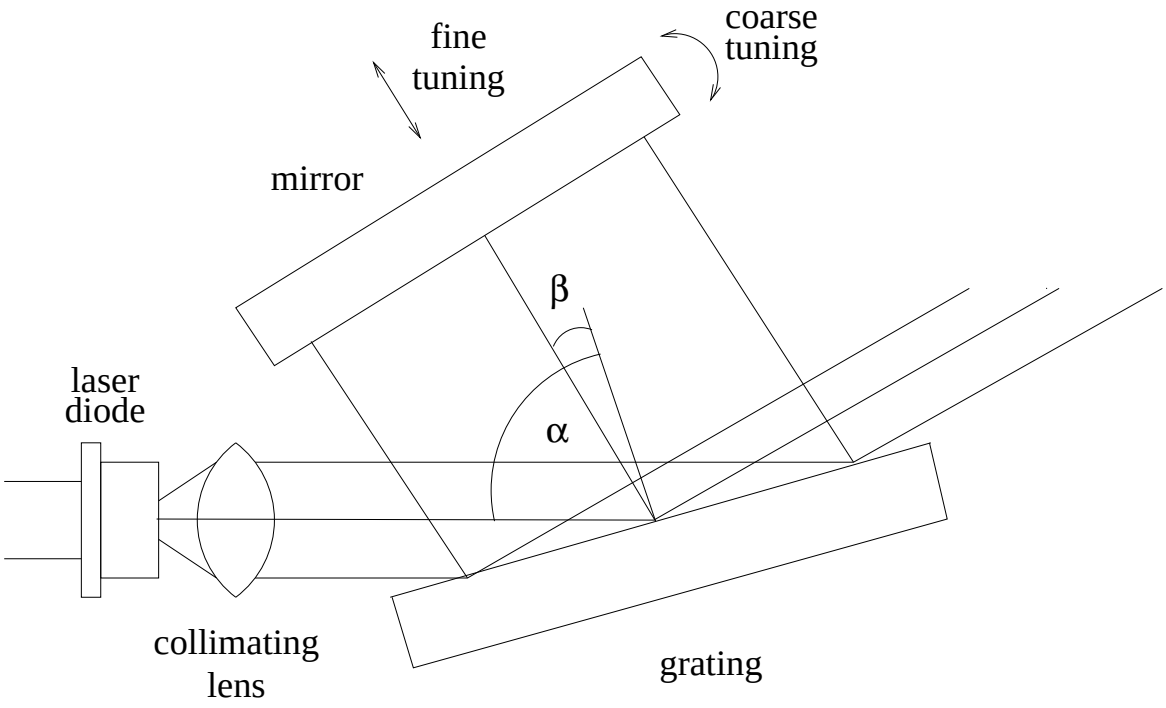

Figure 4.2: Setup of the Littman lasers

is measured with a thermo-electric resistor[4] and controlled with Peltier elements to a temperature slightly above room temperature with 5 mK uncertainty. The emitted light is collimated with a triplet lens[5] and illuminates a grating[6]. The light diffracted by the grating into the 1^{st} order is back-reflected from a mirror[7] into the laser diode, such that the rear facet of the laser diode and the mirror are forming an external laser cavity. The amount of light diffracted into the 1^{st} order, and hence the amount of feedback, depends strongly on the incidence angle. To select a certain wavelength λ,

[4] YSI44203
[5] Schäfter & Kirchhoff SK9648
[6] Zeiss 1800 lines/mm (650 nm) and 1400 lines/mm (986 nm)
[7] Layertech mirrors

the geometry of the setup has to fulfill

$$\lambda = d\ (\sin\alpha + \sin\beta) \tag{4.1}$$

with the grating constant d, angle of incidence α and diffraction angle β. Thus by changing the mirror angle, which varies as β, one can force the laser diode to operate at a desired wavelength. For this purpose, the mirror is mounted on a precision mirror mount[8]. In order to fine-tune the diode laser, the length of this external cavity can be changed with a piezo ceramic (PZT)[9] which shifts the mirror normal to its surface. The 0^{th} diffraction order of the grating is used as output coupler of the laser system. The polarization of the 0^{th} diffraction order is rotated by 90° with a $\lambda/2$ plate[10] and circularized spatially with an anamorphic prism pair[11]. The whole laser setup is mounted in a sturdy aluminum box[12] which is temperature stabilized to $20° \pm 0.2°$ C in order to prevent long term drifts of the laser setup. Optical isolators[13] with an isolation ratio of more than 60 dB are used to prevent unwanted feedback from the rest of the experiment into the diode laser.

4.1.2 Electronic stabilization

The linewidth of the diode lasers is further reduced by means of electronic stabilization to a reference resonator. At the same time, the long-term stability of the lasers, i.e. of the laser center frequencies, is greatly improved. Different methods of electronic stabilization are described in [62,63]. In this work the Pound-Drever-Hall [64] approach is used. It uses a frequency-modulation scheme to generate an error signal which is very steep around zero, but has also a wide capture range. The principle of operation is shown in Fig. 4.3. The light from the laser is phase modulated at a frequency $\Omega_{pd} = 20$ MHz, which is much larger than the linewidth of the reference resonator $\Delta\nu \approx 1$ MHz. For small modulation indices m, only 1^{st} order sidebands contribute. The laser beam is coupled into the reference cavity and the light reflected from the resonator is detected with a fast photodiode. If the laser frequency is near the cavity resonance, the sidebands are off resonance and reflected back without phase shift. The phase shift and amplitude of the reflected carrier depend strongly on its exact detuning from the cavity resonance. If it is on resonance, the phase shift of the carrier is also zero. The photodiode detects the sum of the mixing products of the lower sideband with the carrier, and of the carrier with the upper sideband. On resonance, this is zero because the upper and lower sidebands have opposite sign. Off resonance, the reflected

[8] Lees, Radiant Dyes
[9] Ferroperm
[10] Steeg & Reuter
[11] Melles Griot, Lees mount
[12] Rose
[13] Gseanger 980, Isowave

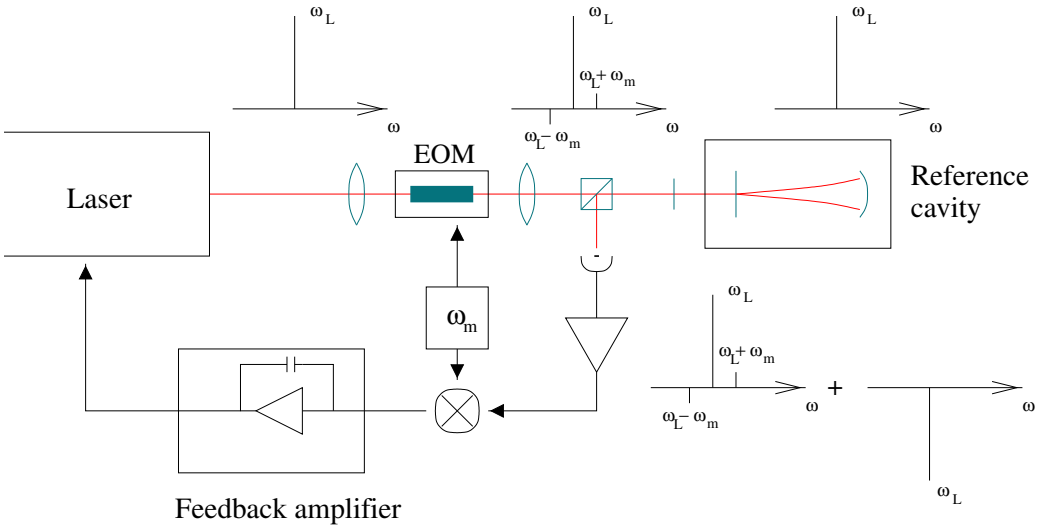

Figure 4.3: The principle of a Pound-Drever-Hall stabilized laser

carrier is phase shifted and the two mixing products do not cancel. A calculation of the error signal can be found in [65]. The photo current is mixed down to DC with a local oscillator with relative phase of 90°. The form of the complete error signal is shown in Fig. 4.4. This signal is amplified with a proportional-integral amplifier and

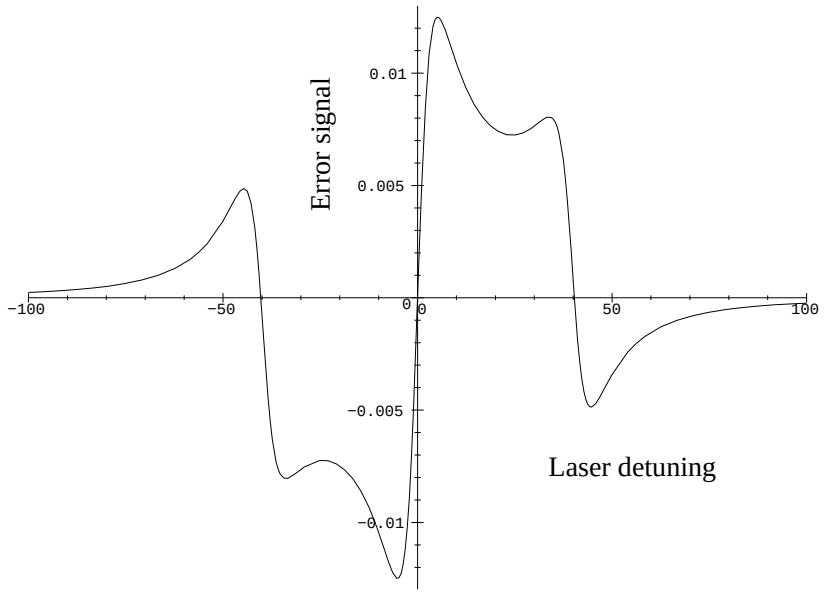

Figure 4.4: Pound-Drever-Hall error signal

fed back onto the laser. The fast part, i.e. up to one MHz, changes the current of the laser diode and the slow part, up to several 100 Hz, controls the PZT voltage of the feedback mirror.

4.1.3 Diode laser at 650 nm

The optical setup of the laser at 650 nm is shown in Fig. 4.5. Due to the very high

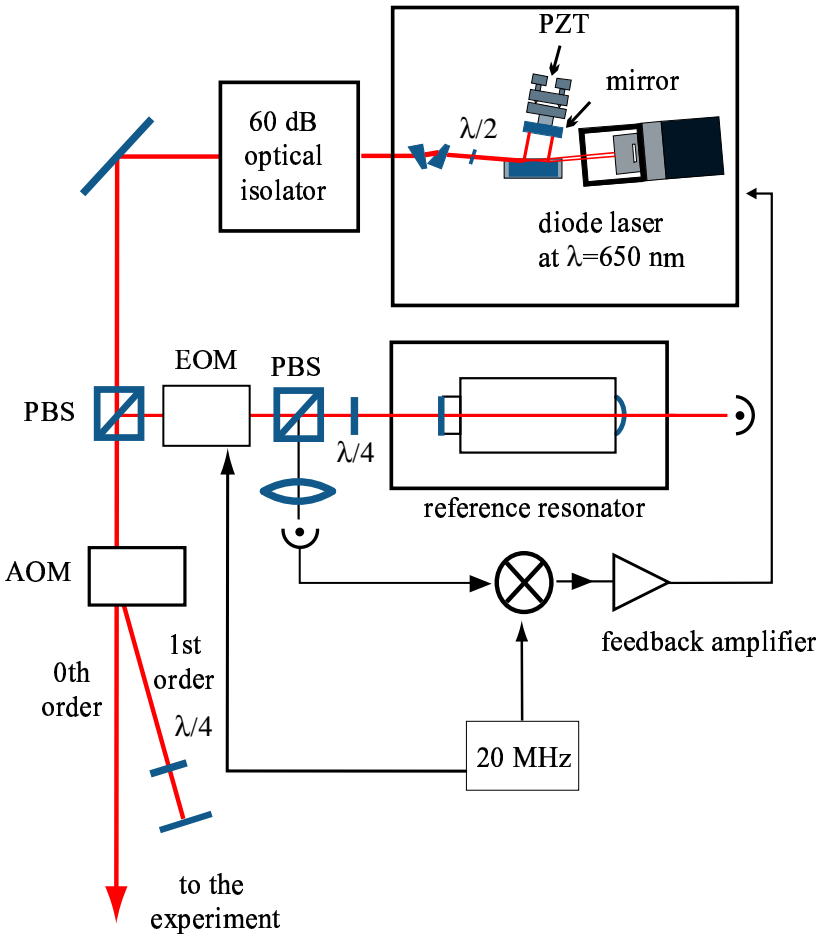

Figure 4.5: Setup of the laser at 650 nm

emission bandwidth of visible light laser diodes, a high level of feedback is required for efficient linewidth narrowing. Therefore the angle of the Littman grating has been chosen such that the feedback into the laser diode is about 30 %. The coarse frequency of the laser is determined with a Michelson-type wave-meter, which has 1 GHz accuracy, and by opto-galvanic spectroscopy in a Ba hollow cathode lamp with

a resolution of about 50 MHz. Then the laser is locked to a fixed reference resonator with a linewidth $\Delta\nu = 750$ kHz and a free-spectral range of $FSR = 750$ MHz, where the mirrors forming the resonator are glued to 20 cm long quartz rod. In order to detune the laser without changing the reference cavity, an acousto-optical modulator (AOM)[14] is inserted between the laser and the reference resonator. This AOM is used in a double-pass arrangement to increase the frequency shift and to get a stable beam position while detuning the AOM. The frequency of the AOM can be tuned from 200 MHz to 300 MHz, so that the light can be detuned in double pass over 200 MHz, which is sufficient for the experiment. The radio-frequency power driving the AOM is controlled in a feedback loop to stabilize the intensity of its zero order, which is used for the experiment. An electro-optical modulator (EOM) produces sidebands at 20 MHz for the Pound-Drever-Hall stabilization. The reference cavity has a finesse of $\mathcal{F} = 1000$ with a free spectral range (FSR) of 750 MHz. The transmitted light is detected with a photodiode to monitor the quality of the stabilization. The reflected light is separated with a polarizing beam splitter and a quarter-wave plate and is detected with a fast photo diode. The photo current is mixed down and fed into a servo amplifier, which controls the laser diode current and the piezo voltage. The resulting linewidth is estimated from the error signal to be on the order of 50 kHz with respect to the reference cavity. Another possibility to determine the laser linewidth is to record excitation spectra of single Ba^+ ions and fit the measured data with eight-level Bloch equations. One of the fit parameters is the combined linewidth of the laser fields. This technique is described in sections 3.2 and 5.4.

The 0^{th} order of the AOM is used for the experiments with trapped Ba^+ ions. A small part of it is split off and used for the wavemeter and the opto-galvanic spectroscopy.

4.1.4 Frequency doubled diode laser at 493 nm

The laser system at 493 nm is described in [60] which is included in Appendix A. Therefore, only important parts of the system and improvements since the publication of ref. [60] are described.

The light at 493 nm is generated by frequency doubling of a diode laser at 986 nm in a setup shown in Fig. 4.6. The setup of the diode laser is the same as the one at 650 nm with a few exceptions. The sidebands used for stabilization are generated by modulating the injection current of the laser diode. The length of the reference cavity can be changed with a PZT, which is mounted between one of the cavity mirrors and the quartz rod. The linewidth estimated from the error signal is below 20 kHz. A beat measurement of two laser systems showed a short term linewidth (≈100 ms) of a few kHz.

[14] Isomet 1250C

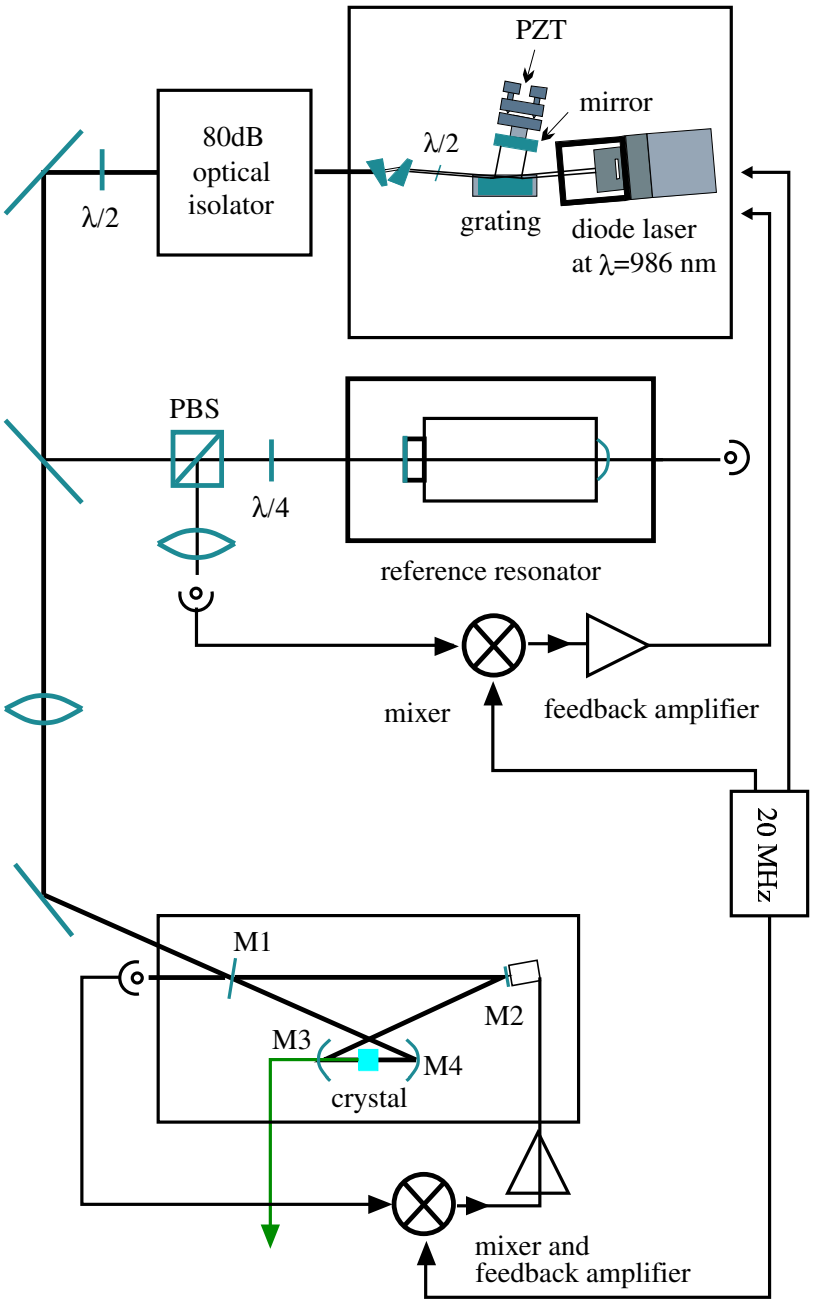

Figure 4.6: Setup of the laser at 493 nm.

The power of the laser system at 986 nm with the diode[15] used in these experiments is 90 mW. It is frequency doubled with a $KNbO_3$ crystal which is placed in an en-

[15]Uniphase L980P180

hancement cavity. This resonator has a FSR of 680 MHz and finesse $\mathcal{F} = 105$. With an enhancement of 33 and an 80% incoupling ratio, the circulating power is 2.38 W. The doubling efficiency of the crystal has been measured [58] to be

$$\eta = \frac{\mathrm{P}_{493\ \mathrm{nm}}}{\mathrm{P}^2_{986\ \mathrm{nm}}} = 1.1 \cdot 10^{-2} \frac{\mathrm{W}}{\mathrm{W}^2}. \tag{4.2}$$

The expected output power at 493 nm is $\mathrm{P}_{493\ \mathrm{nm}} = 62$ mW. This corresponds very well to a measured power of 60 mW.

The long term stability of the reference resonator is not sufficient for the experiment. Therefore, the laser system is locked to a molecular Te_2 transition about 550 MHz away from the Ba^+ $S_{1/2} - P_{1/2}$ transition. The frequency offset is bridged with an AOM[16] with 250 MHz center frequency in a double-pass arrangement and an additional AOM running at 115 MHz. The stabilization to Te_2 has the additional advantage that the laser frequency is reproducible with an accuracy of better than 1 MHz over many weeks.

4.2 Trap apparatus

The trap apparatus consists of the Paul trap [1], the vacuum chamber which houses the trap, and the radio-frequency drive of the trap. The vacuum chamber also holds a high quality lens used to collect the fluorescence light, as will be described in the next section.

4.2.1 Paul trap

A major objective in the trap design was to have access to the ion with laser beams from three different, independent directions and to be able to observe the ion from two directions with a large solid angle. Therefore, an open trap design, as shown in Fig. 4.7, has been chosen. The trap electrodes are made of molybdenum wire with 200 μm diameter. The ring electrode has a diameter of D = 1.4 mm. The end-caps are placed on the symmetry axis of the ring, with 1.4 mm spacing. The rf driving field, with a voltage of up to 1500 V at 18.8 MHz frequency, is applied to the ring electrode. This creates a quadrupole electric field as described in chapter 2. The end-caps are grounded for this ac field but allow to apply a dc offset voltage. The ions are stored at the center of the trap. Due to stray electric fields, and if there is more than one ion trapped, their position is not exactly at the zero of the driving field leading to excess micro-motion. In order to shift an ion into the zero point, a small dc voltage

[16] Brimrose TE270

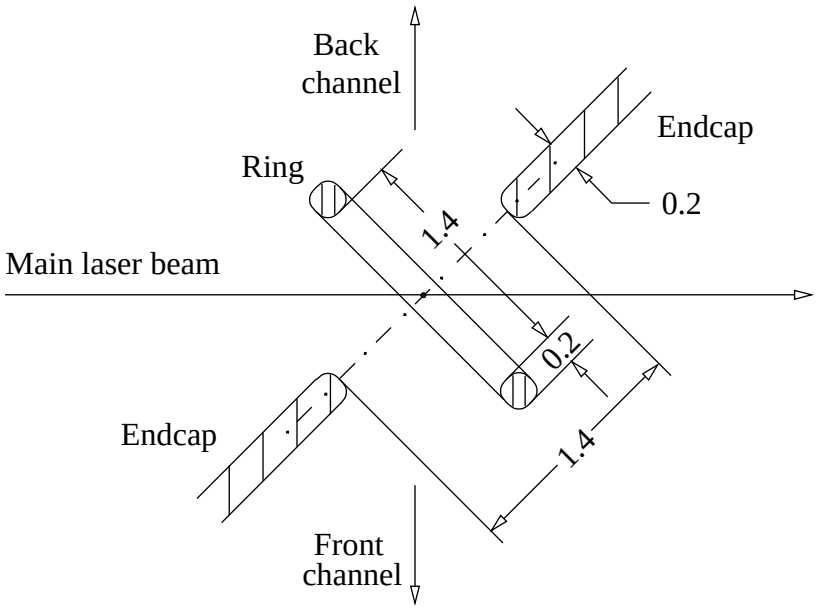

Figure 4.7: Design of the Paul trap and orientation with respect to the two detection channels (view from top).

is applied to one of the end-caps. To allow for compensation in the plane of the ring, there are additional compensation electrodes mounted in that plane with a distance of 5 mm from the ring. All electrodes are attached to steel rods with 1 mm diameter, which are connected directly to vacuum feedthroughs.

To reduce the stray light of the exciting laser beams, a pinhole with a diameter of 600 μm is mounted at a distance of 8 mm in front of the ring on the main laser axis.

4.2.2 Vacuum vessel

The Paul trap is mounted in a vacuum chamber, shown in Fig. 4.8. The spherical vessel provides optical access for observation in two directions and access for laser beams in three independent directions. An atomic oven constructed from a steel pipe with 2 mm diameter and 0.2 mm wall thickness, filled with Barium, is mounted in the vessel with the atomic beam directed through the trap. On the opposite side of the trap an electron gun provides a 400 V electron beam to ionize the Barium atoms. Vacuum at a pressure below 10^{-10} mbar is sustained with a 20 l ion getter pump[17] in combination with a titanium sublimation pump[18].

[17] Varian Vacion Plus 20
[18] Caburn

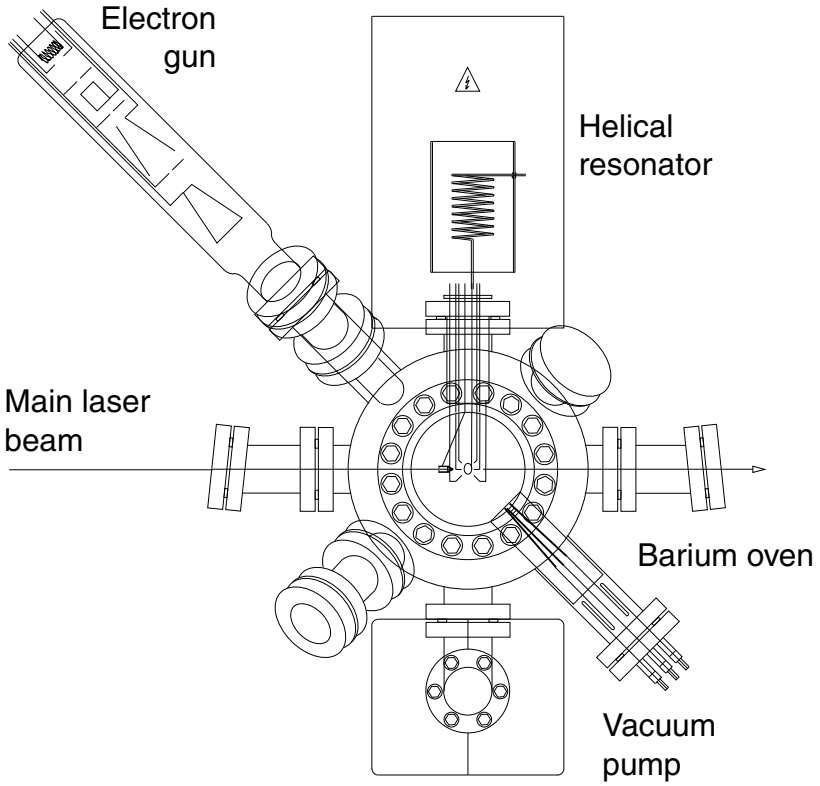

Figure 4.8: The vacuum chamber

4.3 Detection setup

Fluorescence light from the trapped ion or ions is observed from two directions, the front channel and the back channel. While the front channel is mainly used to monitor the ion with the eye or with a photo-multiplier, the back channel is equipped with a high quality lens system to collect the fluorescence light from a large solid angle with a very good beam quality.

4.3.1 The front channel

In the front channel the fluorescence light of the ion is collected through a large viewport[19] with a macroscope[20] ($F_{\#} = 2$). The light can be observed either with the eye, through oculars, or with a photo-multiplier[21] and a photon counting system. The

[19]Larson VPN-400-T
[20]Wild Modell M400
[21]Burle C31034

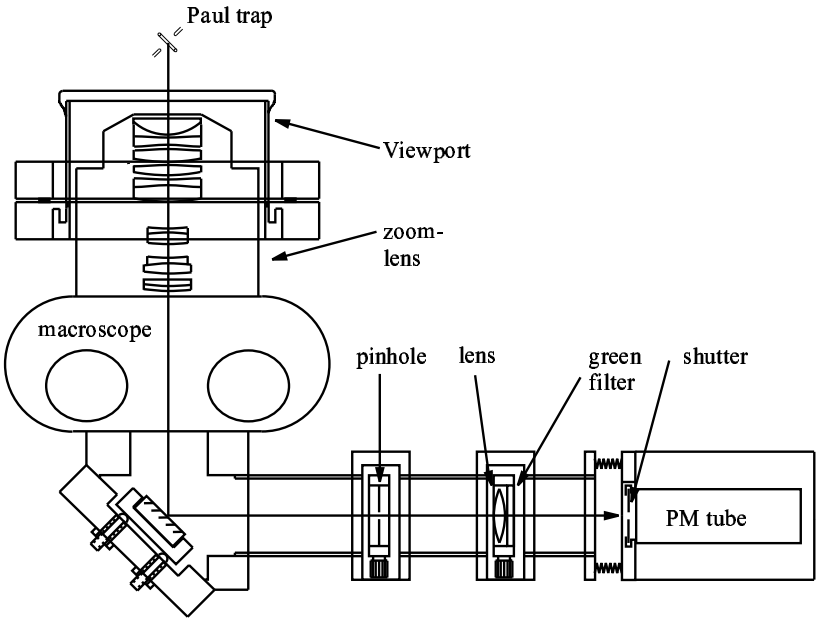

Figure 4.9: Setup of front observation channel

light to the photo-multiplier is spatially filtered by imaging it onto a 600 μm pinhole, to remove stray light, and spectrally filtered with a color filter[22] to block the light at 650 nm. The pulses of the photon counting system are discriminated and counted with a camac system[23] which is read out by the controlling computer.

4.3.2 High quality lens

For interferometric experiments with the fluorescence light it is important to image the fluorescence with high optical quality, i.e. low wavefront distortion or other aberrations. At the same time it is desirable to collect light from a large solid angle. In this experiment a custom-made lens[24] was chosen with a numerical aperture of 0.4 and very low wavefront distortion. Fig. 4.10 shows the lens system and the beam path schematically. The lens is built into the vacuum chamber and the ion is imaged to infinity to prevent additional aberrations due to the vacuum window. The quality of the wavefront was calculated to be better than $\lambda/50$ peak-to-valley for a perfectly made lens. Due to imperfection in the production process the actual quality is slightly lower, but measured to be better than $\lambda/10$ at 493 nm with a Zeigo interferometer [66] by the producer. The lens was then build into the vacuum system and baked out up

[22] L.O.T. BG40
[23] Kinetic systems 3615, 3655
[24] Linos Halo 25/0.4

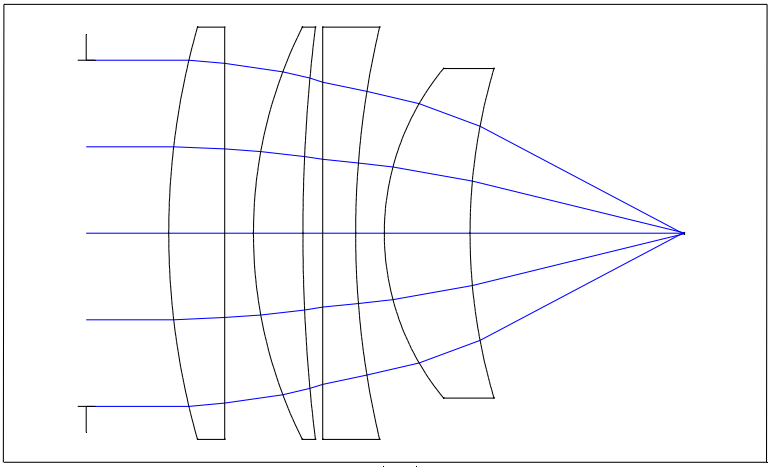

Figure 4.10: Schematic setup of the lens system Halo 25/0.4

to 200° C. The quality after the bake-out has been shown with self interference of the ion (see chapter 7) to be still on the order of $\lambda/10$.

The collection efficiency of the back channel is four times larger than that of the front channel because of the larger numerical aperture and the better anti-reflection coatings. Fig. 4.11 and Fig. 4.12 show an excitation spectrum of an Ba^+ ion simultaneously recorded through the front channel and through the back channel, respectively. The count rate of the two spectra differ by a factor of 4. The absolute collection and detection efficiency of both channels can be calculated from the fits to the excitation spectra. The measurement time for one data point was $\tau = 0.2\ s$. The parameter called 'factor' is the relation between the counted photon rate and the population in the $P_{1/2}$ state divided by 1000. If all photons could be collected, this factor is the spontaneous emission rate times the measurement time $\Gamma \cdot \tau/1000$. The total detection efficiency of the front channel is $\eta = 0.1\%$ and of the back channel is $\eta = 0.4\%$. Taking the quantum efficiency of the photo multipliers of $\eta_{493\ nm} = 25\%$ into account, these numbers are a factor of 2.5 smaller than expected for the solid angle of the lenses. Some of the fluorescence light is absorbed and reflected by the optics, but this is not enough to explain a factor of 2.5.

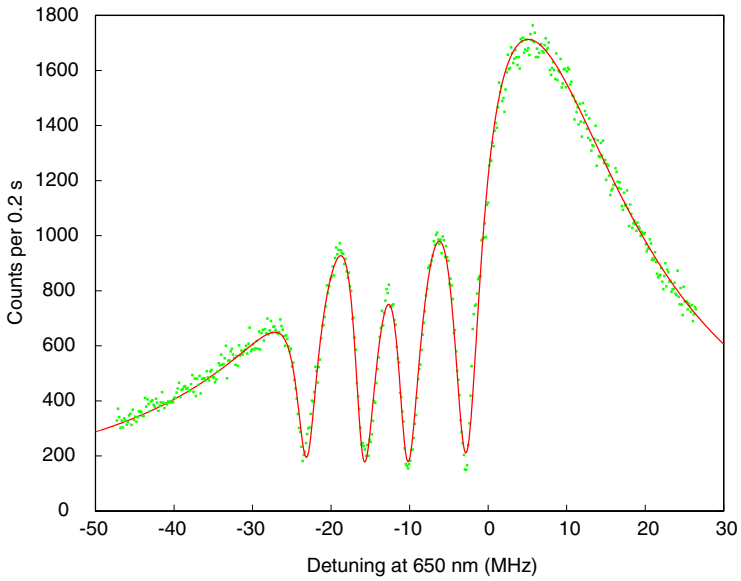

Figure 4.11: Excitation spectrum recorded through the front channel. The fit parameters are $\Delta_g = -12.98$MHz, $S_g = 0.74$, $S_r = 1.68$, $\Gamma_L = 58$ kHz, $u = 4.61$MHz $\alpha = 90°$, factor $= 18.44$ and offset $= 36.60$. The parameters are explained in section (5.4).

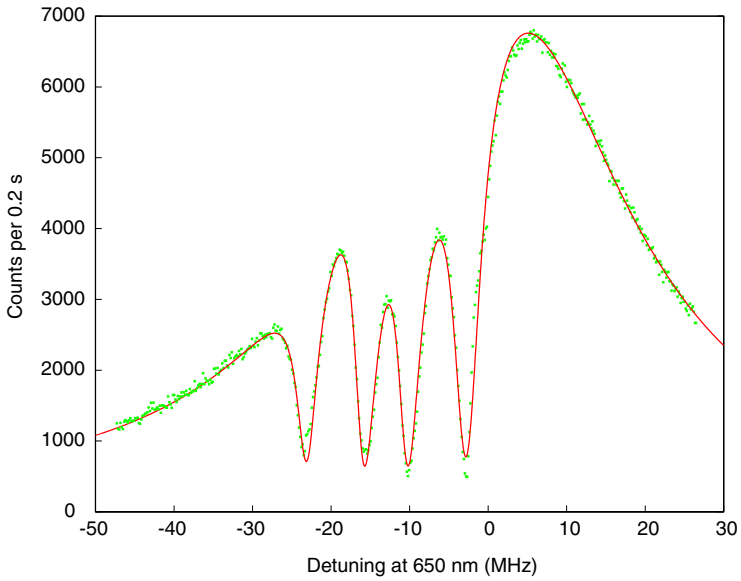

Figure 4.12: Excitation spectrum recorded through the back channel. The parameters are the same as in 4.11 except factor $= 73.49$ and offset $= 79.10$.

5 Preparation of single Ba^+ ions

This chapter describes the steps necessary to prepare the experimental system for the interference experiments. First, the process of generating a single Ba^+ ion, or a pair of ions, is explained. Then the reduction of excess micromotion and the measurement of the trap macromotion frequencies are described. Finally, the experimental parameters, such as the laser detuning and intensity, linewidth of the lasers and magnetic field, are determined by measuring excitation spectra and photon-photon correlation functions.

5.1 Trapping of single Ba^+ ions

In this section, the process of trapping single Ba^+ ions is described. First, the laser parameters have to be set to the optimum trapping conditions. The laser wavelengths are adjusted with the help of a wavemeter with ≈1 GHz accuracy and optogalvanic spectroscopy with ≈50 MHz accuracy. The relative frequency of the laser at 493 nm to the Ba^+ $S_{1/2} - P_{1/2}$ transition can be determined by means of Te_2 spectroscopy, described in chapter 4 and appendix A, with an accuracy of better than 1 MHz. The laser at 493 nm for the $S_{1/2} - P_{1/2}$ transition is red detuned and the laser at 650 nm for the $D_{3/2} - P_{1/2}$ transition is held near resonance.

If it turns out to be necessary to realign the laser beams through the trap center, a big cloud of ions is trapped first, because a cloud is much easier to find with the laser beams than single ions. To do this, an atomic beam of Barium is generated by heating the oven with a current of approximately 4.5 A. This beam can be ionized with an electron beam. If the ionization process takes place inside the trap volume, the ions will be trapped. For large clouds it is helpful to turn off the vacuum pump in order to cool the ions by collisions with the background gas. After the laser beams are aligned the vacuum pump is turned back on and the cloud is removed by shortly turning off the rf driving field.

In order to trap single or few Ba^+ ions the power of the driving field is set to 200 mW which corresponds to a trap frequency of about 200 kHz. The laser at 493 nm is tuned to $\Delta_{493} = -200$ MHz with a power of $P_{493} = 200$ μW and the laser at 650 nm is held near resonance with $P_{650} = 100$ μW. The laser beams have a diameter of 2 mm and 3 mm respectively, and are focused into the trap with an f=250 mm lens. Then the oven is heated with 4 A. When the pressure in the trap reaches about $1 * 10^{-8}$ mbar,

the electron gun is briefly turned on. If an ion is trapped, it is cooled by laser cooling and the fluorescence level rises by about 1000 counts/s after a couple of seconds. If no ion is trapped, the electron gun is pulsed again.
It is possible to load several ions with this method. In some cases more than one ion is loaded at once, or unwanted species are trapped. In this case the fluorescence level is very unsteady and one has to remove the ions by turning off the driving field. The number of Ba^+ ions can be checked by inducing quantum jumps with light from a Ba hollow cathode lamp [56].
After the desired number of ions is loaded, the oven and the filament of the electron gun are turned off and the driving field power is set to 2-5 W. After the oven has been turned off, the pressure drops then from several 10^{-8} mbar to below $1 * 10^{-10}$ mbar within a few minutes.

5.2 Minimizing the micromotion

After a single ion is trapped, it is usually displaced from the ac center of the trap, i.e. the zero of the driving quadrupole field, due to stray electric fields which have been produced by the loading process. In this case the driving field forces the ion to move at the driving frequency with an amplitude which increases linearly with its displacement from the trap center, see section 2.2. This motion leads to unwanted Doppler broadening of the transitions of the ion. Therefore it is necessary to minimize the micromotion by shifting the particle into the zero of the driving field. The position of the ion can be changed by applying dc voltages to one of the end-caps and to correction electrodes which are placed in the plane of the ring.

The amount of micromotion can be measured in three different ways in this apparatus. The most simple way is to observe the position of the ion while the trap stiffness (power of the rf field) is changed. This can be done with the eye or by using a camera. The ion moves towards the ac center of the trap when the stiffness of the trap is increased. Then one decreases the trap stiffness and changes the voltages on the correction electrodes so that the ion is shifted to its position at high trap stiffness. Obviously, this method works only in the 2 dimensional projection which one observes with the eye or camera.
Another method of detecting the micromotion uses a correlation measurement between the arrival time of fluorescence photons and the phase of the driving field [23, 67]. If the laser is detuned to a frequency below the resonance frequency, the ion will absorb and scatter more photons when it is moving towards the laser than when it is moving in the opposite direction. The emission of fluorescence photons is therefore correlated with the micromotion motion in the same way. The correlation is detected using a time-to-digital converter (TDC) and histogram memory[1]. The arrival of a photon

[1] LeCroy Model 4202 and 3588

starts a counter in the TDC. This counter is stopped by the next zero crossing of the driving field. The counter value is proportional to the time delay. Then the bin in the histogram memory, corresponding to the counter value, is increased by one. The histogram memory is read out and reset every second and displayed on the computer. The correlation shows up in the histogram as a modulation at the driving frequency [23]. By moving the ion in the trap one tries to minimize this correlation. Fig. 5.1 shows the correlation of the photon arrivals with the driving field before and after the micromotion has been compensated. This method is only sensitive in the

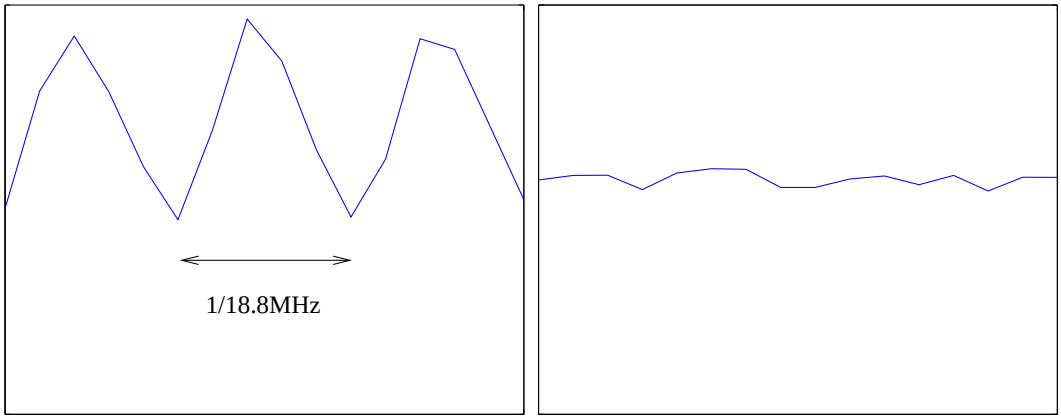

(a) before (b) after

Figure 5.1: Correlation of photon arrival with the driving field phase a) before and b) after compensating the micromotion

direction of the laser beam, i.e. in one dimension. Therefore it is necessary to use three laser beams coming from three independent directions in order to compensate the micromotion in 3 dimensions.

The most sensitive method of minimizing the micromotion is the detection of the sidebands at the driving field frequency in the hetrodyne spectrum of the fluorescence light, see chapter 6. This method is sensitive, with a signal-to-noise ratio of 40 dB on the carrier, to about 1 nm displacement from the trap center. The disadvantage of this measurement is that one has to realign the heterodyne setup every time one moves the ion in the trap.

5.3 Measuring the macromotion frequencies

The driving electric field generates a pseudo-potential for the ion, in which the ion moves with the macromotion frequency, see chapter 2. The frequency of this motion depends linearly on the amplitude of the driving field and it is different in the three spatial directions due to the geometry of the trap. The motion of the ion along the axis of the endcaps is approximately twice as fast as the motion in the plane of the ring. The two modes in the ring plane have slightly different frequencies due to small aberrations of the trap ring from a perfect circle. A method for measuring the macromotion frequencies is to apply a small rf field close to the frequency of the macromotion to one of the trap electrodes and observe the heating of the ion. The frequency of this field is swept over a band of several 10's kilohertz and one observes a dip in the fluorescence level of the ion when the macro motion frequency is hit. Fig. 5.2 shows the decrease of fluorescence at the x and y macromotion frequencies. The frequency resolution of the method is limited to about 1 kHz, because the excited motion has to be large in order to be detected on the fluorescence light. It is also possible to observe

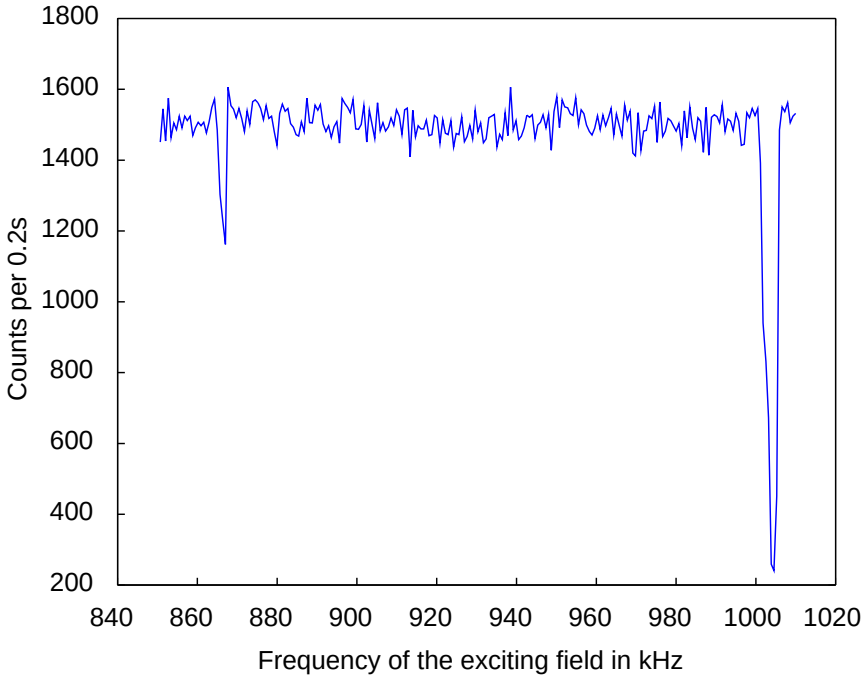

Figure 5.2: Measurement of the x and y macromotion frequencies at a driving power of P=4 W. The frequencies are $\omega_x = 868$ kHz and $\omega_y = 1004$ kHz

the extension of the ion in the direction of the macromotion at resonance with the eye or with a CCD camera, as shown in Fig. 5.3. With this method the principal axis of

the trap can also be determined. A much more sensitive method is the detection of the

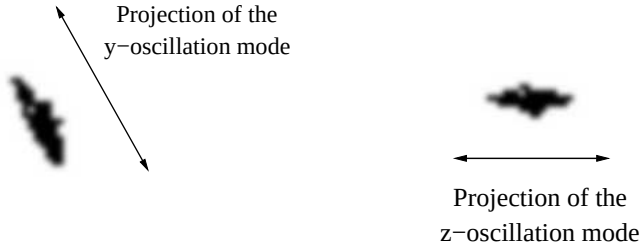

Figure 5.3: Picture of a single ion driven at a) the y-macromotion frequency b) the z-macromotion frequency.

macromotional sidebands in the spectrum of the resoance fluorescence, see chapters 3 and 6.

5.4 Excitation spectra

A measurement of the fluorescence level as a function of the laser detuning is called an excitation spectrum [68]. In such a measurement the fluorescence light is spectrally integrated and its intensity is measured with photo-multipliers. The excitation spectrum can be theoretically described with the stationary solution for the population of the $P_{1/2}$ level of 8-level Bloch equations. By fitting such a solution to the experimental data, several experimental parameters can be determined. These are the laser saturation parameters S_g and S_r, which are given by the ratio of Rabi frequency to the natural linewidth $\Omega/Gamma$, the laser detunings Δ_g and Δ_r , a combined linewidth of both lasers Γ_l, the magnetic field u, the angle between the polarization of the light and the magnetic field α, an offset due to stray light and a factor for the detection efficiency.

To record an excitation spectrum, one laser frequency is set to a certain fixed detuning, usually the laser at 493 nm is red-detuned to maintain cooling, and the other laser is swept over the resonance. Such an excitation spectrum is shown in Fig. 5.4. With the knowledge of the laser parameters from the fit to an excitation spectrum, it is possible

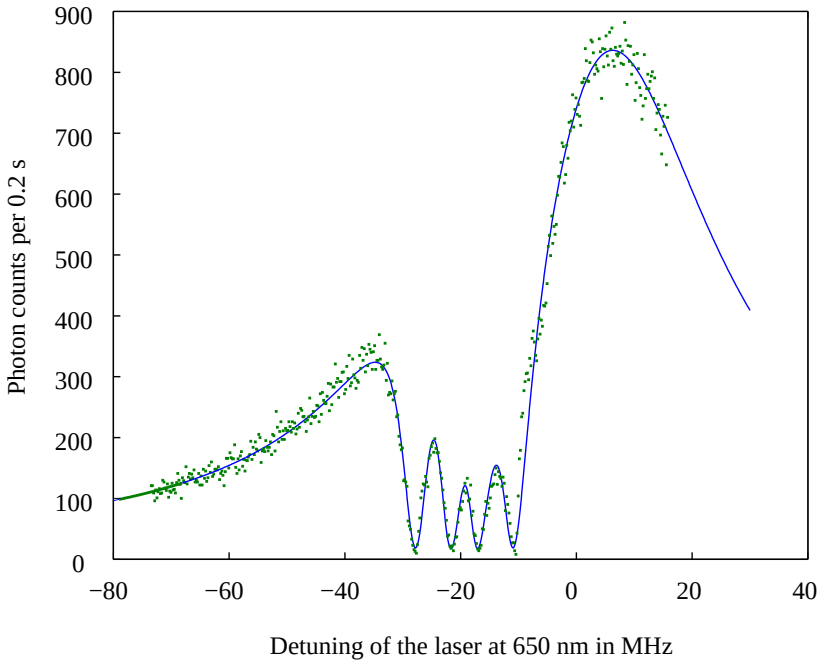

Figure 5.4: Excitation spectrum and fit. The fit parameters are S_g=1.42, S_r=3.02, $\Delta_g = -19.37$ MHz, $\Gamma_l = 4.25$ kHz, u = 3.83 and $\alpha = 90°$

to control and optimize these parameters for the experiments described in the next chapter.

5.5 Intensity correlation measurement

The intensity correlation function $g^2(\tau)$ of the resonance fluorescence, i.e. the correlation of arrival times of fluorescence photons from a single Ba^+ ion (see chapter 3) can be measured with a start-stop measurement of the detected photons. The measurement is done with a TDC, which is started by one detected photon and stopped by the next detected photon. The TDC has a resolution of 156 ps, much shorter than the lifetime of the $P_{1/2}$ state. Due to the dead time of the photo-multiplier, on the order of several ns after the detection of a photon, it is necessary to use different photo-multipliers to generate the start and stop signals. One can show [51] that the photon detection efficiency does not change the outcome of the measurement. This experiment to measure the intensity correlation function $g^2(\tau)$ is only valid for times τ much smaller than the average time between two photons. $g^2(\tau)$ is defined as the correlation between two arbitrary photons at time t and $t+\tau$ independent of whether other photons are detected in the interval between t and $t+\tau$. In this measurement,

the next detected photon is always used to stop the measurement.

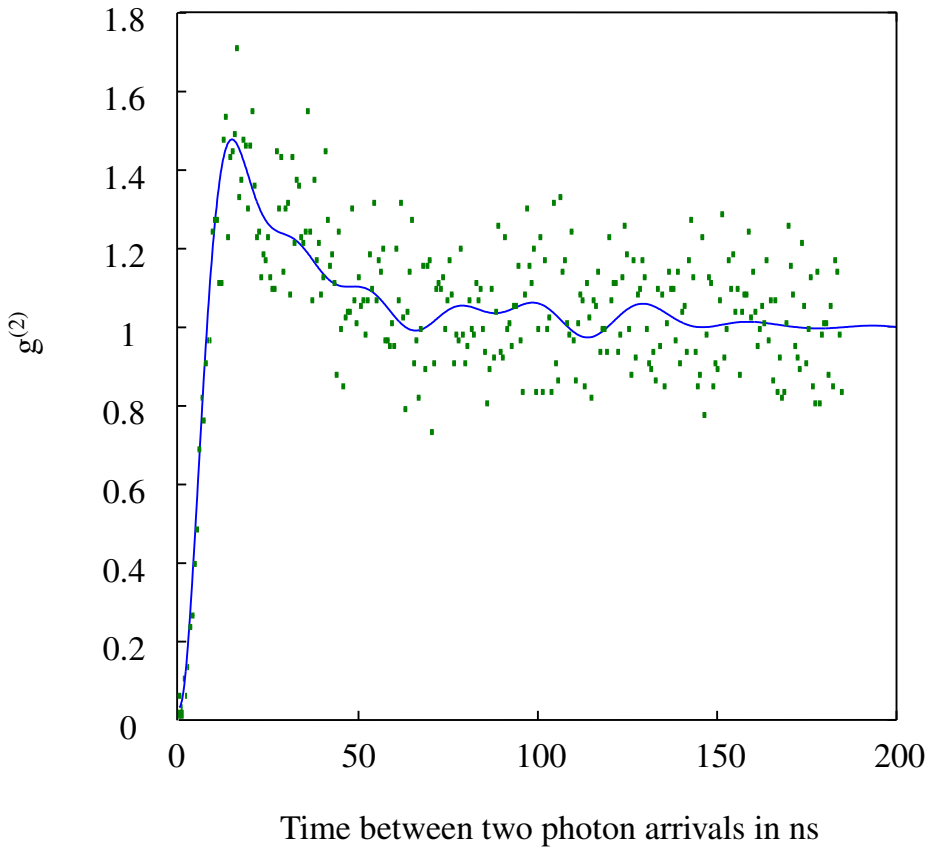

Figure 5.5: Measured $g^{(2)}$ correlation function for a single Ba^+ ion. The theoretical line is a fit to the detuning of the red laser Δ_r only, the other parameters were determined from the excitation spectrum in Fig. 5.4. The red laser detuning is $\Delta_r = 6.61$ MHz.

A measured $g^{(2)}$ function and the fit to 8-level Bloch equations is shown in Fig. 5.5. Most of the parameters have been deduced from an excitation spectrum recorded before. The only free parameters are the red laser detuning, a factor and an offset.

6 Spectrum of the resonance fluorescence

This chapter describes the spectrally resolved measurement of the coherent part of the resonance fluorescence. The coherently scattered light of an atom at rest consists only of a single spectral component at the driving laser frequency. An ion stored in a Paul trap is not at rest but moving with the frequency of the driving field ω_{micro} and with the macro-motion frequencies ω_{macro}. Therefore, sidebands appear in the fluorescence spectrum at these frequencies, as shown in Fig. 6.1. From a measurement of the

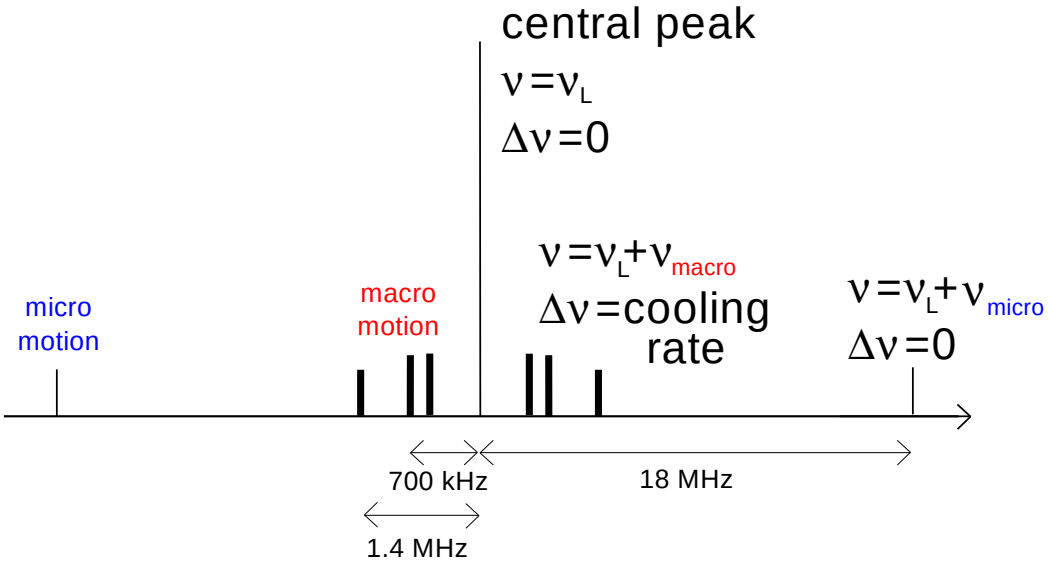

Figure 6.1: Motional sidebands in the spectrum of resonance fluorescence. The central peak is the coherently scattered light, the same as for an atom at rest. Its frequency is the laser frequency, its width $\Delta\nu$ relative to the exciting laser is zero. The macro and micro-motion of the trapped ion lead to sidebands which are displayed schematically. The widths $\Delta\nu$ of the micro-motion sidebands are zero, the width of the macro-motion sidebands is determined by the rate of optical cooling. Higher order sidebands are not displayed.

strengths and the widths of the motional sidebands, one can calculate the amplitude and the damping of the corresponding oscillation mode.

In the following, first the heterodyne setup is described. Then the experimental results are presented which were obtained with the two different lens systems used to collimate the fluorescence light, the Zeiss Kollimator 100 and the Linos Halo 25/0.4.

6.1 Spectrally resolved detection of fluorescence light

In order to resolve the spectral components of the fluorescence light, it is necessary to introduce a tunable narrow band filter into the detection channel. The frequency of this filter is then scanned and the fluorescence intensity is recorded versus the filter frequency.

This filter can be a Fabry-Perot interferometer placed in front of the photo-multiplier. A Fabry-Perot has the advantage that it does not introduce additional noise, but its resolution is limited to several 100 kHz or several MHz. It is suitable to record broad features in the fluorescence spectrum like the Mollow triplet [24, 69]. Narrow spectral features like, e.g., closely spaced sidebands or the coherent scattering peak, cannot be resolved with a Fabry-Perot interferometer, neither can the correlation of the scattered light with the exciting laser be determined.

Here, in order to resolve the narrow Rayleigh scattering and its motional sidebands, a heterodyne detection scheme was chosen. A simple heterodyne detector is shown in Fig. 6.2. The fluorescence light $E_{fl}(t)$ is superimposed on a beam splitter with a

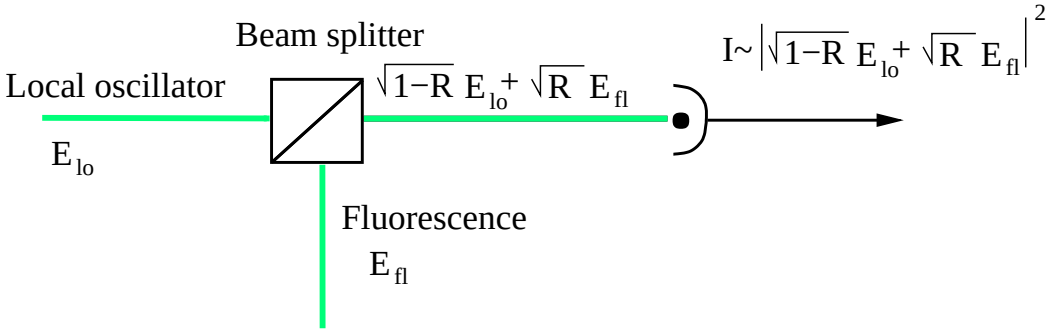

Figure 6.2: Setup of a simple heterodyne detection scheme

reflectivity of R, $0 < R < 1$, with a local oscillator $E_{lo}(t) = E_{lo} \exp^{-i\omega_{lo}t}$, which has a frequency offset relative to the signal field. The frequency offset is chosen that the signal at the difference frequency is not disturbed by the technical $1/f$ noise but can still be detected with photodiodes. A good value is on the order of several 10's MHz. The superimposed light $E_{tot}(t) = \sqrt{R} \cdot E_{fl}(t) + \sqrt{1-R} \cdot E_{lo}(t)$ produces a photo current on the detector, which has a contribution at this offset frequency. The light fields are

assumed to be plane waves within an area A, which is smaller than or equal to the detector size. Their total optical power is then $P_{tot}^{opt} = 2\epsilon_0 cA < E_{tot}(t)^* E(t)_{tot} >$. The power spectrum of the photo current is measured with a spectrum analyzer.

The measured photo current $i(t)$ is proportional to the intensity of the superimposed light fields

$$\begin{aligned} i(t) &= \frac{2e\eta A\epsilon_0 c}{\hbar\omega}|\sqrt{R}\cdot E_{fl}(t) + \sqrt{1-R}\cdot E_{lo}(t)|^2 = \\ &= \kappa\{(1-R)\cdot E_{lo}^* E_{lo} + R\cdot E_{fl}^*(t)E_{fl}(t) + \sqrt{R-R^2}\cdot \mathrm{Re}[E_{fl}^* E_{lo} e^{-i\omega_{lo}t}]\} \end{aligned} \tag{6.1}$$

where η is the quantum efficiency of the detector, and $\kappa = \frac{2e\eta A\epsilon_0 c}{\hbar\omega}$ [70]. The photo currents generated by the fields $E_{fl}(t)$ and E_{lo} alone is $i_{fl}(t) = \kappa R < E_{fl}(t)^* E_{fl}(t) >$ and $i_{lo} = \kappa(1-R)E_{lo}^* E_{lo}$, respectively. The average $< ... >$ is the time average over the terms oscillation with optical frequenencies. The local oscillator is asumed to be an constant, plane wave. Therefore the average over its photo current is constant. The power spectrum of the photo current is

$$P_I(\omega) = \frac{1}{2\pi}\int_{-\infty}^{\infty} C_i^{(1)}(\tau)e^{-i\omega\tau}\mathrm{d}\tau \tag{6.2}$$

with the correlation function $C_i^{(1)}(\tau)$ of the photo current. This is

$$C_i^{(1)}(\tau) =< i(t+\tau)i(t) >=< i(t) >^2 g^{(2)}(\tau) \tag{6.3}$$

with

$$g^{(2)}(\tau) = \frac{< E_{tot}^*(t+\tau)E_{tot}(t+\tau)E_{tot}^*(t)E_{tot}(t) >}{< E_{tot}^*(t)E_{tot}(t) >^2} \tag{6.4}$$

the intensity correlation function of the superimposed light. Equation (6.3) holds for classical signal and local oscillators. The quantization of the light field and the current can be accounted for by adding an extra term [71]. This so called shot-noise term corresponds to that part of the total current at the times t and $t+\tau$ which is associated with a single photo-electron. Let the current of a single photon be $e\delta(t)$. The single electron correlation function is $< e\delta(t+\tau)e\delta(t) >= e^2\delta(\tau)$, and with photo-electrons generated at an average rate of $< i(t) > /e$ the total contribution to $C_i^{(1)}(\tau)$ becomes $e < i(t) > \delta(t)$. The photo-current correlation function becomes

$$C_i^{(1)}(\tau) =< i(t) >^2 g^{(2)}(\tau) + e < i(t) > \delta(\tau). \tag{6.5}$$

This result is identical to that of a rigorous quantum treatment [71]. Eq. (6.5) is expanded in terms of E_{lo} and $E_{fl}(t)$. The fast oscillating terms are averaged out and only the terms containing i_{lo} and i_{lo}^2 are retained:

$$\begin{aligned} C_i^{(1)}(\tau) =& \sqrt{1-R}ei_{lo}\delta(\tau) + (1-R)i_{lo}^2 + \\ & \sqrt{R-R^2}i_{lo} < i_{fl}(t) > [e^{i\omega\tau}g_{fl}^{(1)}(\tau) + e^{-i\omega\tau}g_{fl}^{(1)}(\tau)^*] \end{aligned} \tag{6.6}$$

The spectral density of the photo current measured by a physical spectrum analyzer is

$$P_i^{meas}(\omega) = \sqrt{1-R}\frac{ei_{lo}}{\pi} + (1-R)i_{lo}^2\delta(\omega) + \sqrt{R-R^2}\frac{i_{lo} < i_{fl}(t) >}{\pi} \cdot \int_{-\infty}^{\infty} e^{i\omega_{lo}\tau} g_{fl}^{(1)}(\tau) e^{-i\omega\tau} \mathrm{d}\tau \quad . \tag{6.7}$$

The measured power spectrum density of the photo current contains three terms: The shot-noise $\sqrt{1-R}\frac{ei_{lo}}{\pi}$ gives rise to a constant background in the spectrum (white noise). The dc part $(1-R)i_{lo}^2\delta(\omega)$ is generated by the local oscillator and is zero except at $\omega = 0$. The signal term $\sqrt{R-R^2}\frac{i_{lo} < i_{fl}(t) >}{\pi} \cdot \int_{-\infty}^{\infty} e^{i\omega_{lo}\tau} g_{fl}^{(1)}(\tau) e^{-i\omega\tau} \mathrm{d}\tau$ is an exact replica of the spectrum of the fluorescence light, shifted by the local oscillator frequency. In this description, the electronic noise introduced by the detector (Johnson resistor noise and amplifier noise) is neglected. This is valid if the shot-noise is much larger than the electronic noise of the detector (shot-noise limit). The ratio between signal and shot noise increases for increasing reflectivity R of the beamsplitter. The reflectivity is limited in the experiment because one has to increase the local oscillator power when increasing R to stay in the shot noise limit regime. An additional noise source is amplitude fluctuations of the local oscillator, i.e. if i_{lo} is not constant. Their influence can be greatly reduced by a balanced detection scheme, shown in Fig. 6.3. This scheme also has the additional advantage that the part of the signal which is transmitted through the beam splitter is used. The measured power spectrum density has the same form as (6.7), but without the dc term and no part of the signal is wasted:

$$P_i^{meas}(\omega) = \frac{ei_{lo}}{\pi} + \frac{i_{lo} < i_{fl}(t) >}{\pi} \cdot \int_{-\infty}^{\infty} e^{i\omega_{lo}\tau} g_{fl}^{(1)}(\tau) e^{-i\omega\tau} \mathrm{d}\tau \tag{6.8}$$

6.2 The signal-to-noise ratio in heterodyne detection

Let the total power $P_{fl} = 2i_{lo} < i_{fl}(t) > /\pi$ of the signal be distributed over a spectral bandwidth $\Delta\nu$, so that the spectral power density at the center frequency ω_c is $P_{fl}(\omega_c) = P_{fl}/\Delta\nu$. The ratio between the spectral power density of the signal at the center frequency ω_c and the shot noise power density $P_{shot} = ei_{lo}/\pi$ is

$$\mathrm{SSNR} = \frac{P_{fl}(\omega_c)}{P_{shot}} = \frac{2 < i_{fl}(t) >}{e\Delta\nu} \tag{6.9}$$

and will be called signal-to-shot-noise ratio (SSNR) in the following. The SSNR can also be expressed in terms of the number of signal photons $N = P_{fl}^{opt}/\hbar\omega$,

$$\mathrm{SSNR} = \frac{\eta N}{\Delta\nu}. \tag{6.10}$$

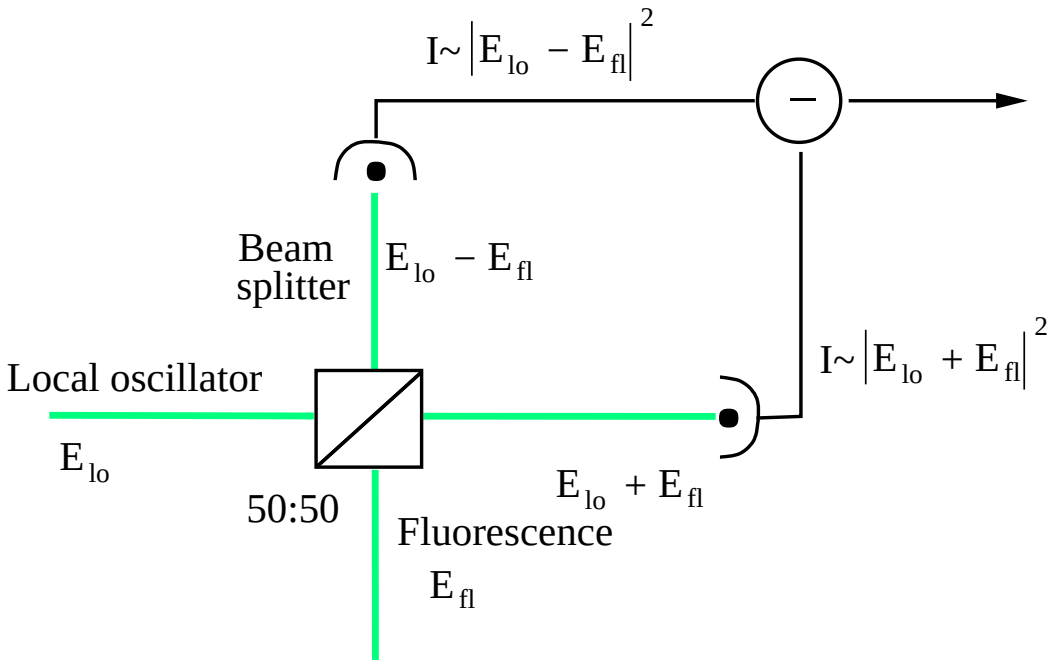

Figure 6.3: Setup of a balanced heterodyne detection scheme

In the derivation of the SSNR, plane, perfectly parallel light fields are assumed, i.e. the overlap between signal and local oscillator beam is perfect. However, this is not the case in the experiment. The wavefronts of the signal and local oscillator can be mismatched due to imperfect parallelity and overlap. Also, their wavefronts can be deformed by optical elements, e.g. the collimation lens. The quantum efficiency of the photodetectors that are used can also vary spatially. This can be taken into account by integrating spatially over the electric fields [72]:

$$\mathrm{SSNR} = \frac{\eta N}{\Delta\nu} \cdot \frac{|\int \eta \vec{E}_{lo}^{*} \vec{E}_{fl} \mathrm{d}A|^2}{\eta^2 \int |\vec{E}_{lo}|^2 \mathrm{d}A \int |\vec{E}_{fl}|^2 \mathrm{d}A} \cdot \frac{\int \eta^2 |\vec{E}_{lo}|^2 \mathrm{d}A}{\int \eta |\vec{E}_{lo}|^2 \mathrm{d}A} \tag{6.11}$$

The achievable SSNR depends very strongly on the relative wavefront error of both fields and on their parallelity. Therefore, these parameters have to be controlled very carefully in the experiment.
The maximum SSNR achievable in this experiment, assuming perfect matching of the beams and wavefronts, can be calculated. The number of coherently scattered photons is calculated from the optical Bloch equations as described in chapter 3. It is the spontaneous emission rate $\Gamma_{SP} = 2\pi \cdot 15.1\ 10^6 s^{-1}$ times the population of the $P_{1/2}$ state, ρ_{22}, times the first order correlation function of the green light for long times, $g^{(1)}(\tau \rightarrow \infty)$. The value of $\rho_{22} \cdot g^{(1)}(\tau \rightarrow \infty)$ is $\leq$0.02 in the case of Ba^+. The maximum number of coherently scattered photons is therefore $N_{sc} = 1.9\ 10^6 s^{-1}$.

Of these photons, 1.6% are collected by the HALO 25/0.4 lens. The total detection efficiency is about $\approx 50\%$, i.e. the photo diodes have quantum efficiency of 80% and other losses are smaller than 40%. With perfectly overlapping wavefronts, the number of collected and detected signal photons is $N = 15000$. These signal photons are spread over the carrier and the sidebands of motion. Assuming an ion in the Lamb-Dicke regime, such that the motional sidebands are much smaller than the carrier, e.g. 50% power in the carrier, a SSNR on the carrier of 7500 (38 dB) in a detection bandwidth of 1 Hz can be expected. On the carrier, the detection bandwidth can be in principle reduced to 0, because the carrier is completely coherent with the exciting laser field and therefore with the local oscillator. The macro-motional sidebands however are broadend by laser cooling. Their width is expected to be in the range of several 100 Hz.

Another measure for the visibility of spectral components in the measurement is the ratio of the signal height to the sum of noise on the signal and shot noise. This measure is called averaged signal-to-noise ratio (ASNR) in the following. The shot noise power density ei_{lo}/π in the power spectrum fluctuates due to the random nature of the photon detection. The noise of the signal is its shot noise, i.e. the square root of the number of signal photons N. This noise can be reduced by averaging over an number M of measured spectra. The ASNR is then

$$\mathrm{ASNR} = \sqrt{M}\frac{\eta N/\Delta\nu}{\sqrt{1+\eta N/\Delta\nu}} = \sqrt{M}\frac{\mathrm{SSNR}}{\sqrt{1+\mathrm{SSNR}}}. \tag{6.12}$$

In the measurement of the motional sidebands the number of averages was set to $M = 1000$, the SSNR was 0.1 in this case, resulting in an $ASNR = 3$. The SSNR is also a measure for the signal-to-noise ratio of the photo current in the time domain. E.g. if one wants to use the heterodyne signal of the macro-motional sidebands to gain information of the ion motion in real time in a bandwidth $\Delta\nu$, that would require a SSNR> 1 in $\Delta\nu$.

6.3 Experimental realization of the balanced heterodyne detector

In the experimental realization the division ratio of the beam splitter is not exactly 1:1 because of uncertainties in the production process. This imbalance leads to a deterioration of the local oscillator noise reduction. Therefore, this beam splitter is replaced by a combination of polarizing beam splitters and a half-wave plate, as shown in Fig. 6.4. The light fields which excite the ion and the local oscillator are generated from the same laser, and are, therefore, coherent. The laser light which excites the ion is frequency-shifted with an acousto-optical modulator (AOM) by 115.86 MHz,

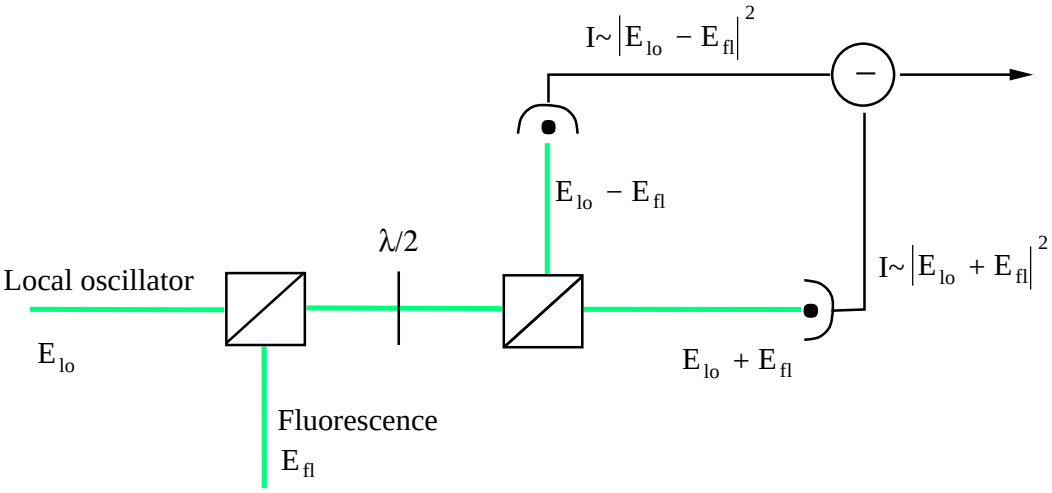

Figure 6.4: Setup of a balanced heterodyne detection scheme using polarizing beam splitters.

the local oscillator is shifted by 85.16 MHz. The heterodyne signal of the carrier is expected at the difference frequency of both AOMs. This frequency is not generated elsewhere in the setup, such that no electrical crosstalk perturbs the final signal, neither can any residual amplitude modulation in one of the beams create a 30.7 MHz signal on the photodiodes. The fluorescence light, after collimation with the lens, is superimposed on a polarizing beam splitter with the local oscillator field. The electric field of the superimposed light is $E(t) = \vec{e}_x E_{fl}(t) + \vec{e}_y E_{lo}(t)$. The polarization of the light is rotated by 45° with a half-wave plate, and the beam is split into two parts E_1 and E_2 on a second polarizing beam splitter.

$$E_1(t) = \vec{e}_x \tfrac{1}{\sqrt{2}}(E_{fl}(t) + E_{lo}(t)) \tag{6.13}$$

$$E_2(t) = \vec{e}_y \tfrac{1}{\sqrt{2}}(E_{fl}(t) - E_{lo}(t)). \tag{6.14}$$

The negative sign in (6.14) is caused by a phase-shift of π through the half wave plate. The half-wave plate is rotated to the best balance, i.e. the best supression of the local oscillator noise. The intensities of the two output fields are detected with two photodiodes resulting in photo currents $I_1(t)$ and $I_2(t)$

$$I_1(t) \propto E_{lo}(t)^2/2 + E_{lo}(t)E_{fl}(t) + E_{fl}(t)^2/2 \tag{6.15}$$

$$I_2(t) \propto E_{lo}(t)^2/2 - E_{lo}(t)E_{fl}(t) + E_{fl}(t)^2/2. \tag{6.16}$$

These photo currents are the same as described in section (6.1). The photo currents are subtracted and converted into a voltage. This signal is mixed down with an additional RF field to about 50 kHz, low pass filtered, and then analyzed using a fast Fourier

transform spectrum analyzer[1] The electronic noise power of the detector is three times smaller than the shot noise power of the local oscillator when 2 mW optical power is used (shot noise limit). All RF sources used in this setup are derived from the same 10 MHz quartz reference oscillator.

6.4 Measurements with the Zeiss Kollimator

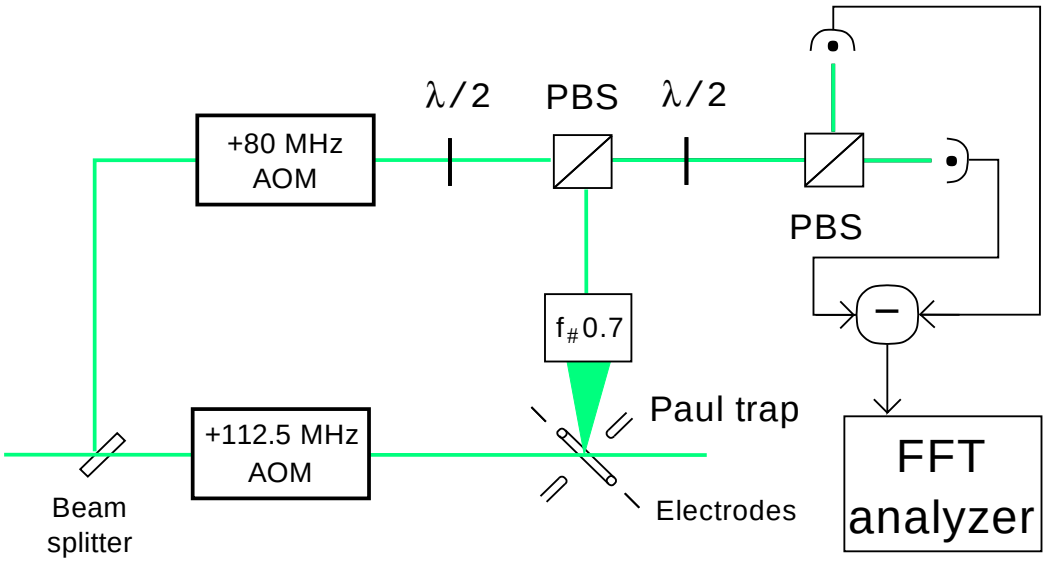

Figure 6.5: Heterodyne experiment with the Zeiss Kollimator.

The experiment was first equipped with a Zeiss Kollimator to collect the fluorescence light. The results of this work are published in [73], which is also reprinted in Appendix B. First, the setup of the detection scheme is described, and measurements of the carrier and the micro-motion sidebands are presented. Finally, the measurement of the cooling rate by probing the macro-motion is shown.

6.4.1 Detection scheme

The setup of the heterodyne detector is shown in Fig 6.5. The light of the ion is collected with a Zeiss Kollimator 100 system. This Zeiss lens has a very high numerical aperture NA=0.7 and collects 15% solid angle. The local oscillator is spatially filtered and mode matched with a telescope. The detection scheme is the one described in

[1] Stanford Research SR770

section (6.3). The expected signal-to-noise ratio should be 3 times higher than the one calculated in section (6.2), because of the larger collection efficiency of the Zeiss lens compared to the HALO 25/0.4.

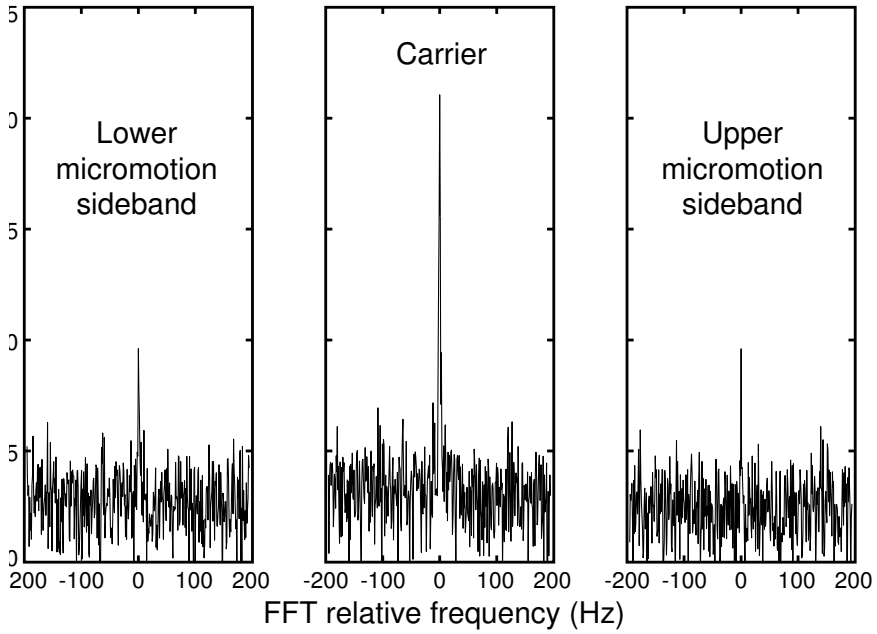

Figure 6.6: Spectrum of the resonance fluorescence of a single ion. The carrier and the two sidebands of micro-motion are shown.

6.4.2 Rayleigh peak and micro-motion sidebands

A typical spectrum of the carrier and sidebands of the micro-motion is shown in Fig. 6.6. Here the resolution of the FFT spectrum analyzer was set to 1 Hz.
The signal-to-shot-noise ratio of the carrier is 50 (17 dB) in this example, about two orders of magnitude smaller than the value expected for perfect overlap of the fluorescence beam with the local oscillator. The reason is the very bad imaging quality of the Zeiss Kollimator. The wavefront distortion of this lens has been calculated with Zemax[2] to be 50 λ.

The δ-like nature of the Rayleigh scattering (the carrier peak in Fig. 6.6) is demonstrated in Fig. 6.7. Here the resolution of the analyzer is set to 61 mHz and the spectrum still consists of only one point. The linewidth of the Rayleigh carrier is theoretically zero, in the experiment it is limited by the mechanical stability of the setup, which forms a Mach-Zehnder interferometer with the ion serving as one mirror.

[2]Focus Software, inc.

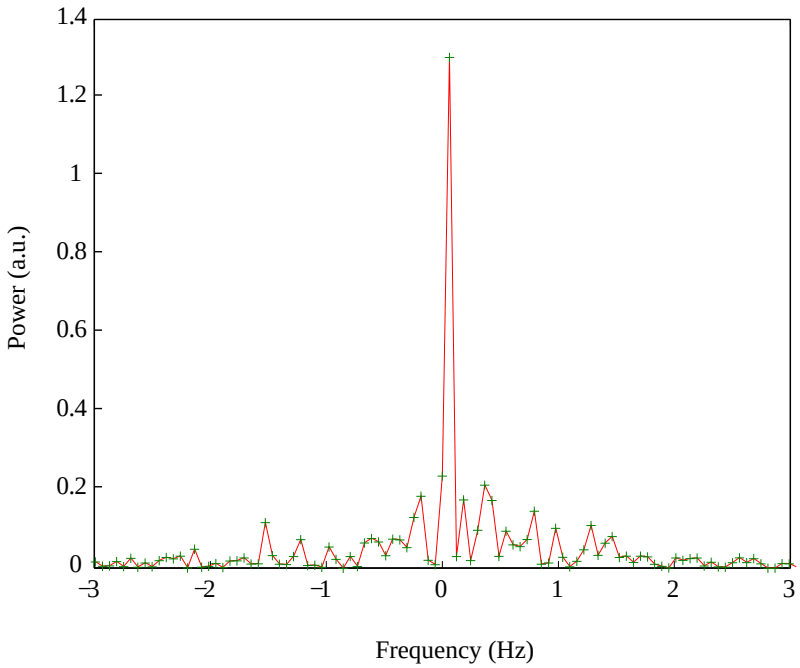

Figure 6.7: The carrier of the Rayleigh scattering with 61 mHz resolution.

6.4.3 Measurement of the cooling rate

Direct measurement of the macro-motion sidebands, i.e. of the freely oscillating ion, with an SSNR=1 requires as many detected photons in that sideband as its width in Hz. The width of the sidebands is expected to be of the order of several 100's Hz. The maximum number of detected signal photons on the carrier is 50. Assuming that the power in the macro-motional sideband is 20% of the carrier, one can expect 10 signal photons on the sideband in a bandwidth of several 100 Hz, resulting in a SSNR of ≈0.02. Averaging over many spectra to achieve an $ASNR > 1$ would take an unreasonably long time, i.e. many 10's of minutes.

Yet there is a possibility to measure the frequency and the damping of the macro-motion by probing it with a weak electrical excitation. The electric field is applied to a trap electrode, the same as for the measurement of the macro-motion frequency in (5.3), but its voltage is smaller by a factor of 100. The ion is excited and oscillates at the frequency of the exciting field with an amplitude that depends on the detuning of the electric excitation from the mechanical resonance of the ion, and on the damping of the oscillation. The important point is that this additional oscillation is coherent with the electric excitation, which itself is in phase with the AOM driving fields. The

amplitude of the driven oscillation at the frequency ω is then

$$x(\omega) = \frac{x_0}{1 + (\frac{\omega - \omega_0}{\Delta\omega})^2} \tag{6.17}$$

with the maximum amplitude x_0 which depends on the driving strength, the resonance frequency ω_0 and the damping $\Delta\omega$, which is equal to the cooling rate. The relative heights of the carrier and the sidebands are given by the Bessel functions $J_n(kx(\omega)$, $n = 0$ for the carrier, $n = 1$ for the sideband, with the wave vector k of the fluorescence light. The corresponding sideband in the fluorescence spectrum is as narrow as the carrier and can therefore be detected even when the limited signal-to-noise ratio does not allow detection of the free oscillation.

Fig. 6.8 shows the amplitude of the carrier and the corresponding sideband as the frequency of the exciting electric field is scanned. The two curves were fitted with functions $|A_n J_n(m(f_{drive}))|^2$, $n = 0$ for the carrier, $n = 1$ for the sideband, where

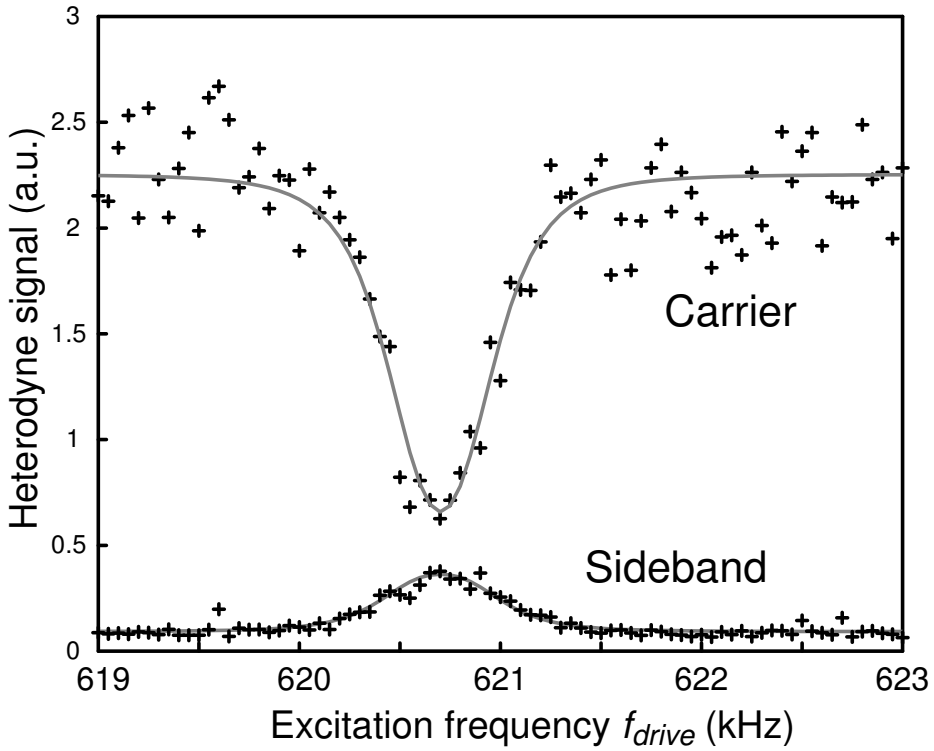

Figure 6.8: Heterodyne signal showing the sizes of the elastic peak (upper trace) and the sideband of the weakly excited macro-motion (lower trace) as functions of the excitation frequency f_{drive}. For the elastic peak the FFT analyzer frequency is kept fixed while for the sideband it is shifted by f_{drive}. The bandwidth is 1 Hz.

$m(f_{drive})$ was assumed as

$$m(f_{drive}) = \frac{m_{Max}}{1 + (\frac{f_{drive} - f_{macro}}{\Delta f/2})^2} \tag{6.18}$$

as expected for a damped harmonic oscillator. The parameters of the fit are the maximum modulation index $m_{Max} = 1.5$ and the width of the macro-motion resonance $\Delta f = 750$ Hz which corresponds to a cooling rate of 750 s^{-1}. The cooling rate can be theoretically estimated with the model described at the end of chapter 2. The parameters used for this estimate were calculated from a fit to an excitation spectrum recorded directly after the sideband spectrum had been measured, i.e. with the same parameter settings. These are the detunings $\Delta_{493\ \mathrm{nm}} = 2\pi * -19$ MHz and $\Delta_{650\ \mathrm{nm}} = 2\pi * 5$ MHz, the saturation parameters $\Omega_{493\ \mathrm{nm}}/\Gamma_{493\ \mathrm{nm}} = 1.4$ and $\Omega_{650\ \mathrm{nm}}/\Gamma_{650\ \mathrm{nm}} = 2.9$, a laser linewidth of $\Gamma_l = 17$ kHz, a magnetic field $\mu = 3.6 * \mu_B$ and an angle between magnetic field and light polarization of 95°. The laser at 650 nm is set to maximum fluorescence, i.e. the population ρ_P does not depend on the red laser detuning to first order, and can therefore be neglected for the calculation of the cooling rate. Then the simple model described in chapter 2 gives a cooling rate

$$\alpha = 2\frac{\hbar k^2}{2M}\Gamma\frac{\partial \rho_P}{\partial \Delta}. \tag{6.19}$$

With the parameters from the excitation spectrum, one calculates a cooling rate of $\alpha = 2\pi * 640\ s^{-1}$ which agrees well with the measurement. The residual disagreement most likely arises because this model assumes that the cooling rate of the ion is not altered due to additional excitation, which is only valid when the amplitude of the driven oscillation is small compared to the laser wavelength (Lamb-Dicke regime). In this case the maximum oscillation amplitude A of the excited motion is $A = m*\lambda/2\pi =$ 120 nm. The dependence of the cooling rate on the excitation parameters has not been investigated further, because after this measurement the Zeiss lens was replaced to achieve a better heterodyne signal and measure the sidebands without excitation.

6.5 High quality lens

6.5.1 Experimental setup

The setup with this lens is shown in Fig. 6.9. As it turned out after lengthy investigations, the experiment just described was limited by the imaging quality of the Zeiss Kollimator. Several alternatives were considered. The most promising was a custom made lens Halo 25/0.4 from Linos Photonics with 0.4 numerical aperture and very low wave front distortion.

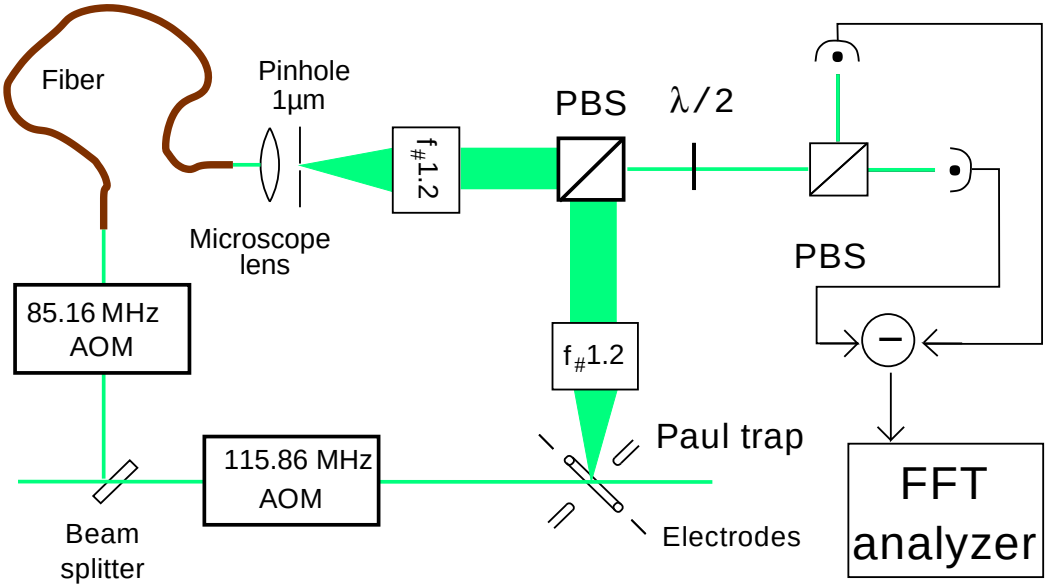

Figure 6.9: Heterodyne experiment with the Halo 25/0.4. The telescope to shape the superimposed beam is not shown.

In order to profit from the high wavefront quality of the fluorescence beam, much more care was taken when generating the local oscillator and superimposing the beams on the polarizing beam splitter. The local oscillator is generated by focusing the laser beam with a microscope objective onto a 1μm pinhole, which is then imaged with a second Halo lens. With this setup, the wavefronts of the fluorescence beam and the local oscillator are made to match as closely as possible. The two beams are superimposed on a high quality PBS[3] which does not add wavefront distortions. The superimposed beams are transformed with a telescope from a diameter of 21 mm to 2 mm. The detector setup is the same as in the Zeiss experiments.

6.5.2 Experimental results

First, the carrier of the coherently scattered light was measured. Fig. 6.10 shows the carrier recorded with a detector bandwidth of 62.5 Hz. The signal-to-shot-noise ratio in this example is 6.1, this corresponds to a SSNR of 386 (26 dB) in 1 Hz detection bandwidth, which is about ten times better than with the Zeiss lens. This SSNR is smaller than the theoretically expected $SSNR = 7500$ (38 dB). The likely reason for this is the still imperfect superposition of the local oscillator and signal beam. While the parallelitism can be controlled very well, the overlap of the beam centers, i.e. the

[3]Halle PTW 30

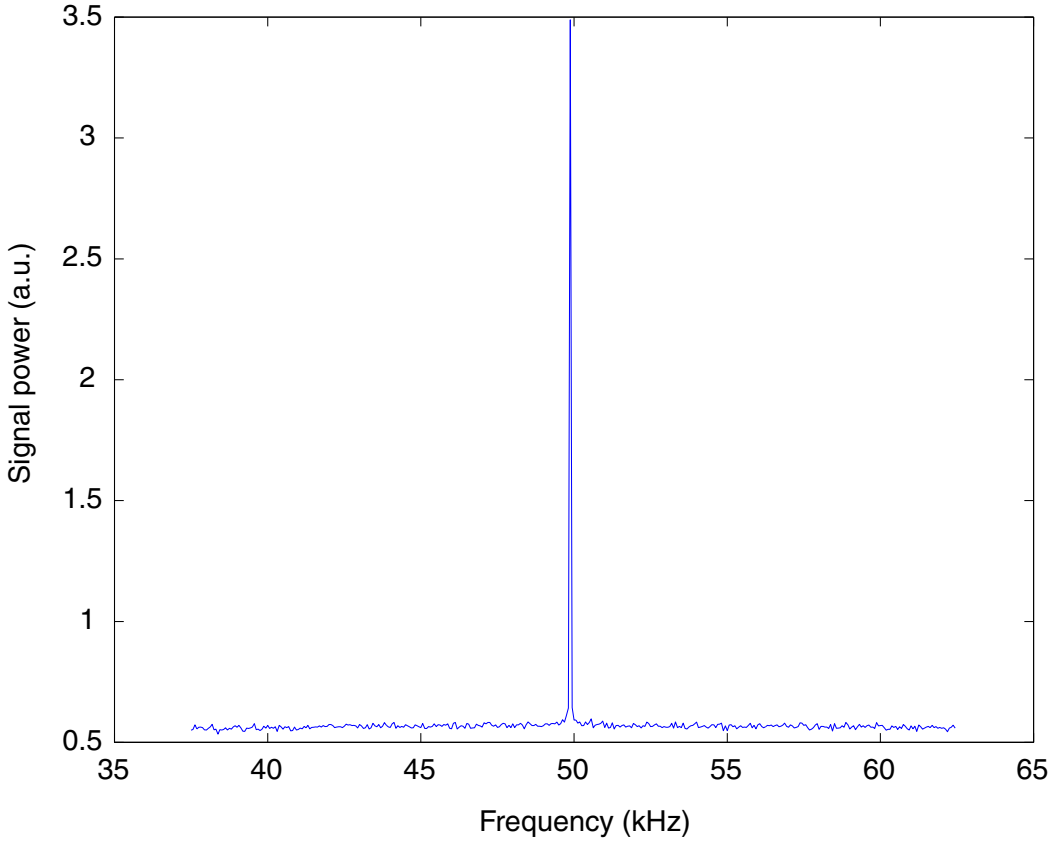

Figure 6.10: Central peak of Rayleigh scattering recorded with Halo 25/0.4. The detection bandwidth has been set to 62.5 Hz. The $SSNR$ is 6.1 and the $ASNR = 400$ in 62.5 Hz. This corresponds to a $SSNR = 386$ in a detection bandwidth of 1 Hz. In this example the carrier peak has 0.35 μV, the shot noise average is 56.5 nV and the standard deviation of the shot noise is 0.9 nV.

spatial offset, is uncertain in the 1 mm range. Nevertheless, this SSNR is sufficient to record the macro-motional sidebands in a reasonable averaging time of about one minute.

A measurement of the macro-motional sidebands is shown in Fig. 6.11 and 6.12. These measurements are the upper x-motional and upper y-motional sideband. The signal-to-shot-noise ratio is ≈0.1 (-10 dB) in 62.5 Hz detection bandwidth, the average signal-to-noise ratio after 1000 averages is about 3. The z-sideband cannot be detected due to the geometry of the setup. A fit of a Lorentzian to the sidebands is displayed in the figures. The full width at half maximum is 620 +574/-416 Hz for the x-sideband and 610 +570/-400 Hz for the y-sideband. The large errors are cause by the low ASNR. This measured cooling rate can again be compared to the simple model, as

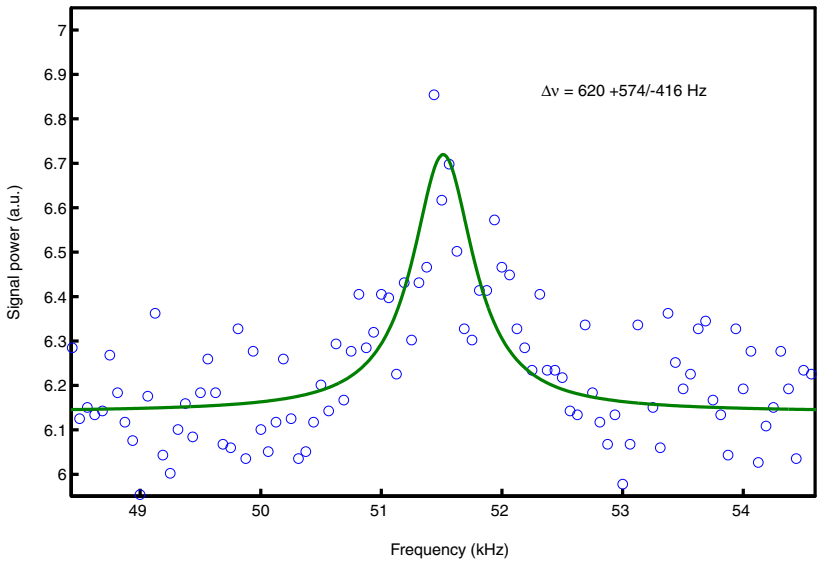

Figure 6.11: Upper x-motional sideband of the macro-motion. The SSNR is about 0.11 in 62.5 Hz detection bandwidth, $ASNR = 5.6$.

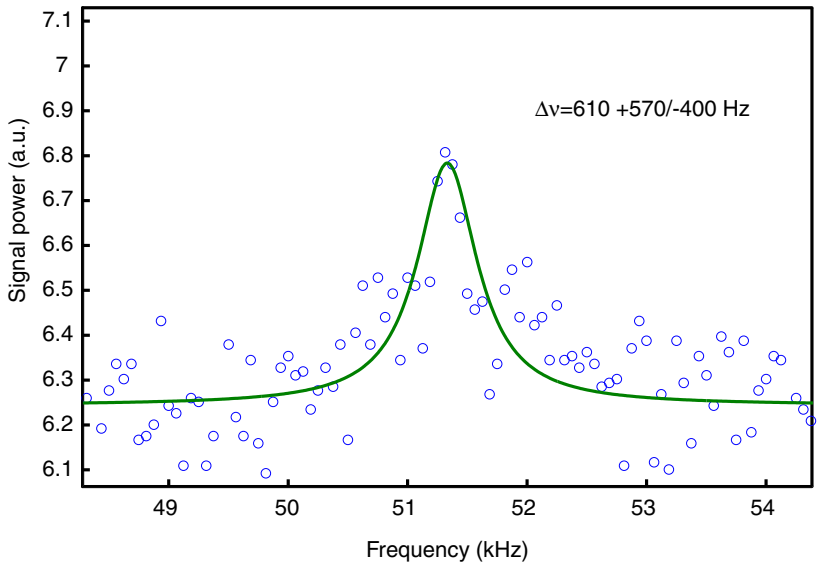

Figure 6.12: Upper y-motional sideband of the macro-motion. The SSNR is about 0.09 in 62.5 Hz detection bandwidth, $ASNR = 4.4$.

described in section 6.4.3. The laser parameters are determined from a fit of optical Bloch equations to the excitation spectrum shown in Fig. 6.13. They are $\Delta\nu_{493} = 2\pi \cdot -20.4$ MHz, $\Delta\nu_{650} = 2\pi \cdot +7$ MHz, $\Omega_{493}/\Gamma_{493} = 0.59$, and $\Omega_{650}/\Gamma_{650} = 2.54$. The magnetic field is $u = 4.4$ MHz μ_0 and the angle between the magnetic field and the

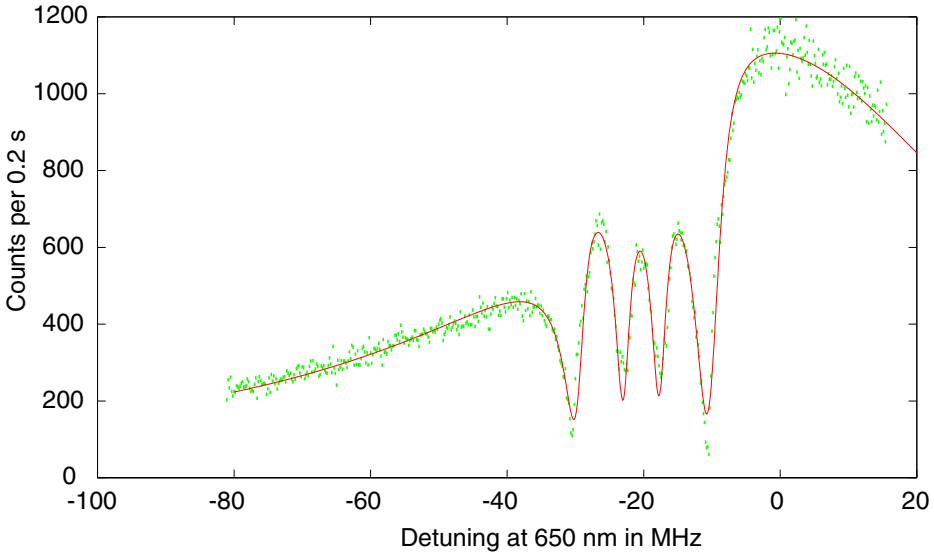

Figure 6.13: Excitation spectrum of a single Ba^+ ion with the same laser parameters as used for recording the sideband spectra in Fig. 6.11 and 6.12

polarization is 91°. As in section 6.4.3, the influence of the red laser on the cooling is neglected. The slope of the population of the excited state versus the green detuning is $\frac{\partial \rho_P}{\partial \Delta \nu_{493}} = 3.6 \cdot 10^{-9} \mathrm{Hz}^{-1}/2\pi$. The cooling rate is given by

$$\alpha = 2\frac{\hbar k^2}{2M}\Gamma_{493}\frac{\partial \rho_P}{\partial \Delta \nu_{493}} \tag{6.20}$$

with $\frac{\hbar k^2}{2M} = 2\pi \cdot 5.9$ kHz and $\Gamma_{493} = 2\pi \cdot 15.1$ MHz. The calculated cooling rate with this model is $\alpha_{th} = 2\pi \cdot 640 s^{-1}$.

Another example is shown in Figs. 6.14 and 6.15. Here the laser parameters are slightly different. They are calculated from the excitation spectrum shown in Fig. 6.16 as $\Delta\nu_{493} = 2\pi \cdot -27.2$ MHz, $\Delta\nu_{650} = 0$ MHz, $\Omega_{493}/\Gamma_{493} = 0.61$, and $\Omega_{650}/\Gamma_{650} = 1.28$. The magnetic field is $u = 4.3$ MHz μ_0 and the angle between the magnetic field and the polarization is 91°. The measured cooling rates from Figs. 6.14 and 6.15 are $\alpha_x = 2\pi \cdot (340\ +500/-140)\ s^{-1}$ and $\alpha_y = 2\pi \cdot (250\ +430/-200)\ s^{-1}$. The calculated cooling rate from the laser parameters with $\frac{\partial \rho_P}{\partial \Delta \nu_{493}} = 1.6 \cdot 10^{-9} \mathrm{Hz}^{-1}/2\pi$ is $\alpha = 2\pi \cdot 289\ s^{-1}$, which is in good agreement with the measured value.

In this chapter the measurement of the coherent part of the fluorescence spectrum was described. The experiment was focused on measuring the motional sidebands of a trapped Ba^+ ion. With the Zeiss lens it was possible to detect the carrier and the micro-motional sidebands in the spectrum of resonance fluorescence. However, the achivable SSNR was limited by the optics to 50 in 1 Hz on the carrier. The sidebands

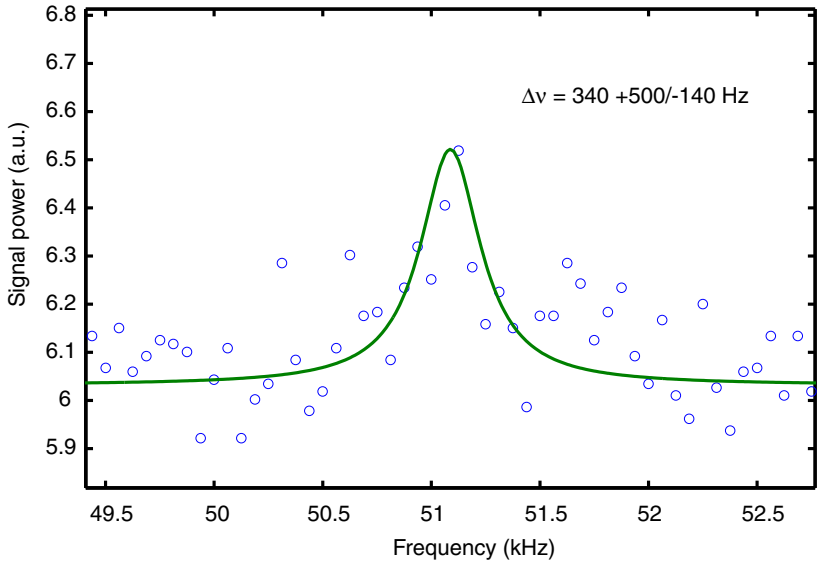

Figure 6.14: Upper x-motional sideband of the macro-motion. The SSNR is about 0.08 in 62.5 Hz detection bandwidth, $ASNR = 4.2$.

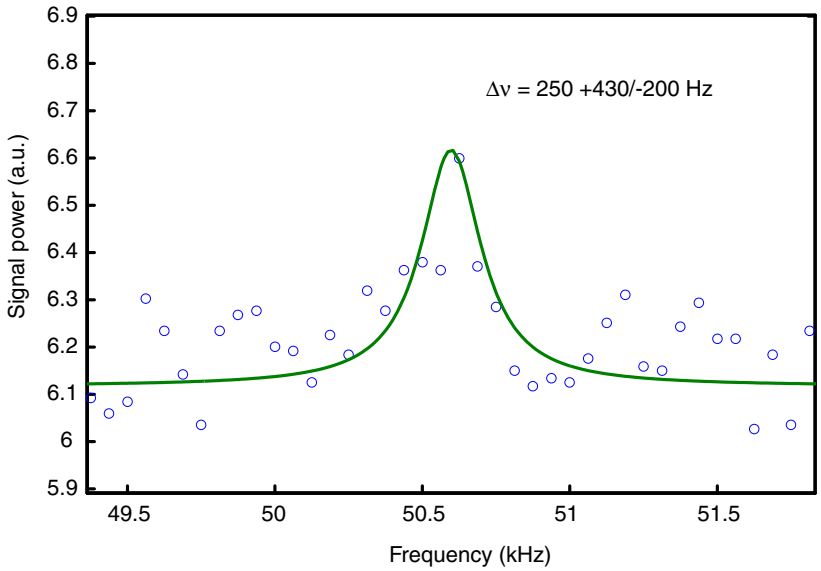

Figure 6.15: Upper y-motional sideband of the macro-motion. The SSNR is about 0.09 in 62.5 Hz detection bandwidth, $ASNR = 4.9$.

of macro-motion could be detected by weakly exciting the ion with an electric field and measuring the sideband at the exciting frequency. With this method, the cooling rate of the ion was determined.

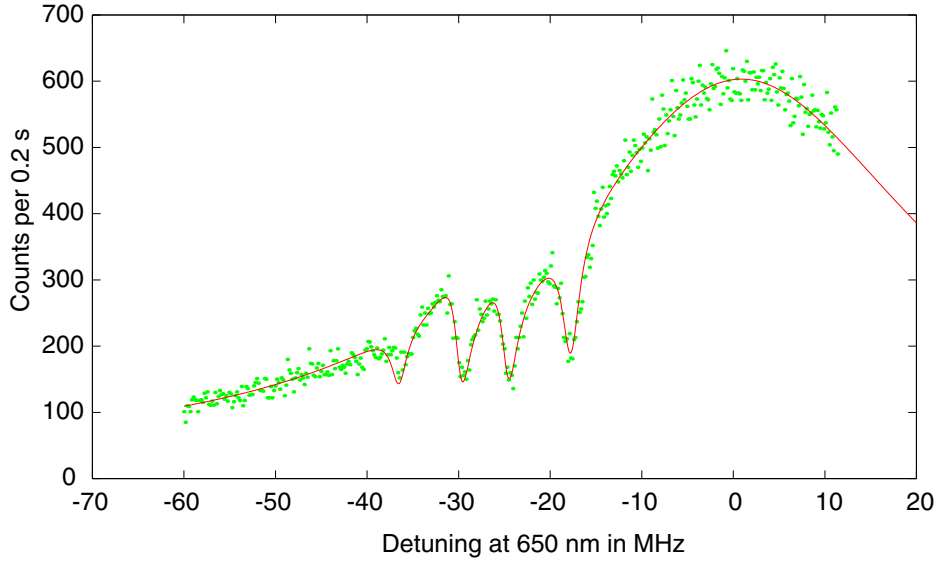

Figure 6.16: Excitation spectrum of a single Ba^+ ion with the same laser parameters as used for recording the sideband spectra in Fig. 6.14 and 6.15

The detection scheme was enhanced by replacing the Zeiss lens with a custom made lens, the HALO 25/0.4, which has a very good beam quality. With this setup, the SSNR on the carrier was improved by a factor of nearly 10 to give a SSNR=400 (26 dB) maximum. We were also able to detect the macro-motional sidebands directly with an SSNR=0.1 (-10 dB) in a detection bandwidth of 62.5 Hz. The measured width of the sideband is in good agreement with the value determined by the simple model described in section 6.4.3.

The maximum SSNR achieved is still about a factor of 10 smaller than expected for a perfect superposition of local oscillator and fluorescence beam. A factor of 2 can be gained by enhancing the detection electronics. At the moment noise from the mirror frequency is mixed into the signal, increasing the noise by a factor of 2. This can be avoided by first bandpass filtering to remove this noise. Also, the generation of the local oscillator and the overlap of the two beams can be improved by better control of the spatial overlap.
If the SSNR on the macro-motional sidebands can be improved to be larger than 1, one could gain real time information about the ion's motion, i.e. as fast or faster than the damping of the motion. This signal could then be fed back onto the ion either by modulation the lasers or with an electric field to directly cool the motion.

7 Interference experiments with single ions

This chapter presents the second part of the main experimental results of this thesis. At the beginning, the objective of these measurements was to test the image quality of the new HALO 25/0.4 lens. Therefore, an interference experiment was setup in which the light emitted from the ion into the front channel was superimposed with light reflected back from the back channel, as shown in Fig. 7.1. In the course of the experiment it turned out that, the results cannot be explained with a simple light interferometer but it is necessary to include the internal dynamics of the ion, its motion and, furthermore, the influence of the ion-mirror distance on the internal state of the ion.

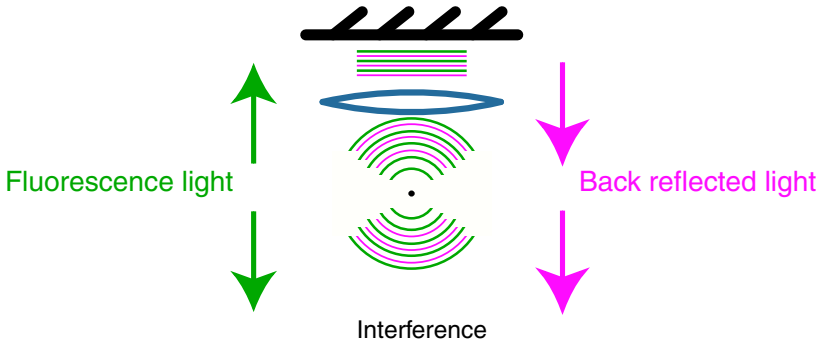

Figure 7.1: Principle of the interference experiment

The lens and the mirror together form a half-cavity. Due to the large solid angle collected by the HALO 25/0.4, the focus is very tight, $\approx 1\mu$m, and the mode volume is correspondingly small. The ion can be shifted into a node or an anti-node of the standing light field created by the mirror, by changing the distance between ion and mirror with a piezo ceramic. The light which is emitted into the front channel, i.e. the opposite direction of the mirror, is detected as a function of the mirror position.

First, a simple theoretical model is given, then the experiment is described.

7.1 Simple Model

The idea of this experiment is, as shown in Fig. 7.1, to collect a part of the fluorescence light of an ion and reflect it back onto the ion with a mirror. One can try to describe this experiment with a modified Mach-Zehnder interferometer setup, shown in Fig. 7.2. This approach is, however, not sufficient, because it neglects the influence of the

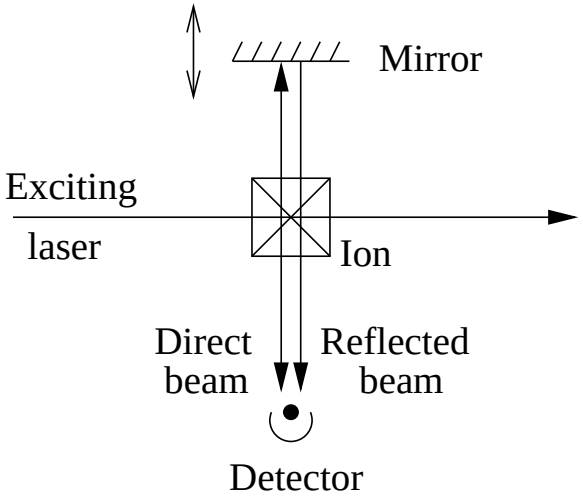

Figure 7.2: Simple, but wrong picture

standing wave produced by the mirror on to the ion.
A better model has to include the back action of the fluorescence light onto the ion. The intensity recorded in the front channel is given by

$$I =< [\hat{E}^{\dagger}(t) + \hat{E}^{\dagger}(t+\tau)][\hat{E}(t) + \hat{E}(t+\tau)] > \tag{7.1}$$

with the time distance $\tau = 2L/c$ given by the distance L between ion and mirror. The electric field operator can also be written in terms of atomic flip operators $\hat{\sigma}^-$ and $\hat{\sigma}^+$, see chapter 3

$$I = I_0 < [\hat{\sigma}^+(t) + \hat{\sigma}^+(t+\tau)][\hat{\sigma}^-(t) + \hat{\sigma}^-(t+\tau)] > . \tag{7.2}$$

This expression can be rewritten in terms of the first order correlation function of the fluorescence light

$$I = 2I_0[1 + \mathrm{Re}(g^{(1)}(\tau)e^{-i\omega_l\tau})]. \tag{7.3}$$

One finds that the light intensity is modulated according to the phase delay between the direct part and the reflected part, $e^{-i\omega_l\tau}$. The visibility of the modulation, assuming perfect reflection and perfect superposition of the two contributions, is given by $g^{(1)}(\tau)$, i.e. it depends on the atomic dynamics during the time the field travels to the

mirror and back. This shows already that the atom itself is involved in the observed interference, which is why the simple 2 beam interferometer picture cannot be correct. The back action onto the ion can be described by modifying the decay operators $\hat{C}_m$ of atomic states used in the optical Bloch equations, see chapter 3. The standard atomic flip operator is

$$\hat{C} = \sqrt{\Gamma}\ |g\rangle\langle e| = \sqrt{\Gamma}\ \sigma^-. \tag{7.4}$$

This operator is now split into two parts, the decay into free space, which is not affected by the mirror, and the decay into the mode volume affected by the mirror. The unaffected part is

$$\hat{C}'' = \sqrt{(1-2\phi)\Gamma}\ \sigma^- \tag{7.5}$$

with ϕ being the fraction of the solid angle in which light is collected by the lens and back reflected by the mirror. The modified part is given by

$$\hat{C}' = \sqrt{\phi\Gamma}\ (\sigma^-(t)\ e^{-i\omega_l t} + \sigma^-(t+\tau)\ e^{-i\omega_l(t+\tau)}). \tag{7.6}$$

Assuming the atomic evolution is much slower than the time τ, one can write

$$\hat{C}' = \sqrt{\phi\Gamma}\ \sigma^-\ (1 + e^{-i\omega_l\tau}). \tag{7.7}$$

This decay operator represents the situation that the two decay channels, a photon emitted directly into the detector and a photon which reaches the detector after reflection, are indistinguishable in the observation such that their amplitudes have to be added. In the experiment the solid angle of the lens is $4\pi\ \phi = 4\pi\ 0.04$. The atomic decay rate on $P_{1/2} \rightarrow S_{1/2}$ can therefore be changed by up to 8%.

7.2 Experimental setup

The setup of the interference experiment is shown in Fig. 7.3. The high quality lens (L1) collects the fluorescence light of the ion in 4% solid angle and images it into a Gaussian beam with $z_0 \approx \infty$. The fluorescence light at 493 nm is reflected back with a mirror (M1). The distance between the ion and the mirror is 25 cm. The mirror can be aligned with a precision mirror mount and, additionally, with two PZTs for fine tuning. The distance between the mirror and the ion is varied with a PZT. The light emitted into the direction opposite to that of the mirror is collected with a second lens (L2) and detected with a photo multiplier (PM2). The coarse alignment of the mirror M1 can be controlled with the eye through L2. When the mirror is misaligned, one sees two spots, one being the ion and the other its mirror image. The mirror is aligned such that both spots overlap maximally. Then, in the fluorescence recorded with PM2, interference fringes are observed as a function of the mirror distance. The visibility of these fringes is optimized by tuning the voltages applied to the PZT of

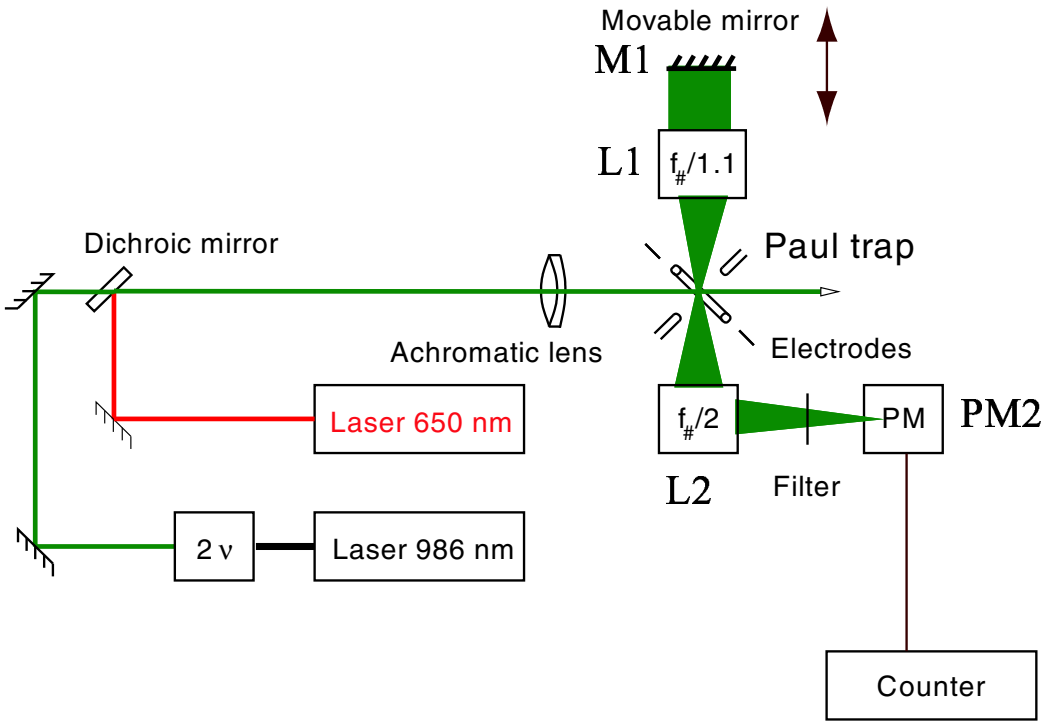

Figure 7.3: Setup of the interference experiments

the mirror mount. A typical interference pattern with a visibility of ≈40% is shown in Fig. 7.4. The measured data was fitted with a sine function. The parameters were the amplitude and offset. Due to the non-linearity of the piezo, it was necessary to fit the x-axis with a third order polynomial.

7.3 Visibility of the fringes

The visibility of the interference fringes is limited by several factors. The most obvious factor is the optical quality of the ion-image superposition. It is limited by the wavefront qualities of the lens L1, the vacuum window and the mirror M1. From the data sheet of the lens one can expect a visibility of 80%-90% measured with a Zeigo interferometer.

Another limiting factor is the motion of the ion along the optical axis of the lens, which averages over the interference fringes and lowers the visibility. This contribution is calculated as follows. The phases of the two paths into the detector vary due to the

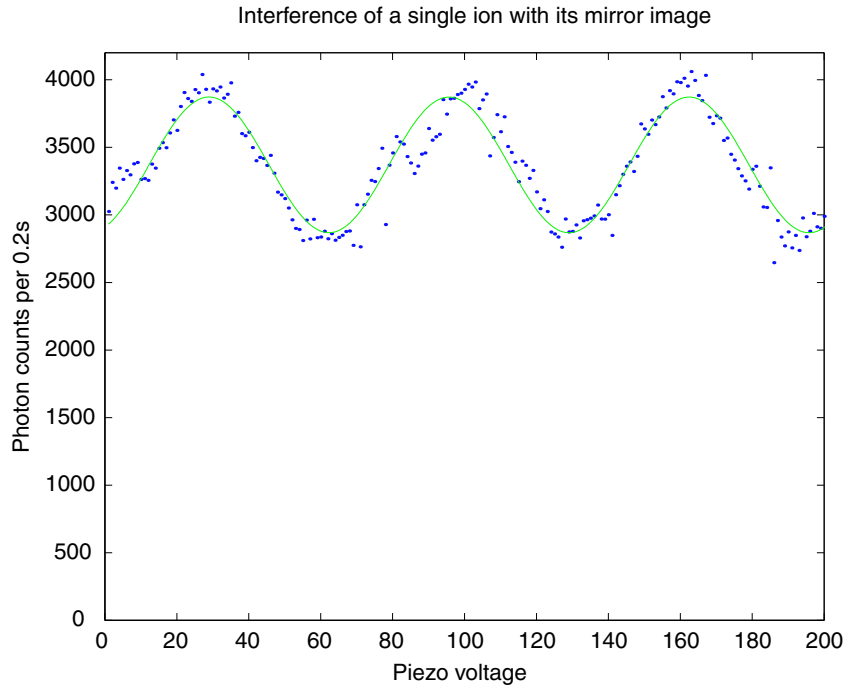

Figure 7.4: Interference of a single ion with its mirror image.

motion of the ion $\dot{x}$ like

$$\frac{\mathrm{d}\phi_1}{\mathrm{d}t} = -\omega_0 - k\dot{x} \text{ for the direct part} \tag{7.8}$$

$$\frac{\mathrm{d}\phi_2}{\mathrm{d}t} = -\omega_0 + k\dot{x} \text{ for the indirect part.} \tag{7.9}$$

Assuming the ion oscillates harmonically $x(t) = x_0 \sin(\omega t)$ with frequency Ω, amplitude x_0, and the wavenumber k of the fluorescence light, the intensity measured on the photo detector at time t is

$$I(t) = |e^{-ikx_0 \sin(\Omega t)} + e^{2ikL} e^{+ikx_0 \sin(\Omega t)}|^2 = 4\cos^2[k(2L + x_0 \sin \Omega t)]. \tag{7.10}$$

Averaging over many coherent oscillation periods gives

$$< I >= 2(1 + \cos(k2L)\mathrm{J}_0(2\eta)) \tag{7.11}$$

with $\eta = kx_0$ and J_0 being the zero order Bessel function. The visibility of the fringes is thus limited by the factor $\mathrm{J}_0(2\eta)$. The trapped ion is not oscillating with a fixed amplitude, but in a thermal state, therefore one has to integrate over all possible harmonic oscillation amplitudes with the weight $g(\eta)$ which is given by the thermal

excitation of the ion. The average detected intensity is then

$$I_{therm} = 2(1 + \cos(k2L)\exp(-\frac{\eta_{therm}^2}{2})\mathrm{I}_0(\frac{\eta_{therm}^2}{2}) \tag{7.12}$$

with the thermal spread η_{therm} and I_0 being the modified zero order Bessel function. Fig. 7.5 shows the visibility as a function of the thermal spread η_{therm}.

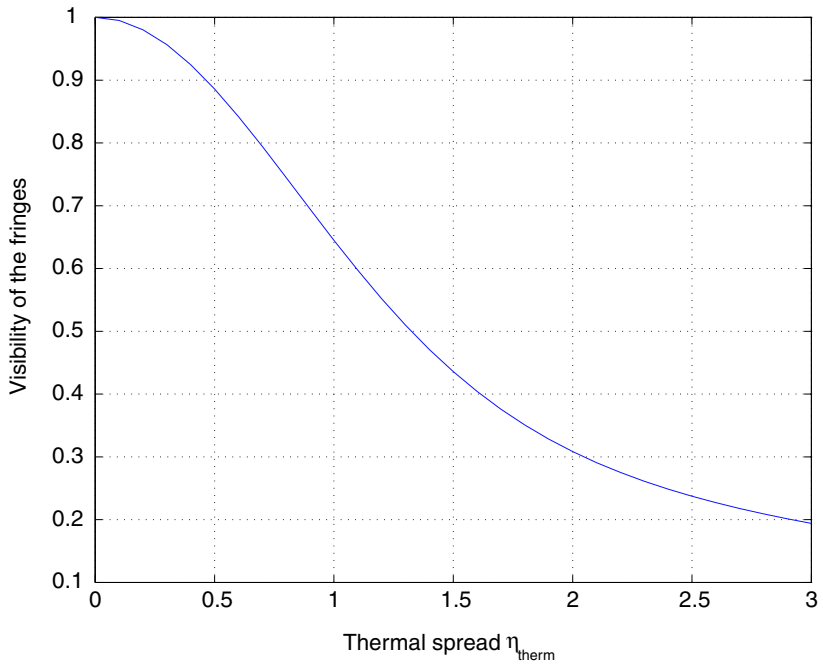

Figure 7.5: Calculated visibility of the interference fringes as a function of the thermal spread η_{therm}.

Another contribution which lowers the visibility is the coherence of the light emitted at time t and reflected by the mirror, with the light emitted at time $t+2L/c$ and detected directly. This contribution can be calculated, as shown in Eqs. (7.1) to (7.3), from the first order coherence function $g^{(1)}(2L/c)$ for various laser parameters. A measurement of the visibility of the interference fringes versus the green laser intensity was made, as shown in Fig. 7.6. However, this measurement shows a large discrepancy between the experiment and the model including only the coherence function $g^{(1)}(2L/c)$. The reason for this is that a change in laser intensity alters the temperature of the ion also. A calculation including the laser cooling isn't done yet.

When the ion is well cooled and the optics are optimized, the visibility can be as high as 72%, as demonstrated in Fig. 7.7.

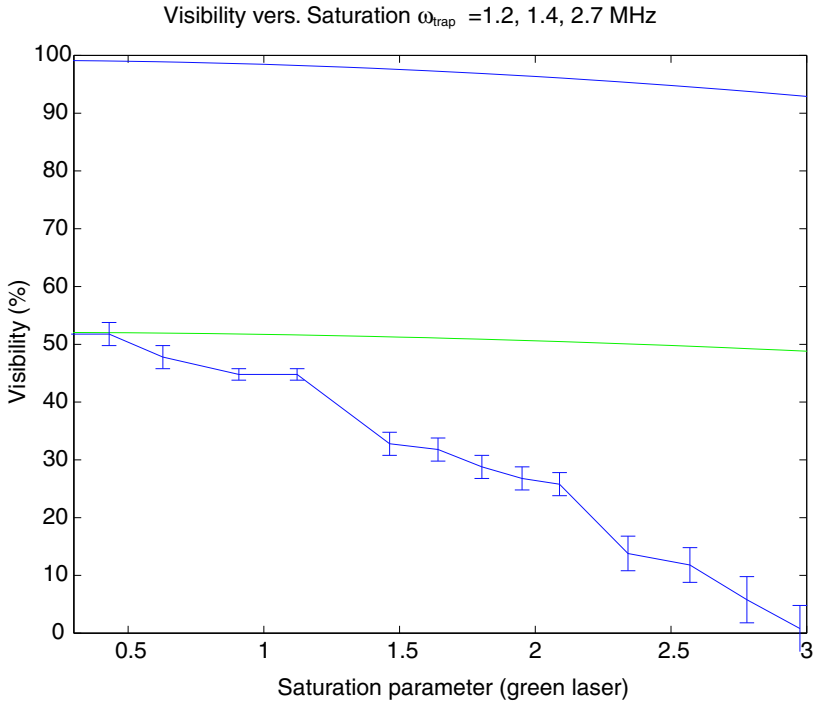

Figure 7.6: Visibility of the interference fringes as a function of the saturation parameter on the green transition. The lower curve are the measured data. The calculated $g^{(1)}$ is shown in the upper curve. In the middle curve the visibility is normalized to the visibility in the experiment for low saturation. The discrepancy between the experimental data and the theoretical curve is due to changes of the ion's temperature for different laser intensities.

7.4 Modification of the spontaneous emission rate

A valid description of the observed interference is that the presence of the lens-mirror system causes a change in the mode density of the electric field around the ion. Depending on the mirror distance, i.e. whether the ion sits in a node or in an anti-node of the standing wave, the vacuum field in the 4% solid angle of the lens and in the 4% in the opposite direction can be suppressed completely or enhanced by a factor of two. This leads to the observed suppression or enhancement of the green fluorescence in the direction opposite to the mirror. The spontaneous emission rate into the remaining 92% solid angle is not modified, leading to a maximum change of ±8% in the total spontaneous emission rate when the visibility is 100%.

In order to observe a modification of the total spontaneous emission, one has to find a measure for the population of the $P_{1/2}$ state. In the case of Ba^+, a good measure is the fluorescence light from the $P_{1/2} - D_{3/2}$ transition at 650 nm. This red fluorescence

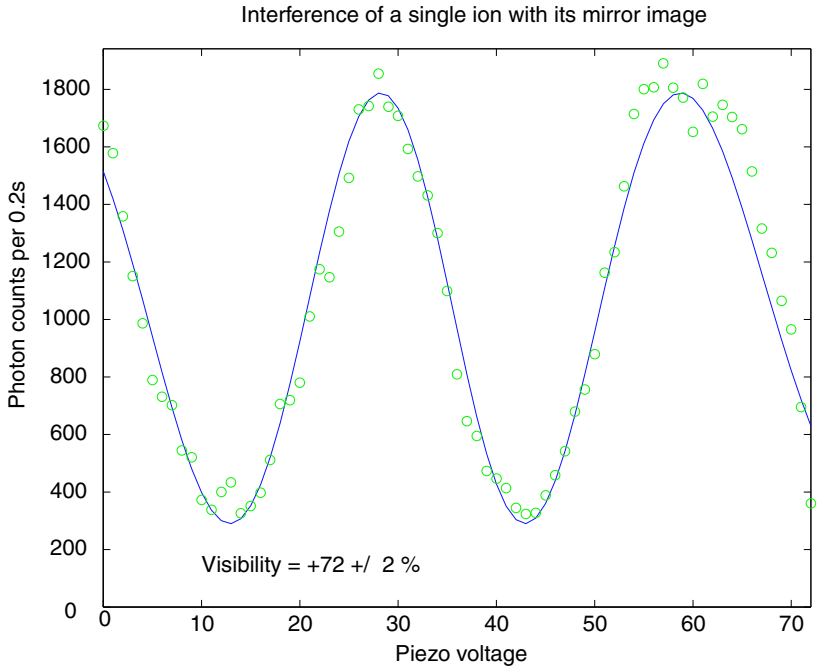

Figure 7.7: Interference fringes of a cold ion with a visibility of 72%.

is also collected with the lens L1, but transmitted through the mirror M1, which has more than 90% transmission at 650 nm, so that the fluorescence at 650 nm can be counted with a second photo-multiplier (PM2).

Such a measurement of the red fluorescence while scanning the mirror M1 is shown in Figs.7.8 and 7.9. The visibility of the fringes at 493 nm is 47% in this case. The reason for the small visibility is that the laser parameters were chosen so that the ion was bright, but with these parameters the cooling is degraded. The amplitude of the modulation at 650 nm, which is found by a fit of a sine function to the measured fluorescence at 650 nm, is 0.9%. The x-axis was taken from the fit to the fluorescence at 493 nm. Additionally, a small modulation with a different periodicity, which is 650/493 slower, was observed with an amplitude of 0.2%. This is likely due to small reflections from the vacuum window.

As mentioned above, the mirror-lens system can modify the spontaneous emission rate in a solid angle of 8%. If the superposition of ion and mirror image is perfect, and for an ion at rest, the spontaneous emission rate is $\Gamma_{node} = 0.92 \cdot \Gamma_{nat}$ when the ion is in a node and $\Gamma_{anti} = 1.08 \cdot \Gamma_{nat}$ when the ion is in a anti-node. Due to the ions motion, one has average over the thermal spread of the ion in order to calculate the modified emission rate Γ. In first order, this can be done by multiplying the change of $\pm 8\%$ for an ion at rest with the visibility of the fringes. One gets $\Gamma_{node} = 0.963 \cdot \Gamma_{nat}$ and

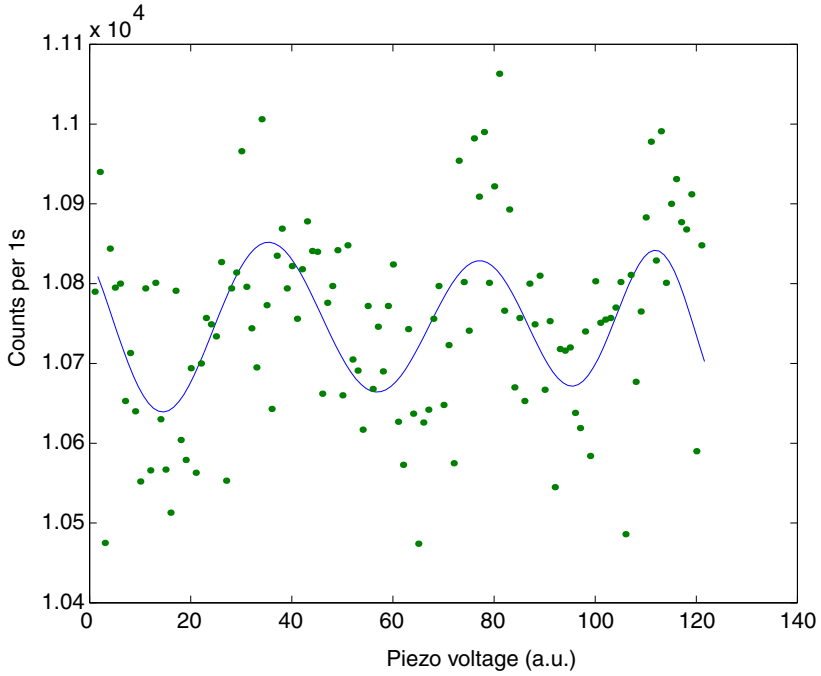

Figure 7.8: Fluorescence at 650 nm while scanning the mirror M1.

$\Gamma_{anti} = 1.037 \cdot \Gamma_{nat}$ for a visibility of 47% at 493 nm.

The population in the $P_{1/2}$ state can be calculated by using the modified decay constants Γ_{node} and Γ_{anti} in the optical Bloch equations. This is equivalent to the modified decay operators described in the section 7.1. Fig. 7.10 shows calculated excitation spectra with different spontaneous decay rates $\Gamma/\Gamma_{nat} = 0.963,\ 1,$ and 1.037.

The visibility of the fringes at 650 nm $v_{650\ nm}$ is given by

$$v_{650\ nm} = \frac{\rho_{P_{1/2}}(node) - \rho_{P_{1/2}}(anti)}{\rho_{P_{1/2}}(node) + \rho_{P_{1/2}}(anti)} \tag{7.13}$$

with the populations in the $P_{1/2}$ state $\rho_{P_{1/2}}(node)$ and $\rho_{P_{1/2}}(anti)$ for the decay constants Γ_{node} and Γ_{anti}, respectively. The visibility at 650 nm $v_{650\ nm}$ for the same laser parameters as in Fig. 7.10 is shown in Fig. 7.11. The modification of the population with the used laser parameters is in the range of 2% to -1.7%. The strong dependence on the detuning of the red laser, and especially the changes of sign, are remarkable. A measurement of this effect could be used to confirm the explanations and models outlined here. But such a measurement would require longer measurement times and, therefore, a more stable setup, because the fluorescence level at the corresponding laser detunings is much smaller.

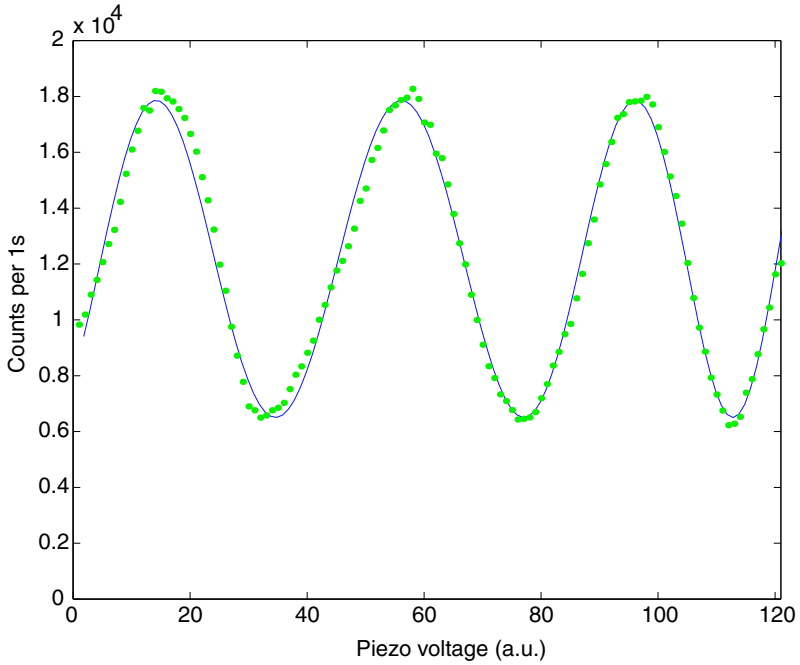

Figure 7.9: Interference fringes at 493 nm while scanning the mirror M1.

7.5 Interference experiments with two ions

A similar experiment can be carried out with two ions. It is possible to either reflect the fluorescence light of one ion back onto itself, or the mirror image of one ion can be superimposed with the real image of the second one. These two cases are sketched in Fig. 7.12. In the first case, the experiment is the same as above. The contrast is reduced, because only half of the fluorescence contributes to the interference and because in a spherical trap two ions have strong micro-motion. In the second case, the fluorescence light of one ion interacts with the second ion. This interaction can be described using a similar model as for one ion. Both ions can be well resolved with the optics in the front channel. Therefore, it is possible to measure separately the intensity of one ion plus the mirror image of the second ion from the intensity of the second ion plus the mirror image of the first. The intensities observed from ion one plus mirror image of ion two and ion two plus mirror image of ion one, respectively, are

$$I_1 =< [\hat{E}_1^\dagger(t) + \hat{E}_2^\dagger(t+\tau)][\hat{E}_1(t) + \hat{E}_2(t+\tau)] > \quad (7.14)$$

$$I_2 =< [\hat{E}_2^\dagger(t) + \hat{E}_1^\dagger(t+\tau)][\hat{E}_2(t) + \hat{E}_1(t+\tau)] > \quad (7.15)$$

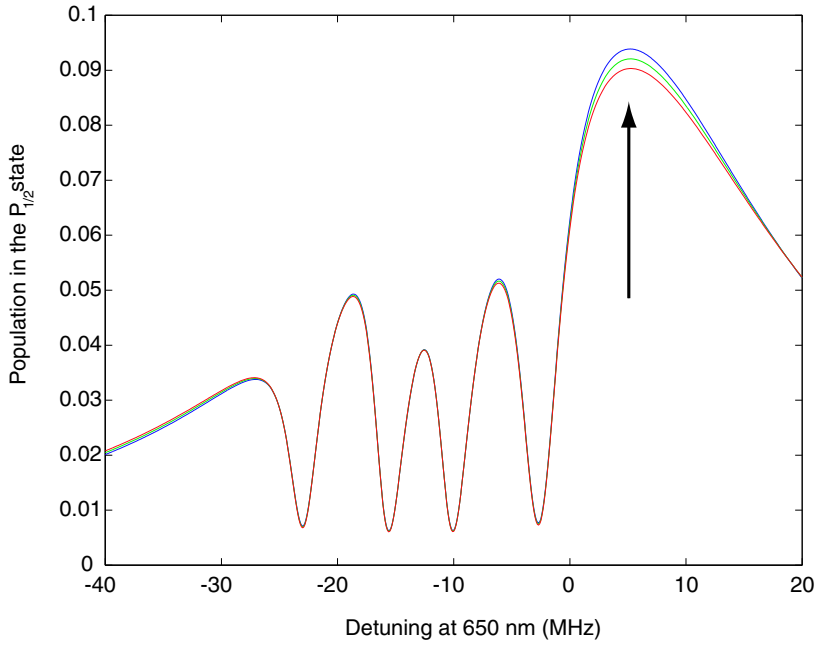

Figure 7.10: Modified excitation spectra with $\Gamma/\Gamma_{nat} = 0.963,\ 1$ and 1.037. The parameters are $\Delta_g = -12.98$MHz, $S_g = 0.74$, $S_r = 1.68$, $\Gamma_L = 58$ kHz, $u = 4.61$MHz and $\alpha = 90°$. For the measurement of the interference fringes, the red laser was tuned to maximum fluorescence.

with electric field $\hat{E}_1$ of ion one and $\hat{E}_2$ of ion two. This can be written in terms of the atomic flip operators

$$I_1 = I_0 < [\hat{\sigma}_1^+(t) + \hat{\sigma}_2^+(t+\tau)][\hat{\sigma}_1^-(t) + \hat{\sigma}_2^-(t+\tau)] > \quad \text{and} \tag{7.16}$$

$$I_2 = I_0 < [\hat{\sigma}_2^+(t) + \hat{\sigma}_1^+(t+\tau)][\hat{\sigma}_2^-(t) + \hat{\sigma}_1^-(t+\tau)] > . \tag{7.17}$$

The intensity observed with the current setup is the sum of both intensities.
The interaction of ion and fluorescence light can be described in a similar model as used in section (7.1). The two ions are described by their combined density matrix $\hat{\rho}_1 \otimes \hat{\rho}_2$. The free decay operators for the two ions are

$$\hat{C}_1 = \sqrt{\Gamma}|g_1\rangle\langle e_1| \cdot \hat{1}_2 = \sqrt{\Gamma}\sigma_1^- \cdot \hat{1}_2 \quad \text{and} \tag{7.18}$$

$$\hat{C}_2 = \sqrt{\Gamma}|g_2\rangle\langle e_2| \cdot \hat{1}_1 = \sqrt{\Gamma}\sigma_2^- \cdot \hat{1}_1. \tag{7.19}$$

The modified decay operators are

$$\hat{C}_1' = \sqrt{\phi}\ (\hat{C}_1 \cdot \hat{1}_2 + e^{-i\omega\tau}\hat{C}_2 \cdot \hat{1}_1) \quad \text{and} \tag{7.20}$$

$$\hat{C}_2' = \sqrt{\phi}\ (\hat{C}_2 \cdot \hat{1}_1 + e^{-i\omega\tau}\hat{C}_1 \cdot \hat{1}_2). \tag{7.21}$$

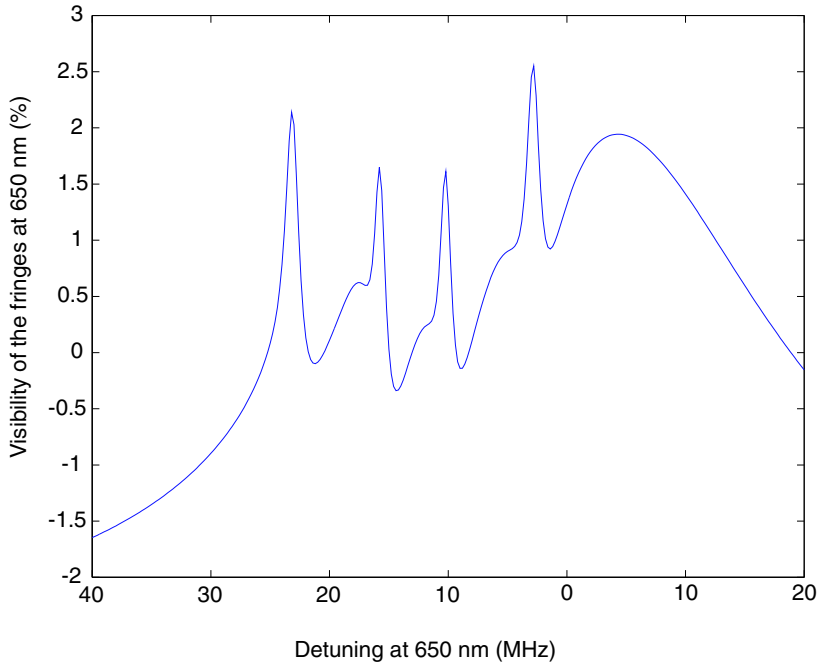

Figure 7.11: Visibility of fringes at 650 nm for different red laser detunings. The parameters used to calculate the population in the $P_{1/2}$ state are the same as in Fig. 7.10

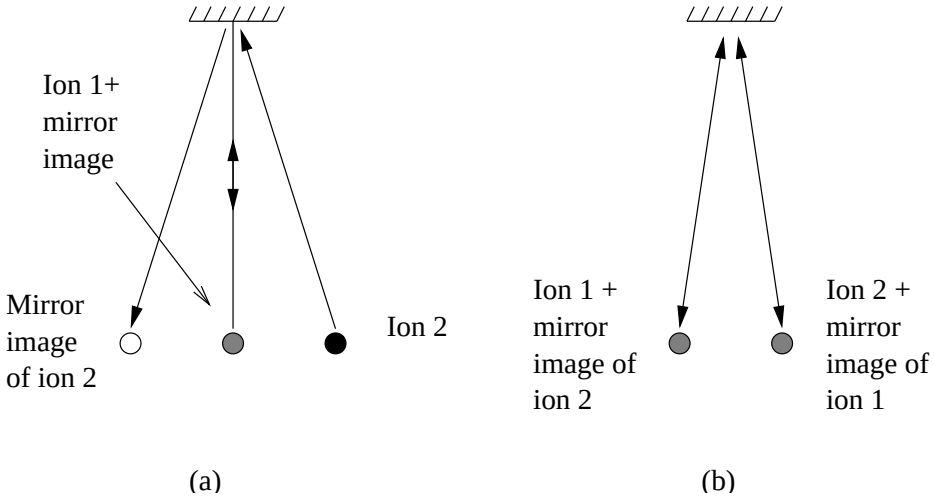

Figure 7.12: Interference experiment with two ion. (a) The light of one ion is reflected back onto itself. The reflected light of the other ion is separated. (b) The light of ion one is reflected onto the the second ion and vice versa.

The decay of the two ion system is given, see section (3.2), by

$$\mathcal{L}_{damp}(\hat{\rho}) = -\frac{1}{2}\sum_m \hat{C}_m^\dagger \hat{C}_m \hat{\rho} + \hat{\rho}\hat{C}_m^\dagger \hat{C}_m. \tag{7.22}$$

Using the modified decay operators from (7.20), Eq. (7.22) contains a part

$$\mathcal{L}_{part} = \phi\Gamma(\sigma_1^- \cdot \sigma_2^- + \sigma_2^- \cdot \sigma_1^-)\cos(\omega\tau), \tag{7.23}$$

i.e. a photon which is emitted by one ion can be absorbed by the other ion. The interaction between the two ions is limited by the solid angle, which is collected by the lens, in this case 4%.
Fig. 7.13 shows an interference experiment with two ions, where the mirror image of the second ion was superimposed with the first and vice versa. The visibility of the fringes in this example is 5%. The visibility is limited mainly due to the motion of the ions, which a have strong excess micro-motion, because in a spherical trap only a single ion can be brought into the center of the trap. This limited visibility makes it difficult to investigate the two-ion case further with the current spherical trap. However, the observed interference fringes and our model clearly indicate sub- and super-radiant effects in this system.

In summary, the experiments described in this chapter demonstrated the influence of a half-cavity, consisting of a lens and a mirror, on single, trapped ions. In the case of a single Ba^+ ion, the interference fringes observed in the front channel have a visibility of up to 72%. It was shown that the visibility depends strongly on the temperature of the ion and on the laser intensity. Furthermore, the visibility of 72% puts an upper limit on the wavefront aberration of the lens HALO 25/0.4 which is $\lambda/16$ (rms) at $\lambda = 493$ nm.

The interaction of the ion with the standing vacuum field generated by lens and mirror was demonstrated by measuring the fluorescence intensity at 650 nm which is proportional to the population of the $P_{1/2}$ state. This measurement revealed a dependence of the red fluorescence of $\pm 1\%$ on the position of the mirror. This modulation is anti-correlated with the interference observed at 493 nm as expected from the calculations. However, for other laser parameters, e.g. large red detuning, one expects the modulation at 650 nm to change its sign. To observe this, longer measurement times are necessary because the fluorescence level at these detunings is lower and therefore the noise is higher.

The two ion experiment also showed interference fringes, which can be explained by the interaction of the two ions via the fluorescence light. Preliminary results showed a fringe visibility of 5%. In order to study the two ion case, one should replace the current spherical trap with a linear trap. Also, higher macro-motion frequencies would reduce the dependence of the fringe visibility on the temperature, because the thermal spread for a given temperature decreases for increasing trap frequencies.

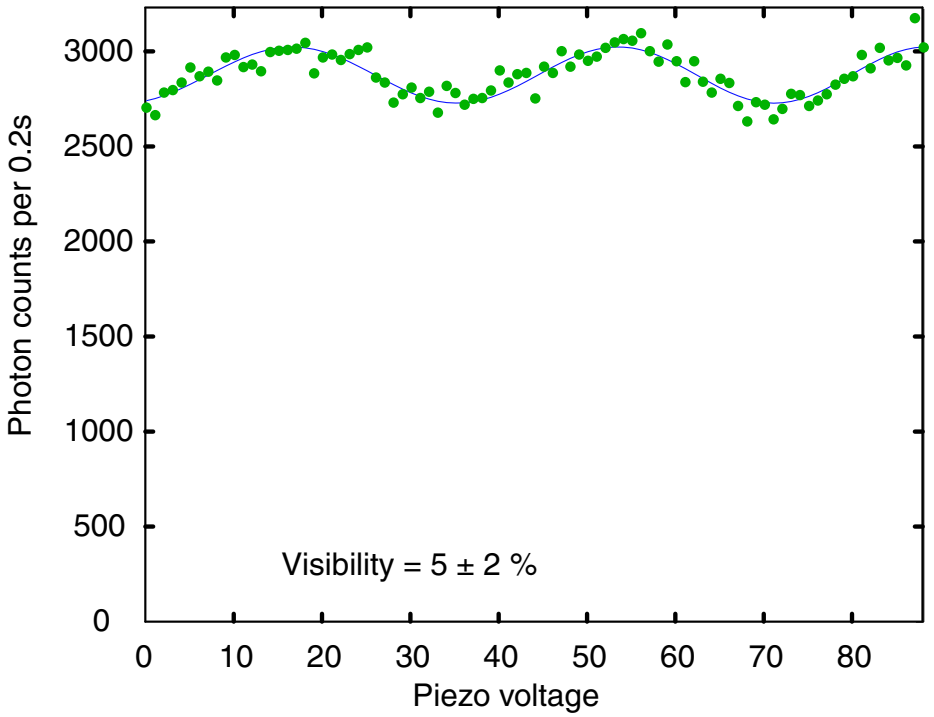

Figure 7.13: Interference of the fluorescence light of one ion with the light of a second ion.

8 Summary and conclusions

I have described several experiments in which the resonance fluorescence of a single Barium ion in a Paul trap is investigated and manipulated with various interference techniques.

The work presented started with the setup of the diode laser system at 493 nm and the improvement of the laser at 650 nm. The initial experiments, described in chapter 6, were carried out with a trap apparatus built in [56]. With this trap it was possible to reliably store single Ba^+ ions over a period of about one hour. The Ba^+ ions were routinely cooled to the Lamb-Dicke regime with laser cooling. Excitation spectra and correlation measurements of $g^{(2)}(\tau)$ could be measured with various different laser parameters. Thus, the trap and the diode lasers were specified and understood. The first interference experiment with the fluorescence light was also conducted in [56]. A Mach-Zehnder type interferometer was placed in one observation channel, and interference fringes with a visibility of 82% were observed. By measuring the intensity correlation function it was verified that not more than one photon is in the interferometer at any time.

Furthermore, first measurements of the spectrum of the resonance fluorescence of single or two Ba^+ ions were conducted. The carrier of the spectrum was measured with a resolution of 61 mHz. Also, the sidebands of the micro-motion were directly measured. The cooling rate of laser cooling was recorded by probing the macro-motion resonance with a small electric excitation. The signal to noise ratio was limited to 50 (17 dB) on the carrier in a bandwidth of 1 Hz due to the wavefront aberrations of the collimation optics. Therefore, this lens was replaced by a custom made, high-quality lens. The trap apparatus was also modified to include a better vacuum pump, reducing the pressure in the trap chamber by two orders of magnitude. With this setup it was possible to conduct interference experiments with the fluorescence light with a high signal to noise ratio.

The measurement of the fluorescence spectrum was repeated with the new lens. The signal to shot noise ratio on the carrier was increased by a factor of about 10. The sidebands of macro-motion were observed with a signal-to-shot-noise ratio of 0.1 in an average time of about one minute. They were fit with a Lorentzian, and their measured width, which is equivalent to the cooling rate of the ion, is in good agreement with the theoretical prediction.
The signal to shot noise ratio could be enhanced by improving the superposition of

the fluorescence beam and local oscillator. At the moment, the relative position of the beam centers can only be measured with an uncertainty of about 1 mm, and it is difficult to adjust without changing other beam parameters. Also, the simulation of the ion in the local oscillator with a 1 μm pinhole could be improved. Another factor of two would be gained by filtering the photo diode signal with a narrow passband before the mixing stage. This rejects the noise from the mirror frequency, which at the moment is added to the heterodyne signal. With the described improvements, it should be possible to reach a signal-to-shot-noise ratio on the macro-motional sidebands larger than one. Then the signal can be used to gain information about the ion's motion in real time and, e.g., use this information to cool the ion by electronic feedback. Also, the experiment can be carried out in a linear trap with more than one ion. The heterodyne signal from, e.g., two ions can be detected separately, allowing one to measure the relative motion of the ions with a precision on the nm scale.

Interference of the ion with its mirror image was demonstrated with a visibility of more than 70%. With this experiment, it has been shown that the new lens has indeed the expected wavefront quality. Also, a strong dependence of the fringe visibility on the motion of the ion and the laser saturation is observed and theoretically described. Furthermore, by observing fringes in the fluorescence at 650 nm the influence of the mirror on the spontaneous decay, and therefore on the $P_{1/2}$ population, was demonstrated. Also, interference of the fluorescence light of one ion with fluorescence of another ion was observed with a visibility of 5%. These experiments were strongly limited by the fact that the current spherical trap does not allow one to compensate the micro-motion for more than one ion. However, the modeling of this experiment shows that it is super- and sub-radiance effects that has been observed.
In future, this problem can be overcome by using a linear trap, where a string of ions can be trapped without excess micro-motion. Also, individual addressing of the ions with the exciting laser beam provides new possibilities. Furthermore, it is possible to place a second HALO 25/0.4 lens into the front channel. With a second mirror one could form a cavity with a very tight focus and a Finesse of about 30. The Finesse is limited by the transmission of the lens, which is about 96% at 493 nm. With this setup, the spontaneous emission into the solid angle of the cavity could be enhanced by a factor of 10. By adjusting the mirrors, one can also form a cavity with two foci, one ion in the first focus and the second ion in the other focus. This experiment is similar to the super-fluorescence experiments, where two atoms are brought very close together, i.e. the distance has to be smaller than the transition wavelength. The advantage of our experiment is that while the interaction between the ions is strong, one can also address each ion individually with the exciting laser and the detector.

A Laser at 493 nm

Appl. Phys. B 67, 683–688 (1998)

Applied Physics B
Lasers
and Optics

Diode laser spectrometer at 493 nm for single trapped Ba^+ ions

C. Raab, J. Bolle, H. Oberst, J. Eschner, F. Schmidt-Kaler, R. Blatt

Institut für Experimentalphysik, Universität Innsbruck, Technikerstraße 25, A-6020 Innsbruck, Austria

Received: 12 June 1998

Abstract. A diode laser spectrometer at 493 nm is described, which is especially suited for spectroscopy of single trapped Ba^+ ions. Frequency doubling of a 100 mW diode laser at 986 nm results in up to 60 mW output power at 493 nm in a bandwidth of less than 60 kHz with respect to the cavity used for locking. Reference frequencies of 18 spectral lines of Te_2 near the 493 nm resonance of Ba^+ have been measured using modulation transfer spectroscopy. The fluorescence excitation spectrum of a single Ba^+ ion, measured with this laser, exhibits well-resolved dark resonances, which confirms the versatility of the system for quantum optical experiments.

PACS: 39.30.+w; 42.60.By; 42.80.Pj; 33.20.Kf

Single trapped ions have played a major role in the development of quantum optics since their first demonstration in 1980 [1]. In particular, they have been applied to fundamental investigations of the interaction between light and matter [2, 3], to ultrahigh precision spectroscopy, and to the development of frequency standards [4]. Present and future applications involve the generation and measurement of quantum states, in particular in the framework of quantum information and quantum computing [5], with our short-term application being the study of the ion's state by spectral analysis of its resonance fluorescence. In such experiments lasers are used to optically cool the ion and to control and measure its quantum state, i.e., the internal electronic state and the motional state of the trapped ion are manipulated with near-resonant laser light. A generic level scheme that applies to several elements typically used in single ion traps (such as Ca^+, Ba^+, and Sr^+), consists of an $S_{1/2}$, $P_{1/2}$ and a metastable $D_{3/2}$ state in lambda configuration. In this case, two lasers are necessary to continuously cool the ion and generate resonance fluorescence, one for the S–P transition and one for the D–P transition. Since reliable cooling and state preparation is a prerequisite for all the above-mentioned applications, these lasers have to be stabilized against long-term drift and their linewidths have to be reduced to a level below the typical frequencies involved, such as the Zeeman splitting (≈ 5 MHz), the vibrational frequency in the trap (≈ 1 MHz), and the width of Raman resonances which appear in the lambda level scheme (≈ 0.1 MHz) [6]. Spectral analysis of the single ion's fluorescence is also facilitated if the laser, which determines the width of the elastic component, is spectrally narrow.

The very first single-ion experiments were carried out with barium [1] because dye lasers at 493 nm (S–P) and 650 nm (P–D) were available at that time; Fig. 1 shows the relevant levels of the barium ion. Dye lasers have a large tuning range and can be stabilized well. Their disadvantages are their difficult handling and, due to the need for an ion pump laser, their high acquisition and running costs. Today, with the availability of diode lasers in many spectral regimes, more and more experiments utilize these low-cost and robust lasers. Although the first diode lasers were delicate to handle and their spectral qualities were poor, progress in the production process has made them much more reliable and has led to a vast improvement of their optical characteristics. The average lifetime of diode lasers now ranges from 10 000 h, up to several 100 000 h, which exceeds the lifetime of ion lasers by far. Their spectral purity can be improved using various optical feedback schemes as well as electronic stabilization.

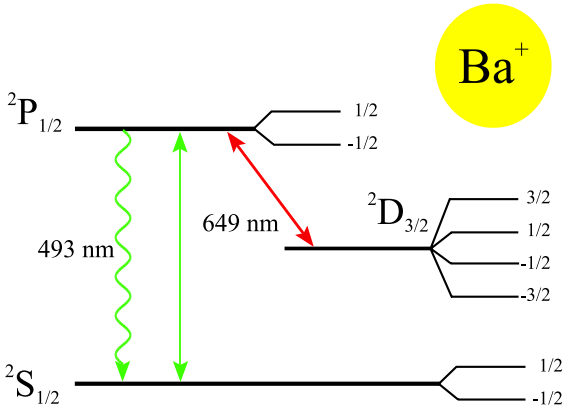

Fig. 1. Level scheme of $^{138}Ba^+$ with Zeeman level splitting schematically indicated

Currently, there are still no laser diodes commercially available with wavelengths below 600 nm. Therefore, in order to reach the spectral range down to 400 nm, one can use frequency doubling in external cavities [7–10]. In this paper we describe a diode laser system that provides powerful, tunable, and frequency-stable light at 493 nm, which is used for quantum optics and precision spectroscopy with single Ba^+ ions. Light of a 986 nm laser diode ($P_{max} = 150$ mW), which is stabilized by optical feedback from a grating, is frequency-doubled with a $KNbO_3$ crystal in an external cavity where a maximum conversion efficiency of 63% is achieved.

For a first demonstration of the spectroscopic qualities of the 493 nm laser system and in order to find stable frequency markers independent of Ba^+, we carried out Doppler-free spectroscopy on molecular tellurium at wavelengths near the S–P transition of Ba^+ (493.54 nm). To obtain a clean Doppler-free signal, we used modulation transfer spectroscopy (MTS) [11–13]. 18 Te_2 lines were found near the barium resonance in the range from 20 261.46 cm^{-1} to 20 261.87 cm^{-1}. The closest line is approximately 330 MHz above the Ba^+ transition, a frequency difference that can be easily bridged with an acousto-optical modulator (AOM).

As a first application to a single Ba^+ ion, we recorded the fluorescence excitation spectrum obtained by scanning the 493 nm laser over the S–P resonance, with another diode laser exciting the P–D transition (650 nm) at a fixed frequency. Well-resolved dark resonances are observed in the fluorescence in agreement with theoretical predictions and with earlier observations. The paper is organized as follows: In Sect. 1 the experimental setup is presented: generation of well-stabilized laser light at 986 nm and frequency doubling in a external enhancement cavity with high efficiency. In Sect. 2 modulation transfer spectroscopy of Te_2 is described and in Sect. 3 the application of this light source for quantum optical measurements on a single Ba^+ ion is demonstrated.

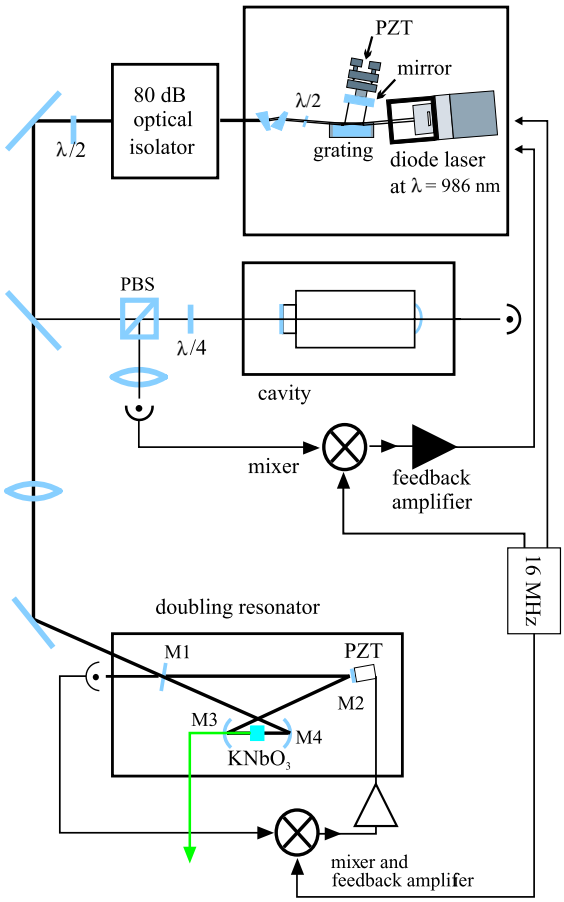

Fig. 2. Laser setup showing the IR laser, the stabilization circuit, and the frequency doubler

1 Laser system

The laser system consists of three main parts, the diode laser at 986 nm, the stabilization to a reference cavity, and the frequency doubler. The experimental setup is shown in Fig. 2. An SDL 6500 laser diode (150 mW) is temperature stabilized and driven with a commercial current source (ILX LDX-3620). The emitted light is vertically polarized and collimated into a parallel beam with an $f = 5$ mm triplet lens. To reduce the large inherent emission bandwidth and to select the lasing wavelength, we use optical feedback from a grating. We have chosen a setup in the Littman–Metcalf configuration [14], which has several advantages compared with the more commonly used Littrow scheme. These are, for example, the fixed output beam position and the adjustable feedback level. The laser beam illuminates the grating (1800 lines/mm, 30 mm long) at an angle of about 75° to obtain high wavelength selectivity and a high output coupling rate, emitting 89% into the 0th order. About 4% of the power is diffracted into the 1st order which is back reflected from a mirror into the laser diode. The laser operates in a single mode at an output power of up to 130 mW with 200 mA injection current. The emission wavelength of the laser can be adjusted between 976 nm and 990 nm by tilting the mirror. The laser frequency is fine tuned by shifting the mirror along the z axis with a high voltage applied to the piezo ceramic (PZT, see Fig. 2). Thus we obtain a continuous tuning range of 1.5 GHz. Using additional feed-forward adjustment of the injection current, the continuous tuning range increases to 3 GHz. The polarization of the output light is rotated 90° with a half-wave plate to avoid losses at the anamorphic prism pair, which is used to circularize the beam. Unwanted feedback into the diode laser from the rest of the experimental setup is prevented with two Faraday isolators of 40 dB isolation each.

The laser is actively locked to a reference cavity using a Pound–Drever–Hall stabilization scheme [15]. The cavity has a finesse of 1200 and a free spectral range of 1.2 GHz, its drift rate is about 0.5 MHz/min. FM sidebands of about 10^{-4} of the laser power are generated by modulating the laser diode injection current at 16 MHz. A small part ($\approx 2\%$) of the laser light is coupled into the reference cavity, and the reflected light is separated, using a quarter-wave plate and a polarizing beam splitter, and detected with a fast photodiode. The photo current is mixed with the 16-MHz reference to produce an error signal, which is amplified with a PID amplifier and fed back to the diode current and the piezo-mounted Littman mir-

ror. We achieve a short-term ($\tau < 1$ s) laser linewidth below 30 kHz rms with respect to the reference cavity. For scanning, the frequency of the locked laser is varied by tuning the reference cavity with a piezo.

Frequency doubling of the diode laser light is achieved with a $KNbO_3$ crystal, which is placed inside an enhancement cavity for the 986 nm light. This ring cavity consists of two plane mirrors and two curved mirrors of 38 mm radius. Three mirrors (M2, M3, M4) have high reflectivity at 986 nm, $R > 99.9\%$, and they transmit about 95% at 493 nm. The input coupler (M1) is chosen to have a reflectivity of $R = 97\%$, which leads to an impedance matching of better than 80% at optimum doubling efficiency. The resonator length is 395 mm and the distance between the curved mirrors is 82 mm. Mirror M2 is mounted on a PZT to tune the resonator length. The 5 mm B-cut $KNbO_3$ crystal is placed between the curved mirrors and the cavity is designed for an optimum focus inside the crystal [16]. The 986 nm laser light is mode matched, with a single lens, into the doubling cavity. We achieve 90% mode matching efficiency into TEM_{00}. The doubling cavity is locked, also with a Pound–Drever–Hall feedback circuit, to the frequency of the IR laser using the 16-MHz sidebands on the 986 nm light. The error signal is fed back to the piezo-mounted mirror M2. This mirror has a diameter 6.75 mm and 3 mm thickness. In combination with a fast piezo we obtain a servo-loop bandwidth of about 40 kHz. Together with a 12 dB/octave integrator this leads to an intensity stability of the frequency-doubled light of better than 2×10^{-3} under normal laboratory background noise conditions.

At a diode current of 200 mA we obtain 94 mW light at 986 nm in front of the doubler and up to 60 mW of green light out of the doubling cavity. This corresponds to 63% conversion efficiency of the frequency doubler. The overall efficiency, i.e. the ratio of the electrical power injected into the diode to the output power of the green light amounts to 16%.

2 Spectroscopy on Te_2

The experimental setup for spectroscopy of Te_2 is shown in Fig. 3. We use modulation transfer spectroscopy (MTS), a Doppler-free method that detects a rf modulation of a probe beam which is generated in the Te_2 vapor via four-wave-mixing with a counter-propagating, rf-modulated pump beam [11, 13, 17–19]. The advantage of this technique in comparison to frequency modulation spectroscopy (FMS) [20–22] is that the Doppler-free spectra appear without a background slope and therefore, the resulting signals can be used for locking a diode laser directly to the molecular resonance without the need for offset compensation. The laser light is divided into the pump and the probe beam with a polarizing beam splitter. The splitting ratio is adjusted with a half-wave plate to optimize the signal-to-noise ratio. The pump beam is frequency-modulated with a $LiTaO_3$ electro-optical modulator (EOM) driven at 6 MHz frequency. The EOM is heated to about 100 °C to avoid optical damage of the crystal. As shown in Fig. 3, the pump and the probe beam counter-propagate with orthogonal polarizations through the Te_2 cell, which is heated to about 420 °C. The beams are focused with $f = 200$ mm lenses to increase the intensity inside the cell and the probe beam is detected with a fast photodiode whose output is amplified and mixed with the 6 MHz reference using a double-balanced mixer. The phase of the local oscillator can be shifted over a range of 360°, and the MTS signal is recorded with a Tektronix TDS784 oscilloscope.

We have scanned the spectral range from 20 261.46 cm^{-1} to 20 261.87 cm^{-1} in several intervals of ≈ 2.5 GHz with the laser locked to the reference cavity. Neighboring scans overlap and were taken with at least one common Te_2 resonance. In order to obtain a frequency scale, a small part of the green light was coupled into a Fabry–Pérot resonator (FP2) with a free spectral range of 725.6(1) MHz.

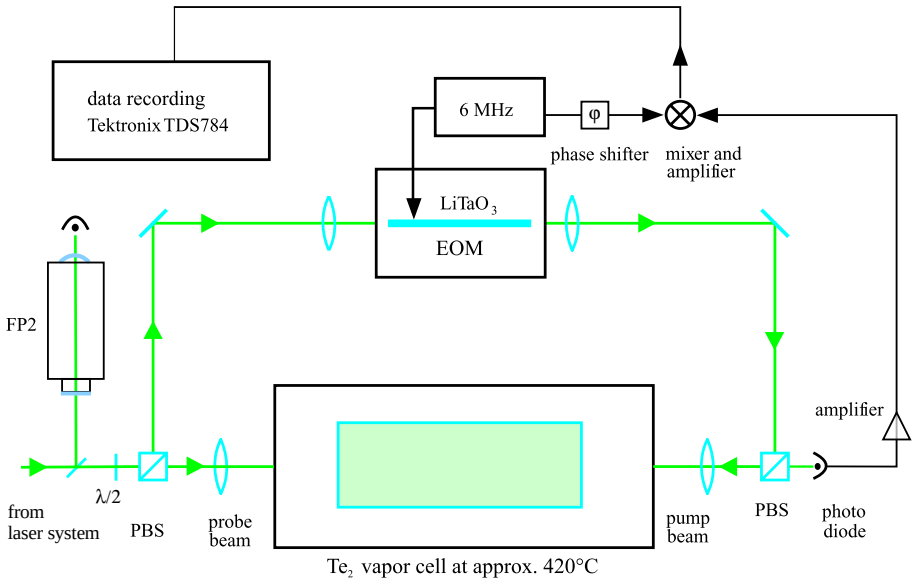

Fig. 3. Schematic setup for modulation transfer spectroscopy of Te_2

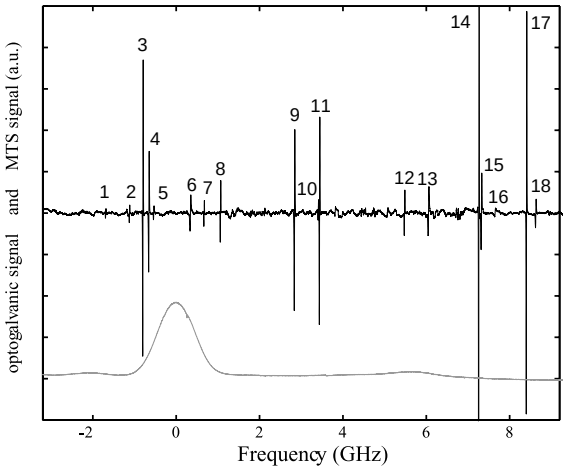

Fig. 4. *Upper curve*: Te_2 spectrum from 20 261.46 cm^{-1} to 20 261.87 cm^{-1}. *Lower curve*: Ba^+ optogalvanic spectrum

The frequency axis has been calibrated from the measured cavity resonances with 1% relative accuracy, limited by the nonlinearity of the scanning piezo and the drift of the cavity. The absolute wavelengths were determined with a wavemeter and by means of optogalvanic spectroscopy of Ba^+ which has been carried out simultaneously. The measured spectra are shown in Fig. 4. From a Gaussian fit to the measured Ba^+ spectrum the center of the S–P resonance at 493 nm was determined with an accuracy of 26 MHz. The literature value of this resonance frequency, 20 261.562 cm^{-1} [23], was taken as the absolute frequency reference. In the covered frequency range of 12.7 GHz, 18 tellurium resonances were resolved. Their positions and relative amplitudes are listed in Table 1. By comparison with the Tellurium Atlas of Cariou and Luc [24], two of their lines, No. 3435 (20 261.5342 cm^{-1}) and No. 3436 (20 261.8012 cm^{-1}), were identified as our No. 3 and 14. The measured distance of 8.06(8) GHz between these two lines is in good agreement with the listed separation of 0.2670 cm^{-1}. The smallest frequency distance between one of the Te_2 lines (line No. 6 in Table 1) and the Ba^+ resonance is 330 MHz. For further investigation we concentrated on the strong line No. 3435 (No. 14 in Table 1). Scanning 100 MHz about this line was used to resolve the MTS line shape and compare it to the theoretically expected shapes [18, 25]. For a calculation of the latter, and for low modulation index as in our experiment, only the first sideband has to be taken into account and the line shape of the demodulated signal is given by:

$$S(\Delta) = \mathrm{Re}\left[\sum_{j=a,b} \frac{\mu_{ab}^2}{\gamma_j + \mathrm{i}\delta}\left(\frac{1}{\gamma_{ab} + \mathrm{i}(\Delta + \delta/2)} - \frac{1}{\gamma_{ab} + \mathrm{i}(\Delta + \delta)} + \frac{1}{\gamma_{ab} - \mathrm{i}(\Delta - \delta)} - \frac{1}{\gamma_{ab} - \mathrm{i}(\Delta - \delta/2)}\right)\mathrm{e}^{-\mathrm{i}\vartheta}\right] . \quad (1)$$

Here, a and b denote the lower and the upper level of the Te_2 transition, respectively, μ_{ab} is the electric dipole moment, $\Delta = \omega_{\mathrm{laser}} - \omega_{ab}$ is the detuning of the laser, $\gamma_{a.b}$ are the decay rates of the two levels, γ_{ab} is the optical relaxation rate from a to b, δ is the modulation frequency, and ϑ is the demodulation phase. The measured data have been fitted with this line shape. Figure 5 shows the data and the fit for phases 95° and 180°. The fitting parameters are γ_{ab}, ϑ, a scaling factor proportional to $\sum_{j=a,b} \mu_{ab}^2/(\gamma_j + \mathrm{i}\delta)$ and the frequency offset. The fitting procedure yields a linewidth of the measured line of $\gamma_{ab} = 3.9(2)$ MHz. The asymmetry in the experimental data is attributed to a residual amplitude modulation in the EOM.

3 Spectroscopy of a single Ba^+ ion

For spectroscopy of single trapped Ba^+ ions, an additional laser at 650 nm is required to excite the D–P transition. The setup of this laser uses a SDL 7511 laser diode and is otherwise very similar to the setup of the infrared diode laser. The ion is stored in a miniature Paul trap and localized to

Table 1. Positions and relative amplitudes of lines in the Te_2 spectrum. The amplitude has been defined by the difference between the maximum and the minimum signal at 90° demodulation phase. Lines No. 3 and 14 have been previously published in [24]. The errors in frequency are the relative errors of the scaling, the errors in wave number are absolute errors

Line number	Relative frequency /GHz	Wave number /cm^{-1}	Relative amplitude
1	−1.70(1)	20261.505(1)	0.8
2	−1.13(1)	20261.524(1)	1.4
3	−0.808(8)	20261.535(1)	23.9
4	−0.666(6)	20261.540(1)	9.7
5	−0.549(5)	20261.544(1)	1.1
6	0.330(3)	20261.573(1)	2.9
7	0.658(6)	20261.584(1)	2.1
8	1.05(1)	20261.597(1)	5.0
9	2.83(2)	20261.656(2)	14.6
10	3.40(3)	20261.675(2)	1.6
11	4.01(4)	20261.696(2)	16.7
12	5.47(4)	20261.744(3)	3.7
13	6.05(6)	20261.764(3)	3.9
14	7.25(7)	20261.804(3)	78.0
15	7.31(7)	20261.806(3)	5.5
16	7.64(7)	20261.817(3)	0.7
17	8.39(8)	20261.842(4)	32.4
18	8.61(8)	20261.850(4)	2.3

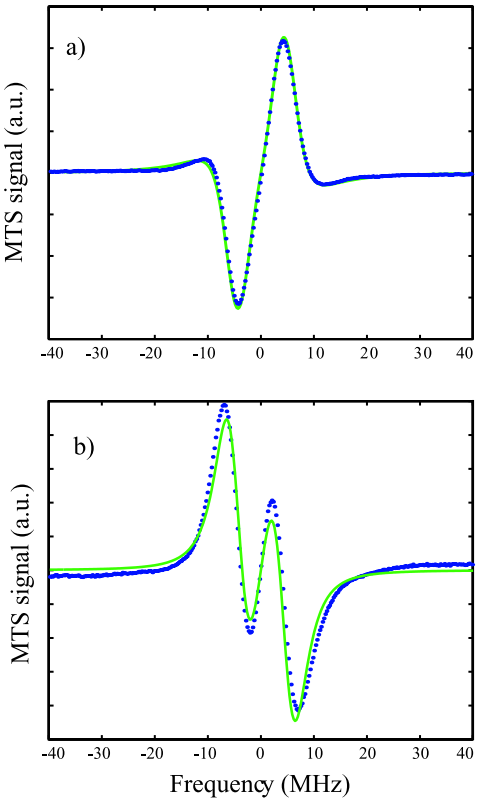

Fig. 5. Line No. 3435 with high resolution (*points*) and calculated MTS line shape (*solid line*)

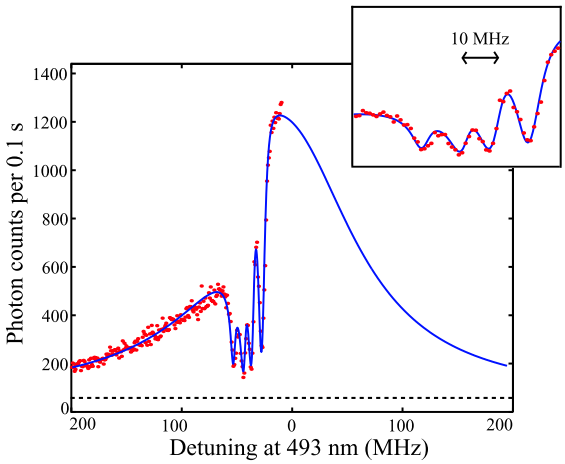

Fig. 6. Fluorescence excitation spectrum of a single trapped Ba^+ ion, experimental data (*points*) and calculated fit (*line*). The *dashed line* indicates the constant background count rate. The *insert* shows the four dark resonances magnified, with background subtracted

better than a few μm. The light from the two lasers is combined using a dichroic mirror and focused into the trap with an $f = 250$ mm lens resulting in a diameter of the focus in the trap center of ≈ 80 μm. The light level is adjusted using a half-wave plate and a polarizer. Three orthogonal pairs of Helmholtz coils are employed to produce a well-defined magnetic field that is oriented perpendicular to the direction of light polarization. Fluorescence from the ion is collected with an $f/0.7$ quartz collimator, imaged onto a cooled photomultiplier, and recorded in photon-counting mode for 0.1 s per data point. For continuous excitation of fluorescence, the laser at 493 nm has to be tuned below the S–P resonance to maintain optical cooling of the ion [26–28]. Figure 6 shows a scan of the laser at 493 nm across the Ba^+ resonance in steps of ≈ 100 kHz while the laser at 650 nm is kept at a fixed frequency below the D–P resonance. The power of the green light was set to 25 μW, the red power is 9 μW. The frequency axis is calibrated with the help of an optogalvanic signal from a barium hollow cathode lamp, which is recorded simultaneously with the Ba^+ fluorescence. Four dark resonances are resolved in the fluorescence signal. These occur when the detuning for an S–D Raman transition between one of the Zeeman sublevels becomes zero [6]. The solid line in Fig. 6 indicates a fitted curve to the measured data calculated from 8-level Bloch equations taking into account the Zeeman substructure of the S, P, and D levels, the light polarization, and magnetic field [29]. The complex spectral shape is well reproduced in the calculation. In particular, the measured and calculated widths and depths of the dark resonances, which are determined by the laser intensities and linewidths, respectively, agree well. Experimental parameters determined from the fit are the green and red light intensity, the exact detuning of the red laser, the magnetic field, the angle between magnetic field and light polarization, and the common linewidth of both lasers. The intensities are $380(50)\,\mathrm{mW/cm^2}$ at 493 nm and $140(20)\,\mathrm{mW/cm^2}$ at 650 nm. The magnetic field is $5.8(3) \times 10^{-4}$ Tesla, the angle is $88\,(7)^\circ$, the detuning of the red laser is $-40.6(7)$ MHz, and the common linewidth of both lasers is 89(35) kHz. If we assume that both lasers have the same width, the linewidth of the laser at 493 nm is 63 kHz, which agrees well with the value measured from the error signal.

4 Conclusion

We have set up a powerful, frequency-stable and reliable laser system for spectroscopy of single Ba^+ ions. We obtain a maximum output power of 60 mW of light at 493 nm in a bandwidth of 60 kHz rms. Doppler-free modulation transfer spectroscopy was carried out on molecular tellurium and 18 lines were found in a spectral region of 8 GHz around the Ba^+ $S_{1/2} - P_{1/2}$ transition. The MTS signal agrees well with theory. In order to eliminate the cavity drift in the laser stabilization circuit, the laser will be actively locked to the Te_2 line, which is 330 MHz above the Ba^+ S–P transition, and the laser frequency will be scanned with an acousto-optical modulator. We have applied the laser to excite resonance fluorescence from a single Ba^+ ion in a Paul trap. Well-resolved dark resonances and a spectral line shape that agrees well with the theory confirm the versatility of the laser system for quantum optical measurements.

Acknowledgements. This work is supported by the Fonds zur Förderung der wissenschaftlichen Forschung (FWF) under contract number P11467-PHY and in parts by the TMR network "Quantum Structures" (ERB-FMRX-CT96-0077).

References

1. W. Neuhauser, M. Hohenstatt, P.E. Toschek, H.G. Dehmelt: Phys. Rev. A **22**, 1137 (1980)
2. D.M. Meekhof, C. Monroe, B.E. King, W.M. Itano, D.J. Wineland: Phys. Rev. Lett. **76**, 1796 (1996)
3. C. Monroe, D.M. Meekhof, B.E. King, D.J. Wineland: Science **272**, 1131 (1996)
4. R. Blatt: In Atomic Physics **14**, p. 219, ed. by D.J. Wineland, C.E. Wieman, S.J. Smith (AIP, New York 1995)
5. J.I. Cirac, P. Zoller: Phys. Rev. Lett. **74**, 4091 (1995)
6. I. Siemers, M. Schubert, R. Blatt, W. Neuhauser, P.E. Toschek: Europhys. Lett. **18**, 139 (1992)
7. P. Lodahl, J.L. Sørensen, E.S. Polzik: Appl. Phys. B **64**, 383 (1997)
8. W.J. Kozlovsky, W. Lenth, E.E. Latta, A. Moser, G.L. Bona: Appl. Phys. Lett. **56**, 2291 (1990)
9. A.S. Zibrov, R.W. Fox, R. Ellingsen, C.S. Weimer, V.L. Velichansky, G.M. Tino, L. Hollberg: Appl. Phys. B **59**, 327 (1994)
10. C. Zimmermann, V. Vuletic, A. Hemmerich, T.W. Hänsch: Appl. Phys. Lett. **66**, 2318 (1995)
11. L.S. Ma, Ph. Courteille, G. Ritter, W. Neuhauser, R. Blatt: Appl. Phys. B **57**, 159 (1993)
12. J.L. Hall, R. Felder, L.S. Ma: Conference on Precision Electromagnetic Measurements, Paris (1992) p. 160
13. J.J. Snyder, R.K. Kaj, D. Bloch, M. Ducloy: Opt. Lett. **5**, 163 (1980)
14. K.C. Harvey, C.J. Myatt: Opt. Lett. **16**, 910 (1991)
15. R.W.P. Drever, J.L. Hall, F.V. Kowalski, J. Hough, G.M. Ford, A.J. Munley, H. Ward: Appl. Phys. B **31**, 97 (1983)
16. G.D. Boyd, D.A. Kleinman: J. Appl. Phys. **39**, 3597 (1968)
17. R.K. Kaj, D. Bloch, J.J. Snyder, G. Camy, M. Ducloy: Phys. Rev. Lett. **44**, 1251 (1980)
18. G. Camy, D. Bloch: J. Phys. **43**, 57 (1982)
19. A. Schenzle, R.G. DeVoe, R.G. Brewer: Phys. Rev. A **25**, 2606 (1982)
20. M.D. Levenson, G.L. Eesley: Appl. Phys. **19**, 1 (1979)
21. G.C. Bjorklund: Opt. Lett. **5**, 15 (1980)
22. J.L. Hall, L. Hollberg, T. Baer, H.G. Robinson: Appl. Phys. Lett. **39**, 680 (1981)
23. Ch. Moore: Atomic Energy Levels, Volume III, NIST (1971)
24. J. Cariou, P. Luc: *Atlas du Spectre d'Absorption de la molécule de Tellure*, Laboratoire Aimé–Cotton, CNRS II, Orsay, France (1980)
25. L.S. Ma, L.E. Ding, Z.Y. Bi: Appl. Phys. B **51**, 233 (1990)
26. W. Neuhauser, M. Hohenstatt, P.E. Toschek, H.G. Dehmelt: Phys. Rev. Lett. **41**, 233 (1978)
27. D.J. Wineland, R.E. Drullinger, F.L. Walls: Phys. Rev. Lett. **40**, 1639 (1978)
28. D. Reiß, A. Lindner, R. Blatt: Phys. Rev. A **54**, 5133 (1996)
29. M. Schubert, I. Siemers, R. Blatt, W. Neuhauser, P.E. Toschek: Phys. Rev. A **52**, 2994 (1995)

B Motional sidebands in the fluorescence spectrum

Motional Sidebands and Direct Measurement of the Cooling Rate in the Resonance Fluorescence of a Single Trapped Ion

Ch. Raab, J. Eschner, J. Bolle, H. Oberst, F. Schmidt-Kaler, and R. Blatt

Institut für Experimentalphysik, Universität Innsbruck, Technikerstraße 25, A-6020 Innsbruck, Austria

(Received 20 March 2000)

Resonance fluorescence of a single trapped ion is spectrally analyzed using a heterodyne technique. Motional sidebands due to the oscillation of the ion in the harmonic trap potential are observed in the fluorescence spectrum. From the width of the sidebands the cooling rate is obtained and found to be in agreement with the theoretical prediction.

PACS numbers: 32.80.Pj, 42.50.Lc, 42.50.Vk

Since the first preparation of a single atom in a Paul trap and observation of its resonance fluorescence [1], investigation of this light has revealed a range of unique properties. Examples are its nonclassical nature [2] and the highly nonlinear response, in the form of sudden intensity jumps, of a multilevel atom to continuous laser excitation [3]. The fluorescence is, at the same time, a unique tool for determining the state of the atom. This is particularly obvious for a single particle where each photon emission marks the respective projection of the atomic wave function into the final state of the corresponding transition. It is also of great interest to study, through its resonance fluorescence, the motion of a single laser-excited particle, e.g., for investigating laser cooling schemes or in connection with proposals for quantum state manipulation or quantum information processing with trapped particles [4].

The spectrum of fluorescence of a motionless two-level atom exhibits an elastic part (Rayleigh peak) which is δ correlated with the exciting light, and an inelastic contribution, the Mollow triplet [5]. While the latter marks spontaneous transitions between the dressed states of the combined atom-light quantum system and appears when the light intensity approaches saturation, the elastic contribution dominates for light levels below saturation. For a free atom this spectrum is modified by the recoil shift. For a trapped atom the elastic peak is unshifted, and sidebands appear at the characteristic frequencies of the motion in the trap [6–8], with sizes that depend on the amplitude of this motion. The spectral width of these sidebands reflects the effective decay of the motional states of an atom in the trap, i.e., the rate of transitions which change this state. In particular, if laser excitation provides optical cooling of the trapped atom, the sideband width reflects the equilibrium of heating and cooling transitions in the steady state. While such sidebands have been observed in the fluorescence spectrum of ensembles of trapped neutral atoms [9], their investigation for a single particle and analysis of their width has not been done so far [10]. The measurement of cooling rates is highly interesting in experiments with cold atoms or ions, in particular when many levels or several light fields are involved such that an optimal set of parameters is hard to find solely from theoretical arguments.

In this paper we report on a measurement of the resonance fluorescence of a single trapped barium ion which reveals sidebands of the elastically scattered light due to the various components of the ion's motion in the trapping potential. From the width of the sidebands which correspond to one of its vibrational modes in the Paul trap quasipotential we deduce the cooling rate induced by the exciting laser. This method will enable us to perform detailed studies of motional effects of laser radiation *in situ,* i.e., during the laser excitation without further analysis tools.

In the experiment, a single Ba^+ ion is trapped in a 1.4 mm diameter Paul trap. The ion is generated by impact ionization of a weak thermal Ba atomic beam with an electron beam inside the trap. The trap is suspended in UHV and driven with a 500 V_{pp} radio frequency signal at $f_{\mathrm{Paul}} \approx 19$ MHz. The ion is laser cooled by simultaneous excitation on its $S_{1/2} \leftrightarrow P_{1/2}$ and $P_{1/2} \leftrightarrow D_{3/2}$ resonance lines at 493.4 and 649.7 nm, respectively [11]. See Fig. 1 for the relevant levels of Ba^+. The 493 nm light is produced by a frequency doubled diode laser

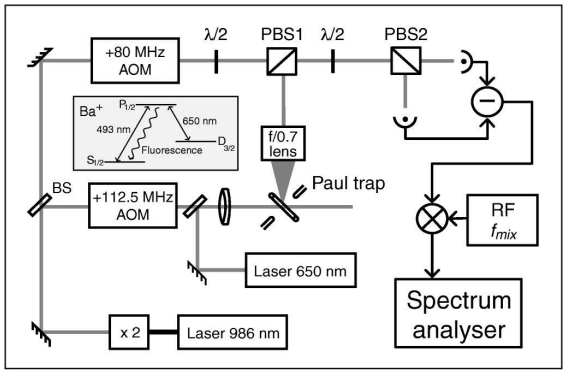

FIG. 1. Experimental setup. The inset shows the relevant levels and transition wavelengths of Ba^+. Resonance fluorescence at 493 nm is investigated. AOM stands for acousto-optic modulator, BS for beam splitter, PBS for polarizing beam splitter, and $\times 2$ for frequency doubling. f_{mix} is varied to observe the various spectral components of the fluorescence.

 0031-9007/00/85(3)/538(4)$15.00

with external grating resonator described in Ref. [12]. This laser is frequency stabilized to a Te_2 resonance line 666 MHz away from the Ba^+ line, by modulation transfer spectroscopy [13]. The 650 nm light is generated by a diode laser with an external grating resonator, stabilized to an optical resonator. Both lasers have linewidths well below 100 kHz. The laser beams are combined on a dichroic beam splitter before they are focused into the trap, and both light fields are linearly polarized. The laser intensities at the position of the ion are in the range of 200 mW/cm^2 (493 nm) and 100 mW/cm^2 (650 nm). The 650 nm laser is close to resonance; the 493 nm laser is red detuned by about the transition linewidth ($\Gamma = 15.1$ MHz) for Doppler cooling. A 2.8 G magnetic field which is orthogonal to both the laser wave vector and the laser polarization defines a quantization axis and lifts the degeneracy of the Zeeman sublevels. The precise parameters are determined by fitting an eight-level Bloch equation calculation to a scan of the fluorescence intensity vs the detuning of the 650 nm laser [14].

The 493 nm resonance fluorescence of the ion is analyzed with a heterodyne detection setup shown in Fig. 1 [15]. Using a slightly simpler scheme, with a frequency shift in only one arm of the heterodyne setup and with a frequency selective photodetector, Höffges *et al.* [16] have observed the elastic part of an ion's resonance fluorescence, but no motional sidebands. In our setup, the fluorescence at right angle to the direction of the laser beams, in the direction of the magnetic field, is collimated with an $f/0.7$ lens. This light consists of the two σ-polarized components corresponding to the $P_{1/2}(m = \pm 1/2)$ to $S_{1/2}(m = \mp 1/2)$ transitions, and its elastic part is linearly polarized, because the two σ-polarized components are coherently superimposed. For creating a local oscillator beam, the green laser light is divided into two beams which are frequency shifted by 112.5 MHz (beam 1) and 80 MHz (beam 2) using acousto-optical modulators (AOMs). Beam 1 excites the ion while beam 2 is superimposed with the collimated fluorescence on a polarizing beam splitter PBS1. The beam sizes of the collimated fluorescence and the local oscillator (beam 2) are adjusted for optimum overlap, using telescopes. Their orthogonal polarizations after PBS1 are mixed with a $\lambda/2$ plate and a second polarizing beam splitter PBS2 to create an interference signal. The two output signals of PBS2 are detected on two fast photodiodes (50 MHz bandwidth, 80% quantum efficiency). By subtracting their photodiode currents, the interference term $S \propto E_{\mathrm{lo}} E_{\mathrm{fluor}}$ between the fluorescence and the local oscillator is filtered out. Because of the frequency shifts in beams 1 and 2, this interference product (i.e., its elastic part) is expected at a frequency of 32.5 MHz, the difference frequency of the two AOM drives, while any motional sideband due to an oscillatory motion with frequency f_s would appear at 32.5 MHz $\pm n f_s, n = 1, 2, \ldots$. The reason for using two AOMs is that their difference frequency is not generated elsewhere in the setup, such that no electrical cross talk perturbs the final signal; neither can any residual amplitude modulation in one of the beams create a 32.5 MHz signal on the photodiodes. The interference signal S is mixed with an rf reference signal at variable frequency f_{mix} around 32.5 MHz, low-pass filtered, and finally analyzed on a fast Fourier transform (FFT) spectrum analyzer with 100 kHz maximum bandwidth. All rf sources, i.e., the trap drive, the AOM supplies, and the rf reference, are phase locked to the same 10 MHz master oscillator.

With the mixer frequency f_{mix} set to $f_0 = 32.45$ MHz, the elastically scattered light produces a signal at 50 kHz on the spectrum analyzer. Such a signal, with the resolution bandwidth set to 61 mHz, is shown in Fig. 2. Clearly, only one data point is significantly above the background noise, thus verifying the δ correlation between exciting laser and fluorescence. The signal-to-noise ratio (SNR) is 17 dB (at unit bandwidth). The maximum SNR which can be achieved depends on the rate N of fluorescence photons that are detected. It is derived in the following way: The spectral power of the signal S is $P_S \propto S^2/\Delta\nu$, where $\Delta\nu$ is the detection bandwidth (or signal bandwidth, whichever dominates), while the noise power is $P_N \propto E_{\mathrm{lo}}^2$, such that their ratio is $\mathrm{SNR}_{\mathrm{max}} = E_{\mathrm{fluor}}^2/\Delta\nu = N/\Delta\nu$. For this to hold, the noise created by E_{lo} with no fluorescence present [17] has to be the dominant noise in the photodiode signal S. By varying the local oscillator power without a fluorescence signal, we confirmed that this is the case in our experiment and that the noise is close to the quantum limit. With a typical scattering rate of $(2.5–5) \times 10^4$ photons/s into the solid angle that is collimated, and with 80% photodiode quantum efficiency, the maximum possible SNR turns out to be 35–40 dB. The comparatively low value of 17 dB which we find is due to phase front distortions induced by the collimating lens and a resulting low degree of mode matching between the collimated fluorescence and the local oscillator.

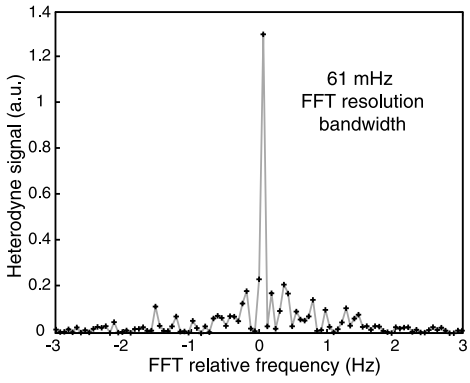

FIG. 2. FFT spectrum analyzer signal around 50 kHz showing bandwidth-limited heterodyne detection of the elastic (carrier) peak of the resonance fluorescence.

Because of the quadrupole radiofrequency field in a Paul trap, the ion undergoes a driven oscillation at the frequency $f_{\mathrm{Paul}} = 18.53$ MHz. This so-called micromotion is in phase with the driving field, and its amplitude is proportional to the ion's distance from the trap center. The sidebands to the elastic peak which this oscillation generates can be observed on the spectrum analyzer, in the same manner as the carrier, by setting f_{mix} to $f_0 \pm nf_{\mathrm{Paul}}$, $n = 1, 2, \ldots$. In Fig. 3 we show the results of such measurements. Because of the fact that the phase of the micromotion is well defined, and because all rf sources are phase locked, the width of the micromotion sidebands is limited by the resolution bandwidth of the spectrum analyzer, just like the width of the elastic peak in Fig. 2.

The sizes of the micromotion sidebands are expected to be proportional to $|J_n(m)|^2$ where J is a Bessel function, $n = 0, \pm 1, \pm 2, \ldots$, is the number of the sideband, and m is the modulation index corresponding to the ion's oscillation. With the micromotion described by $\vec{a} \sin\Omega t$, ($\Omega = 2\pi f_{\mathrm{Paul}}$) and with $\vec{k}_l$ and $\vec{k}_d$ describing the laser and fluorescence wave vectors, respectively, m is given by $m = \vec{a} \cdot (\vec{k}_d - \vec{k}_l)$ [16]. The particular value of m found from the sidebands in Fig. 3 is 0.47. This corresponds to a micromotion amplitude in the direction of $\vec{k}_l - \vec{k}_d$ of about 26 nm. By minimizing the micromotion, i.e., the value of m, with the aid of such a measurement, the ion can be placed in the trap center where the trapping conditions are optimal [18]. At optimum conditions, i.e., if the SNR reaches 40 dB, and $\vec{a} \parallel \vec{k}_d - \vec{k}_l$, this measurement is sensitive to micromotion amplitudes of about 1 nm.

Apart from the forced micromotion oscillation, the three-dimensional trapping in the rf-generated pseudopotential of a Paul trap results in three independent modes of free vibration along orthogonal axes at three (in general different) frequencies f_{macro}. In our case, these frequencies are 620.5, 670, and 1301 kHz. Investigation of this so-called macromotion is our main purpose, because these motional degrees of freedom interact with the laser in a cooling process, and the corresponding sidebands contain information about the motional state of the ion, the efficiency of the cooling, and their dependences on the laser parameters. It is also the macromotion which is used in experiments on quantum state manipulation and entanglement, in particular in the framework of quantum information and quantum computation [19].

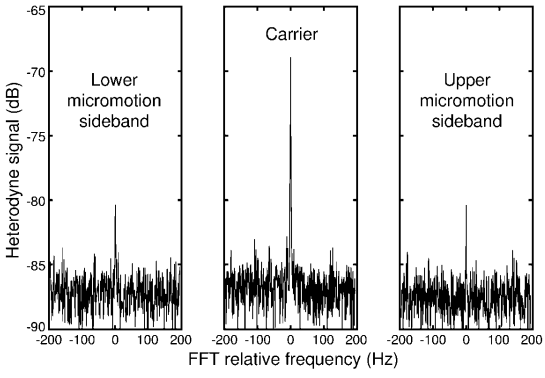

FIG. 3. Heterodyne signal showing the elastic peak (center) and the $n = \pm 1$ micromotion sidebands (right, left). For recording the sidebands the FFT analyzer frequency is shifted by $\pm f_{\mathrm{Paul}} = \pm 18.53$ MHz. The FFT resolution bandwidth was set to 1 Hz. Note the logarithmic ordinate scale.

The macromotion is harder to detect in the heterodyne signal than the micromotion because it is not correlated with any applied rf source. In view of the noise considerations above, detection of a macromotion sideband requires that the rate of photons which contribute to the sideband heterodyne signal is larger than the spectral width of that sideband. Because of the inefficient mode matching described above, this situation is not realized in our present setup. However, the macromotion corresponds to a damped harmonic oscillator (laser cooling being the damping mechanism) which can be driven with an additional external field at some frequency f_{drive} close to the macromotion frequency f_{macro}. Then, with f_{mix} set to $f_0 \pm nf_{\mathrm{drive}}$, the excited macromotion is detectable as a δ signal on the spectrum analyzer, and a scan of f_{drive} over one of the macromotion resonances reveals the response of that oscillator mode to the drive, in particular the broadening of the resonance due to laser cooling. The result of such a measurement is shown in Fig. 4. Here, the upper trace corresponds to the height of the elastic peak ($f_{\mathrm{mix}} = f_0$) as in Fig. 2, while the lower trace corresponds to the height of the sideband at f_{drive} ($f_{\mathrm{mix}} = f_0 + f_{\mathrm{drive}}$), both as functions of f_{drive} around the 620.5 kHz macromotion mode frequency. The driving voltage was applied to an electrode about 1 mm away from the ion; its power was -60 dB m. The axis of the excited vibrational mode is at 45° between the direction of the laser and the observation, as was found from the image of the ion at much higher drive power.

Figure 4 shows how the elastic scattering decreases while the sideband scattering increases around the macromotion resonance. The two traces were fitted with functions $|A_n J_n(m(f_{\mathrm{drive}}))|^2, n = 0$ for the carrier, $n = 1$ for the sideband, where $m(f_{\mathrm{drive}})$ was assumed as

$$m(f_{\mathrm{drive}}) = \frac{m_{\max}}{1 + (\frac{f_{\mathrm{drive}} - f_{\mathrm{macro}}}{\Delta f/2})^2}, \qquad (1)$$

as expected for a damped harmonic oscillator. We find a maximum modulation index $m_{\max} = 1.5$ and a width of the macromotion resonance $\Delta f = 750$ Hz. This width corresponds to the effective linewidth that the ion's oscillator eigenstates in the trap acquire due to the ongoing laser excitation which makes the ion change its motional state [7,8,16].

To compare this cooling rate with the one derived from a simple model, we describe the motion of the ion by a driven and damped harmonic oscillator. Some limiting conditions are fulfilled in our experiment: The cooling

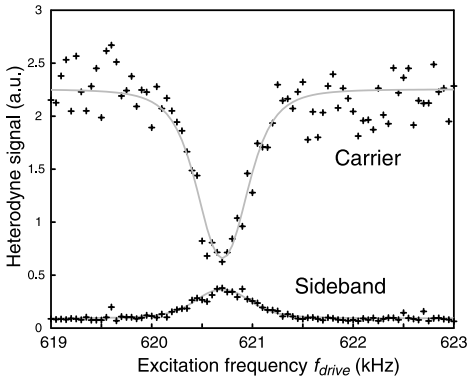

FIG. 4. Heterodyne signal showing the sizes of the elastic peak (upper trace) and the sideband of the weakly excited macromotion (lower trace) as functions of the excitation frequency f_{drive}. For the elastic peak the FFT analyzer frequency is kept fixed while for the sideband it is shifted by f_{drive}. The bandwidth is 1 Hz.

rate is much smaller than the linewidth of the transition Γ, i.e., the velocity changes only negligibly during one lifetime, and both the recoil frequency $\hbar k^2/2M = 2\pi \times 5.9$ kHz, M being the ion mass, and the maximum Doppler shift $k v_{\max}$ are smaller than the oscillation frequency (the latter being the Lamb-Dicke condition). Therefore we can calculate the cooling rate, i.e., the damping coefficient, from the radiation pressure that acts on the ion during its oscillation [20],

$$F(v) = \hbar k \Gamma P_P(\Delta - kv), \tag{2}$$

where P_P is the probability of finding the ion in the $P_{1/2}$ state and Δ is the detuning of the 493 nm laser from the atomic resonance frequency. With Δ negative and of the order of Γ, and for $kv \ll \Gamma, |\Delta|$ the velocity-dependent part of $F(v)$ amounts, in first order, to a friction force $F_f = -\alpha M v$ that the ion experiences [20], and

$$\alpha = 2\frac{\hbar k^2}{2M}\Gamma\frac{dP_P}{d\Delta} \tag{3}$$

corresponds to the linewidth induced by the laser cooling. All parameters in Eq. (3) refer to the 493 nm laser. We can neglect the contribution of the 650 nm laser to the cooling because this laser is set to yield maximum fluorescence ($\Delta_{650} = 2\pi \times 5$ MHz), such that $dP_P/d\Delta_{650} \approx 0$. By calculating $dP_P/d\Delta$ from the same eight-level Bloch equations that determine our experimental parameters [14] $\Delta_{493} = -2\pi \times 19$ MHz, $I_{493} = 189$ mW/cm^2, $I_{650} = 107$ mW/cm^2, we get $\alpha = 2\pi \times 640$ Hz which agrees well with the measurement.

In conclusion, the spectrum of resonance fluorescence from a single harmonically confined ion in a Paul trap was observed using heterodyne detection. Aside from the elastic peak, the spectrum exhibits sidebands due to the weakly excited macromotion of the ion in the trap. Investigation of these sidebands allows for an analysis of the cooling rate, without affecting the motional state of the ion by, e.g., probing pulses. The measured cooling rate in our experiment compares well with a simple model calculation. Moreover, micromotion sidebands are observed which, by minimizing their amplitude, can be used to actively compensate for residual micromotion down to the nm level. These techniques will prove useful in the context of precision spectroscopy with ion traps and, in particular, for the preparation and manipulation of vibrational quantum states of motion as they are required for quantum information experiments with trapped ions.

We acknowledge support by the Fonds zur Förderung der wissenschaftlichen Forschung (FWF) (Project No. P11467-PHY) and by the EC (TMR network "Quantum Structures," ERB-FMRX-CT96-0077).

[1] W. Neuhauser *et al.,* Phys. Rev. A **22**, 1137 (1980).
[2] F. Diedrich and H. Walther, Phys. Rev. Lett. **58**, 203 (1987); M. Schubert *et al.,* Phys. Rev. Lett. **68**, 3016 (1992).
[3] W. Nagourney *et al.,* Phys. Rev. Lett. **56**, 2797 (1986); Th. Sauter *et al.,* Phys. Rev. Lett. **57**, 1696 (1986); J. C. Bergquist *et al.,* Phys. Rev. Lett. **57**, 1699 (1986).
[4] D. J. Wineland *et al.,* J. Res. Natl. Inst. Stand. Technol. **103**, 259 (1998).
[5] B. R. Mollow, Phys. Rev. **188**, 1969 (1969).
[6] J. Javanainen, Opt. Commun. **34**, 375 (1980).
[7] M. Lindberg, Phys. Rev. A **34**, 3178 (1986).
[8] J. I. Cirac *et al.,* Phys. Rev. A **48**, 2169 (1993).
[9] P. S. Jessen *et al.,* Phys. Rev. Lett. **69**, 49 (1992).
[10] Preliminary results have been reported by V. Bühner and Ch. Tamm of PTB, Braunschweig, Germany.
[11] B. Appasamy *et al.,* Appl. Phys. B **60**, 473 (1995).
[12] Ch. Raab *et al.,* Appl. Phys. B **67**, 683 (1998); **69**, 253 (1999).
[13] L. S. Ma *et al.,* Appl. Phys. B **67**, 159 (1993).
[14] M. Schubert *et al.,* Phys. Rev. A **52**, 2994 (1995).
[15] H. J. Kimble, in *Fundamental Systems in Quantum Optics,* Proceedings of the Les Houches Summer School, Session LIII, edited by J. Dalibard, J.-M. Raimond, and J. Zinn-Justin (Elsevier, New York, 1992).
[16] J. T. Höffges *et al.,* Opt. Commun. **133**, 170 (1997); J. T. Höffges *et al.,* J. Mod. Opt. **44**, 1999 (1997).
[17] This corresponds to vacuum field input into the fluorescence port of PBS1.
[18] D. J. Berkeland *et al.,* J. Appl. Phys. **83**, 5025 (1998).
[19] Ch. Roos *et al.,* Phys. Rev. Lett. **83**, 4713 (1999).
[20] S. Stenholm, Rev. Mod. Phys. **58**, 699 (1986).

Bibliography

[1] W. Paul, O. Osberghaus, and E. Fischer. *Ein Ionenkäfig*. Forschungsberichte des Wirtschafts- und Verkehrsministeriums Nordrhein-Westfalen 415, Westfälischer Verlag (1958).

[2] T. W. Hänsch and A. L. Schawlow. *Cooling of gases by laser radiation*. Opt. Comm. **13**(1), 68 (1975).

[3] D. J. Wineland and H. G. Dehmelt. Bull. Am. Soc. **20**, 637 (1975).

[4] W. Neuhauser, M. Hohenstatt, P.E: Toschek, and H.G. Dehmelt. Phys. Rev. A **22** (1980).

[5] F. Diedrich, J. C. Bergquist, W. M. Itano, and D. J. Wineland. *Laser cooling to the zero-point energy of motion*. Phys. Rev. Lett. **62**(4), 403 (1989).

[6] F. Diedrich and H. Walther. *Nonclassical radiation of a single stored ion*. Phys. Rev. Lett. **58** (1987).

[7] M. Schubert, I. Siemers, R. Blatt, W. Neuhauser, and P. E. Toschek. *Photon antibunching and non-poissonian fluorescence of a single three-level ion*. Phys. Rev. Lett. **68** (1992).

[8] Z. H. Lu, S. Bali, and J. E. Thomas. *Observation of squeezing in the phase-dependent fluorescence spectra of two-level atoms*. Phys. Rev. Lett. **81** (1998).

[9] R.J. Glauber. Phys. Rev. **130** (1963).

[10] R.J. Glauber. Phys. Rev. **131** (1963).

[11] R. Hanbury Brown and R.Q. Twiss. Nature **177** (1956).

[12] H.J. Carmichael and D.F. Walls. J. Phys. B **9** (1976).

[13] H.J. Kimble and L. Mandel. Phys. Rev. A **13** (1976).

[14] C. Cohen-Tannoudji. *Frontiers in Laser spectroscopy, Les Houches 1975*. North Holland (1977).

[15] E. Jakeman, E.R. Pike, P.N. Purey, and J.M. Vaugham. J. Phys. A **10** (1977).

[16] H.J. Kimble, M. Dagenais, and L. Mandel. Phys. Rev. A **18** (1978).

[17] M. Dagenais and L. Mandel. Phys. Rev. A **18** (1978).

[18] V. Weisskopf. Ann. Phys. **9** (1931).

[19] B.R. Mollow. Phys. Rev. **188** (1969).

[20] F. Schuda, C.R. jr Stroud, and M. Hercher. J. Phys. **7** (1974).

[21] F.Y. Wu, R.E. Groove, and S. Ezekiel. Phys. Rev. Lett. **35** (1975).

[22] W. Hartig, W. Rassmussen, R. Schieder, and H. Walther. Z. Phys. A **278** (1976).

[23] M. Schubert. *Intensitätskorrelation in der Resonanzfluoreszenz eines einzelnen gespeicherten Ions*. Ph.D. thesis, Universität Hamburg (1991).

[24] Y. Stalgies, I. Siemers, B. Appasamy, T. Altevogt, and P.E. Toschek. Europhys. Lett. **35** (1996).

[25] C. I. Westbrook, R. N. Watts, C. E. Tanner, S. L. Rolston, W. D. Phillips, P. D. Lett, and P. L. Gould. *Localization of atoms in a three-dimensional standing wave*. Phys. Rev. Lett. **65** (1990).

[26] J.T. Höffges, H.W. Baldauf, T. Eichler, S.R. Helfrid, and H. Walther. Opt. Comm. **133** (1997).

[27] M. Lindberg. *Resonance fluorescence of a laser-cooled trapped ion in the lamb-dicke limit*. Phys. Rev. A **34** (1986).

[28] J.I. Cirac, R. Blatt, A.S. Parkins, and P. Zoller. *Spectrum of resonance fluorescence from a single trapped ion*. Phys. Rev. A **48** (1993).

[29] P. S. Jessen, C. Gerz, P. D. Lett, W. D. Phillips, S. L. Rolston, R. J. C. Spreeuw, and C. I. Westbrook. *Observation of quantized motion of rb atoms in an optical field*. Phys. Rev. Lett. **69** (1992).

[30] P. R. Berman. *Cavity quantum electrodynamics*. Advances in atomic, molecular and optical physics, supplement 2. Academic Press (1994).

[31] G. Rempe, F. Schmidt-Kaler, and H. Walther. *Observation of sub-poissonian photon statistics in a micromaser*. Phys. Rev. Lett. **64** (1990).

[32] M. Brune, F. Schmidt-Kaler, A. Maali, J. Dreyer, E. Hagley, J. M. Raimond, and S. Haroche. *Quantum Rabi oscillations: A direct test of field quantization in a cavity*. Phys. Rev. Lett. **76**(11), 1800 (1996).

[33] C. J. Hood, M. S. Chapman, T. W. Lynn, and H. J. Kimble. *Real-time cavity qed with single atoms*. Phys. Rev. Lett. **80** (1998).

[34] P. Münstermann, T. Fischer, P. Maunz, P. W. H. Pinkse, and G. Rempe. *Dynamics of single-atom motion observed in a high-finesse cavity*. Phys. Rev. Lett. **82** (1999).

[35] C. J. Hood, T. W. Lynn, A. C. Doherty, A. S. Parkins, and H. J. Kimble. *The atom-cavity microscope: Single atoms bound in orbit by single photons*. Science **287** (2000).

[36] W. Paul. *Quadrupole mass filter*. Z. Naturforsch. **A8**, 448 (1953).

[37] P. K. Ghosh. *Ion traps*. Clarendon Press (1995).

[38] C. Monroe, D. M. Meekhof, B. E. King, S. R. Jefferts, W. M. Itano, D. J. Wineland, and P. Gould. *Resolved-sideband Raman cooling of a bound atom to the 3D zero-point energy*. Phys. Rev. Lett **75**, 4011 (1995).

[39] S. Chu. Rev. Mod. Phys. **70** (1998).

[40] C. Cohen-Tannoudji. Rev. Mod. Phys. **70** (1998).

[41] W.D. Phillips. Rev. Mod. Phys. **70** (1998).

[42] I. Marzoli, J. I. Cirac, R. Blatt, and P. Zoller. *Laser cooling of trapped three-level ions: Designing two-level systems for sideband cooling*. Phys. Rev. A **49**(4), 2771 (1994).

[43] M. Lindberg and J. Javanainen. J. Opt. Soc. Am. B **3** (1986).

[44] G. Morigi, J. Eschner, and C. Keitel. *Ground state laser cooling using electromagnetically induced transparency*. Phys. Rev. Lett. **85** (2000).

[45] S. Stenholm. *The semiclassical theory of laser cooling*. Rev. Mod. Phys. **58**(3), 699 (1986).

[46] D. Reiß, A. Lindner, and R. Blatt. *Cooling of trapped multilevel ions: A numerical analysis*. Phys. Rev. A **54** (1996).

[47] O.R. Frisch. *The nuclear handbook*. Georges Newnes Ltd., London (1958).

[48] N. Yu, W. Nagourney, and H. Dehmelt. *Radiative lifetime measurement of the* ba^+ *metastable* $d_{3/2}$ *state*. Phys. Rev. Lett. **78** (1997).

[49] A. Gallagher. Phys. Rev. **157**, 24 (1967).

[50] H. Oberst. *Resonance fluorescence of single barium atoms*. Diplomarbeit, Universität Innsbruck (1999).

[51] R. Loudon. *The quantum theory of light*. Oxford University Press, second edition (1983).

[52] M.O. Scully and M.S. Zubairy. *Quantum optics*. Cambridge University Press (1997).

[53] A. Lindner. *Grundkurs Theoretische Physik*. Teubner (1994).

[54] D.F. Walls and G.J. Milburn. *Quantum Optics*. Springer Heidelberg (1994).

[55] M. Lax. Phys. Rev. **145** (1966).

[56] J. Bolle. *Spektroskopie und nichtklassische Fluoreszenzeigenschaften von einzelnen gespeicherten Ba^+-Ionen*. Ph.D. thesis, Universität Innsbruck (1998).

[57] C. Raab. *Ein Laserspektrometer zur Untersuchung einzelner Ba^+-Ionen*. Diplomarbeit, Universität Göttingen (1996).

[58] N. Pörtner. *Stabilisierung und Frequenzverdopplung eines Hochleistungsdiodenlasers bei 986.8 nm zur Spektroskopie an Ba^+-Ionen*. Diplomarbeit, Universität Göttingen (1996).

[59] H. Langfischer. *Frequenzstabilisierung eines Diodenlasers bei 650 nm zur Spektroskopie an einzelnen Barium-Ionen*. Diplomarbeit, Universität Innsbruck (1998).

[60] C. Raab, J. Bolle, H. Oberst, J. Eschner, F. Schmidt-Kaler, and R. Blatt. *A diode laser spectrometer at 493 nm*. Appl. Phys. B **67**, 683 (1998).

[61] K.C. Harvey and C.J. Myatt. *External-cavity diode laser using a grazing-incidence diffraction grating*. Optics Lett. **16** (1991).

[62] J. Helmcke, S.A. Lee, and J.L. Hall. *Dye laser spectrometer for ultrahigh spectral resolution: design and performance*. Appl. Optics **21** (1982).

[63] T. W. Hänsch and B. Couillaud. *Laser frequency stabilization by polarization spectroscopy of a reflecting reference cavity*. Opt. Comm. **35**(3), 441 (1980).

[64] R. W. Drever, J. L. Hall, F. V. Kowalski, J. Hough, G. M. Ford, A. Munley, and H. Ward. *Laser phase and frequency stabilization using an optical resonator*. Appl. Phys. B **31**, 97 (1983).

[65] A. Schenzle, R.G. DeVoe, and R.G. Brewer. Phys. Rev. A **25** (1982).

[66] M. Schulz. *Data sheet for halo 25/0.4* (1999).

[67] D. Berkeland, J. D. Miller, J. C. Bergquist, W. M. Itano, and D. J. Wineland. *Minimization of ion micromotion in a Paul trap*. J. Appl. Phys. **83**, 5025 (1998).

[68] I. Siemers, M. Schubert, R. Blatt, W. Neuhauser, and P.E. Toschek. Europhys. Lett **18** (1982).

[69] Y. Stalgies. *Laser-Fluoreszenz. und Absorptionsspektroskopie an einem einzelnen Ion*. Ph.D. thesis, Universität Hamburg (1998).

[70] P.S. Jessen. *An investigation of the microscopic motion of atoms in optical molasses using optical heterodyne spectroscopy of resonance fluorescence*. Ph.D. thesis, University of Aarhus (1993).

[71] H.Z Cummins and H.L. Swinney. *Light beating spectroscopy*. Progress in Optics VIII. North Holland Publishing (1970).

[72] R.H. Kingston. *Detection of optical and infrared radiation*. Springer (1978).

[73] Ch. Raab, J. Eschner, J. Bolle, H. Oberst, F. Schmidt-Kaler, and R. Blatt. *Motional sidebands and direct measurement of the cooling rate in the resonance fluorescence of a single trapped ion*. Phys. Rev. Lett. **85** (2000).

Dank, wem Dank gebührt.

An erster Stelle bedanke ich mich bei Rainer Blatt für die Aufnahme in seiner Arbeitsgruppe und die interessante Themenstellung. Er war mit seiner Geduld, auch in schwierigen Zeiten, ein steter Begleiter.

Für seine Hilfe bei theoretischen Problemen bedanke ich mich bei Jürgen Eschner. Außerdem war er eine sehr große Hilfe beim Verfassen meiner Publikationen.

Diese Arbeit war nur möglich durch die Vorarbeit von Joachim Bolle, welcher die Vakuumapparatur mit sehr viel Sorgfalt und Liebe aufgebaut hat. Auch stammen viele Ideen für den optischen Aufbau und die Laser von ihm.

Die unzähligen Diplomanden, Nikolas Pörtner, Helmut Langfischer und Hilmar Oberst sollen hier auch nicht vergessen werden. Besonderer Dank gilt Hilmar, der die wunderbaren Fitprogramme schrieb.

Matthias Schulz gilt Dank für die Tips zur Reinigung der Vakuumapparatur und für unzählige kleine Dinge, die hier nicht aufgezählt werden können.

Unsere Leute in der Werkstatt, Toni Schönherr und Stefan Haslwanter, hatten viel Geduld mit meinen Zeichnungen und haben es immer geschafft, das zu produzieren was ich mir vorgestellt habe, aber nicht zeichnen konnte. Bei elektronischen Problemen stand mir Andreas Mitter, Wolfgang Kofler und, ganz wichtig, Otto Peter stets zur Seite.

Zum erfolgreichen Abschluss dieser Arbeit trugen aber auch noch andere Dinge bei.

Hier ist an erster Stelle Matthias zu nennen, der meine Laune mit viel Geduld und Gleichmut ertrug.

Paul trug zur Erweiterung meines musikalischen Horizonts wesentlich bei. Außerdem war er, mit MS, Achim, Axel und Stefan, öfters dafür verantwortlich, dass ich am nächsten morgen verschlafen war und Kopfschmerzen hatte.

Christian, HCN und Sonja haben mit mir die Wohnung geteilt und mich trotzdem nicht mit Physik genervt.

Meine GenossInnen vom VSSTÖ und den Jusos möchte ich natürlich auch nicht vergessen. Sie waren immer für nette Abende und neue Erfahrungen gut.

Meinen Eltern gebührt Dank dafür, dass sie mir mein Studium ermöglicht haben und auch sonst zur Stelle waren, wann immer nötig.

Die alte Erde steht noch, und der Himmel wölbt sich noch über mir!

J.W. Goethe